ATLAS NOTE

ATL-COM-PHYS-2009-000

May 19, 2009

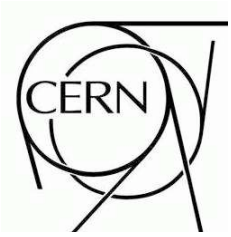

Muon Reconstruction and Identification Performance in ATLAS: Studies with Simulated Monte Carlo Samples

Contributors: D.L. Adams, K. Assamagan, H. Bachacou, S. Behar, N. Benekos, K.M. Black, I. Borjanovic, C. Boulahouache, L. Chevalier, T. Cornelissen, A. Dell'Acqua, D. Fassioulotis, S. Goldfarb, S. Hassani, L. Kashif, P. Kluit, C. Kourkoumelis, T. Lagouri, J.-F. Laporte, D. Levin, E. Moyse, R. Nikolaidou, K. Nikolopoulos, A. Ouraou, N. Panikashvili, W. Park, A. Poppleton, D. Rebuzzi, G. Salamanna, S. Spagnolo, J. Snuverink, S. Tarem, S. Todorova, S. Vallecorsa, N. van Eldik, Z. van Kesteren, S. Willocq, M. Woudstra.

Editors: D. L. Adams, A. Ouraou, A. Poppleton, S. Willocq.

Abstract

Muon reconstruction and identification in ATLAS relies on the Muon Spectrometer for standalone reconstruction, as well as on the Inner Detector and Calorimeter for identification and combined reconstruction.

This note is an expanded version of the note ATL-COM-PHYS-2009-151 published as part of the CSC note book. It presents the results of detailed performance studies of the various ATLAS muon reconstruction and identification algorithms as a function of transverse momentum, pseudorapidity and azimuth. Performance is evaluated with a range of different single-muon and physics Monte Carlo samples, including samples with cavern background and pileup. Emphasis is placed on comparison between algorithms with common muon selection criteria, defined in this note. Results are based on data simulated and reconstructed in 2007 with release 12.0.6.

Contents

1 Introduction

The ATLAS experiment will detect particles created in 14 TeV proton-proton collisions produced by the CERN LHC (Large Hadron Collider). Only a tiny fraction of these collisions will correspond to interesting standard model processes and an even smaller fraction to new physics. Muons, especially those with high-p_T (transverse momentum) and those that are isolated (from other activity in the detector), will be much more common in these interesting events than in the background, and thus provide important means to identify such events and to determine their properties. The ATLAS detector has been designed to be efficient in the detection of muons and to provide precise measurement of their kinematics up to one TeV.

In parallel with the construction of the detector, software has been developed to reconstruct these muons, i.e., for each recorded event, to identify muons and measure their position, direction and momentum. Here we describe the strategies being pursued for this reconstruction and the current performance characterized in terms of efficiency, fake rate and precision and accuracy of measurement. The results reported here are based on simulation data generated and reconstructed in 2007 with release 12.0.6.

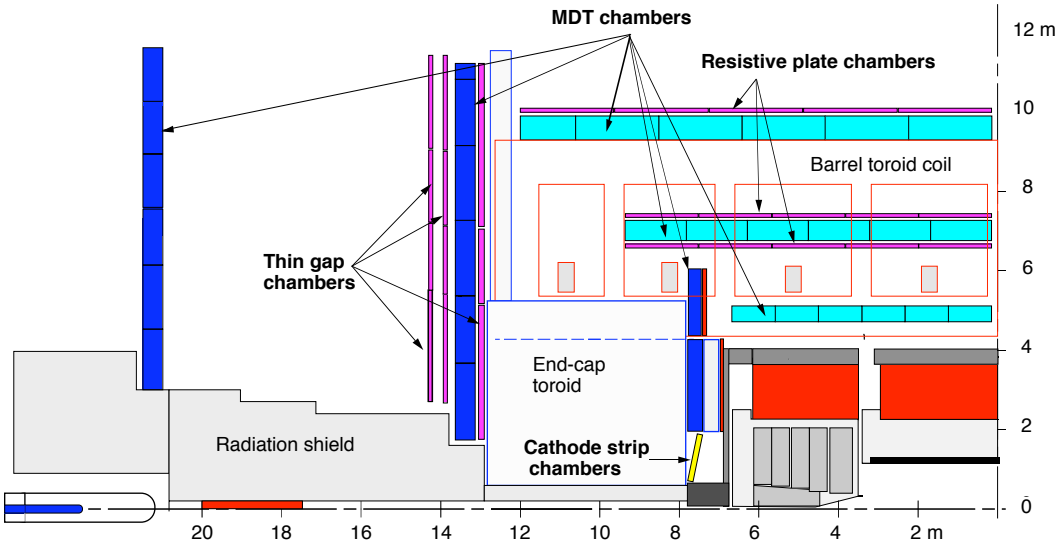

Figure 1: The ATLAS muon spectrometer.

2 Detector

The ATLAS detector [1] has been designed to provide clean and efficient muon identification and precise momentum measurement over a wide range of momentum and solid angle. The primary detector system built to achieve this is the muon spectrometer, shown in Figure 1. The spectrometer covers the pseudo-rapidity range $|\eta| < 2.7$ and allows identification of muons with momenta above 3 GeV/c and precise determination of p_T up to about 1 TeV/c.

The muon spectrometer comprises three subsystems:

- Superconducting coils provide a toroidal magnetic field whose integral varies significantly as a function of both η and φ (azimuthal angle). The integrated bending strength (Figure 2) is roughly constant as a function of η except for a significant drop in the transition between the barrel and endcap toroid coils ($1.4 \lesssim |\eta| \lesssim 1.6$).

- Precision detectors are located in three widely-separated *stations* at increasing distance from the collision region. Each station includes multiple closely-packed layers measuring the η-coordinate, the direction in which most of the magnetic field deflection occurs. Monitored drift tubes provide these measurements everywhere except in the high-η ($|\eta| > 2.0$) region of the innermost station where cathode strip chambers are used. The measurement precision in each layer is typically better than 100 μm. The cathode strip chambers additionally provide a rough (1 cm) measurement of the φ-coordinate.

- Resistive plate and thin gap chambers provide similarly rough measurements of both η and φ near selected stations.

High-p_T muons typically traverse all three stations but there are η-φ regions where one, two or all three stations do not provide a precision measurement, e.g. those regions with support structures or passages for services. There are also regions where overlaps allow two measurements from a single station. Figure 3 shows the number of station measurements as function of η and φ. The resolution and efficiency are degraded where one or more stations do not provide a measurement.

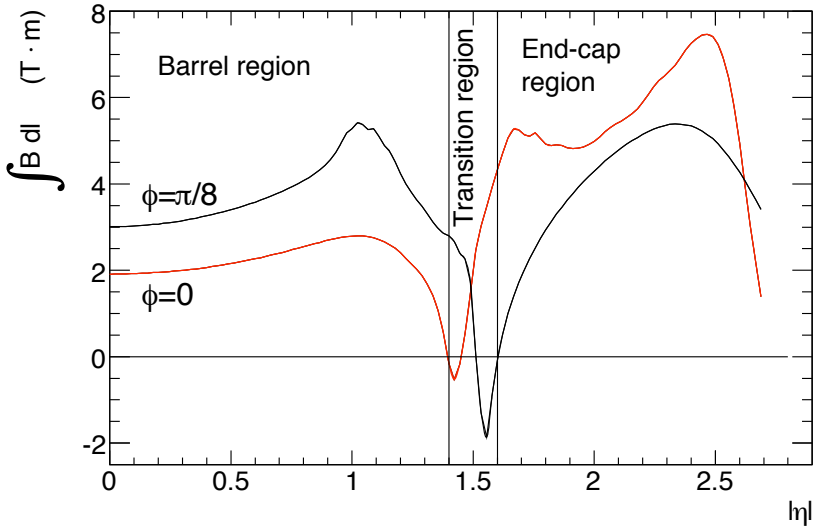

Figure 2: ATLAS muon spectrometer integrated magnetic field strength as a function of $|\eta|$.

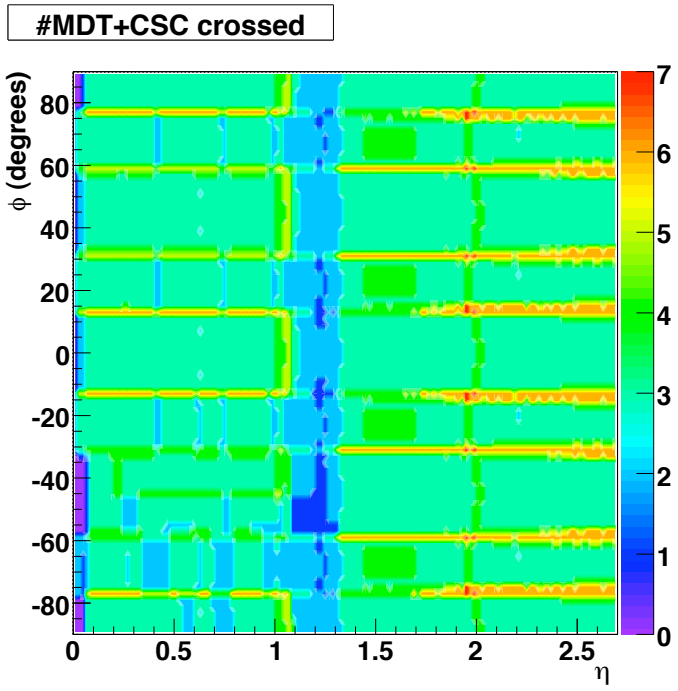

Figure 3: Number of detector stations traversed by muons passing through the muon spectrometer as a function of $|\eta|$ and φ.

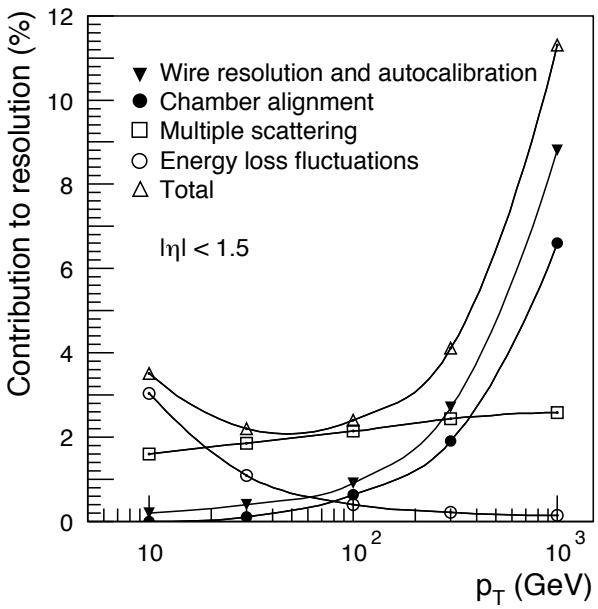

Figure 4: Contributions to the momentum resolution for muons reconstructed in the Muon Spectrometer as a function of transverse momentum for $|\eta| < 1.5$. The alignment curve is for an uncertainty of 30 μm in the chamber positions.

Figure 4 shows how contributions to the muon spectrometer momentum resolution vary as a function of p_T. At low momentum, the resolution is dominated by fluctuations in the energy loss of the muons traversing the material in front of the spectrometer. Multiple scattering in the spectrometer plays an important role in the intermediate momentum range. For $p_T > 300$ GeV/c, the single-hit resolution, limited by detector characteristics, alignment and calibration, dominates.

The other ATLAS detector systems also play important roles in achieving the ultimate performance for muon identification and measurement. The calorimeter, with a thickness of more than 10 interaction lengths, provides an effective absorber for hadrons, electrons and photons produced by proton-proton collisions at the center of the ATLAS detector. Energy measurements in the calorimeter can aid in muon identification because of their characteristic minimum ionizing signature and can provide a useful direct measurement of the energy loss [2].

A tracking system inside the calorimeters detects muons and other charged particles with hermetic coverage for $|\eta| < 2.5$, providing important confirmation of muons found by the spectrometer over that η range. This *inner detector* has three pixel layers, four stereo silicon microstrip layers, and, for $|\eta| < 2.0$, a straw-tube transition radiation detector that records an average of 36 additional measurements on each track. A 2 Tesla solenoidal magnet enables the inner detector to provide an independent precise momentum measurement for muons (and other charged particles). Over most of the acceptance, for p_T roughly in the range between 30 and 200 GeV/c, the momentum measurements from the inner detector and muon spectrometer may be combined to give precision better than either alone. The inner detector dominates below this range, and the spectrometer above it.

3 Overview of reconstruction and identification algorithms

ATLAS employs a variety of strategies for identifying and reconstructing muons. The direct approach is to reconstruct *standalone* muons by finding tracks in the muon spectrometer and then extrapolating these to the beam line. *Combined* muons are found by matching standalone muons to nearby inner detector tracks and then combining the measurements from the two systems. *Tagged* muons are found by extrapolating inner detector tracks to the spectrometer detectors and searching for nearby hits. Calorimeter tagging algorithms are also being developed to tag inner detector tracks using the presence of a minimum ionizing signal in calorimeter cells. These were not used in the data reconstruction reported here and their performance is documented elsewhere [2].

The 2007 ATLAS baseline reconstruction includes two algorithms for each strategy. Here we briefly describe these algorithms. Later sections describe their performance.

The algorithms are grouped into two families such that each family includes one algorithm for each strategy. The output data intended for use in physics analysis includes two collections of muons—one for each family—in each processed event. We refer to the collections (and families) by the names of the corresponding combined algorithms: Staco [3] and Muid [4], see Sec. 3.6 for further information.

3.1 Standalone muons

The standalone algorithms first build track segments in each of the three muon stations and then link the segments to form tracks. The Staco-family algorithm that finds the spectrometer tracks and extrapolates them to the beam line is called Muonboy [3]. On the Muid side, Moore [5] is used to find the tracks and the first stage of Muid performs the inward extrapolation.

The extrapolation must account for both multiple scattering and energy loss in the calorimeter. Muonboy assigns energy loss based on the material crossed in the calorimeter. Muid additionally makes use of the calorimeter energy measurements if they are significantly larger than the most likely value and the muon appears to be isolated [6].

Standalone algorithms have the advantage of slightly greater $|\eta|$ coverage—out to 2.7 compared to 2.5 for the inner detector—but there are holes in the coverage at $|\eta|$ near 0.0 and 1.2 (see figure 3). Very low momentum muons (around a few GeV/c) may be difficult to reconstruct because they do not penetrate to the outermost stations.

Muons produced in the calorimeter, e.g. from π and K decays, are likely to be found in the standalone reconstruction and serve as a background of "fake" muons for most physics analyses. There are a few exotic channels for which charged particles appearing in the calorimeter are a signal of interest.

3.2 Inner detector

The primary track reconstruction algorithm for the inner detector is described in Ref. [7]. Space points are identified in the pixel and microstrip detectors, these points are linked to form track seeds in the inner four layers, and tracks are found by extending these seeds to add measurements from the outer layers. This strategy is expected to give very high detection efficiency over the full detector acceptance, $|\eta| < 2.5$.

3.3 Combined muons

Both of the muon combination algorithms, Staco and Muid, pair muon-spectrometer tracks with inner-detector tracks to identify combined muons. The match chi-square, defined as the difference between outer and inner track vectors weighted by their combined covariance matrix:

$$\chi^2_{match} = (\mathbf{T_{MS}} - \mathbf{T_{ID}})^{\mathrm{T}} (\mathbf{C_{ID}} + \mathbf{C_{MS}})^{-\mathbf{1}} (\mathbf{T_{MS}} - \mathbf{T_{ID}}) \quad (1)$$

provides an important measure of the quality of this match and is used to decide which pairs are retained. Here **T** denotes a vector of (five) track parameters—expressed at the point of closest approach to the beam line—and **C** is its covariance matrix. The subscript ID refers to the inner detector and MS to the muon spectrometer (after extrapolation accounting for energy loss and multiple scattering in the calorimeter).

Staco does a statistical combination of the inner and outer track vectors to obtain the combined track vector:

$$\mathbf{T} = (\mathbf{C}_{\mathbf{ID}}^{-\mathbf{1}} + \mathbf{C}_{\mathbf{MS}}^{-\mathbf{1}})^{-\mathbf{1}} (\mathbf{C}_{\mathbf{ID}}^{-\mathbf{1}} \mathbf{T}_{\mathbf{ID}} + \mathbf{C}_{\mathbf{MS}}^{-\mathbf{1}} \mathbf{T}_{\mathbf{MS}}) \quad (2)$$

Muid does a partial refit: it does not directly use the measurements from the inner track, but starts from the inner track vector and covariance matrix and adds the measurements from the outer track. The fit accounts for the material (multiple scattering and energy loss) and magnetic field in the calorimeter and muon spectrometer.

3.4 Tagged muons

The spectrometer tagging algorithms, MuTag [3] and MuGirl [8], propagate all inner detector tracks with sufficient momentum out to the first station of the muon spectrometer and search for nearby segments. MuTag defines a tag chi-square using the difference between any nearby segment and its prediction from the extrapolated track. MuGirl uses an artificial neural network to define a discriminant. In either case, if a segment is sufficiently close to the predicted track position, then the inner detector track is tagged as corresponding to a muon.

At present, both algorithms simply use the inner-detector track to evaluate the muon kinematics, i.e. the inner track and spectrometer hit are not combined to form new track. This is not very important in low-p_T regime that these algorithms were originally intended to address. Both algorithms are being further developed to allow extrapolation to other and multiple stations and add the capability to include the spectrometer measurements in a track refit.

There is an important difference in the way these algorithms are run in the standard reconstruction chain. MuGirl considers all inner-detector tracks and redoes segment finding in the region around the track. MuTag only makes use of inner-detector tracks and muon-spectrometer segments not used by Staco. Thus MuTag serves only to supplement Staco while MuGirl attempts to find all muons. Obviously, MuTag is part of the Staco family and most sensibly used in that context. MuGirl muons are recorded as part of the Muid family.

3.5 Merging muons

The muon finding efficiency (and fake rate) may be increased by including muons found by multiple algorithms but care must be taken to remove overlaps, i.e. cases where the same muon is identified by two or more algorithms. To a large extent, this is done when the collections are created. Standalone muons that are successfully combined are not recorded separately. In those cases where a standalone muon is combined with more than one inner-detector track, exactly one of the muons is flagged as "best match." In the Staco collection, the tagged and combined muons do not overlap by construction. In the Muid collection, overlaps between MuGirl and Muid muons are removed by creating a single muon when both have the same inner detector track.

Analysts wishing to merge standalone and tagged muons or muons from different collections may make use of a muon selection tool to remove overlaps. It requires muons have different inner-detector tracks and merges standalone muons that are too close to one another. Closeness is defined by η-φ separation with a default limit of 0.4.

3.6 Selection criteria

The output reconstruction stream intended for physics analysis is called the AOD (analysis-oriented data) and, for each processed event, it includes two muon containers: Staco and Muid with contents listed in table 1. The muons found in these containers are created by merging the muons of each type, e.g. a combined muon and the corresponding spectrometer and extrapolated muons are stored as a single muon object with pointers to each of the corresponding tracks.

Container	Algorithm	Muon type
Staco	Muonboy	standalone in the muon spectrometer
	Muonboy	standalone extrapolated to the beam line
	Staco	combined
	MuTag	inner detector with spectrometer tag
Muid	Moore	standalone in the muon spectrometer
	Muid	standalone extrapolated to the beam line
	Muid	combined
	MuGirl	inner detector with spectrometer tag

Table 1: AOD containers. The last column list the types of muons in the container and the middle column indicates the algoritmm which produces that type.

It is possible for a combined muons to share an innner detector or muon spectrometer track. In this case, one of the muons is flagged as "best match" to indicate it is the preferred candidate. For typical analysis and the results presented here, combined muons are used only if this flag is set. A typical analysis selects best-match combined muons from one of these containers possibly supplementing this with the tagged or extrapolated standalone muons from the same container.

The spectrometer standalone muons have their track parameters expressed at the entrance to the muon spectrometer (or first muon hit surface) and are typically not of direct interest for physics analysis. In the following, we will often omit the qualifier "extrapolated" and speak simply of standalone muons, Muonboy muons or Moore/Muid muons when referring to extrapolated standalone muons.

In this note, we separately examine the performance of the (extrapolated) standalone, combined and tagged muons in each container. We also consider a couple cases where muons from different algorithms are merged. Unless explicitly stated, we make no other selecton cuts. The selections were performed using the MuonSelectionTools package which assign a name to each of our selections. Table 2 lists the selections used in this note. The selection Muid+MuGirl avoids double counting by removing MuGirl muons that are within an eta-phi distance of 0.4 to a Muid combined muon. MuTag muons are constructed so that such a cut is not rqequired.

Name	Selection name	Meaning
Muonboy	mucon_staco_standalone_selk001	extrapolated standlone from Staco
Moore/Muid	mucon_muid_standalone_selk001	extrapolated standlone from Muid
Staco	mucon_staco_combined_selk001	combined from Staco
Muid	mucon_muid_combined_selk001	combined from Muid
MuTag	mucon_staco_inner_selk001	spectrometer-tagged from Staco
MuGirl	mucon_muid_inner_selk001	spectrometer-tagged from Muid
Staco+MuTag	mucon_staco_comb+in_selk001	combined or spectrometer-tagged from Staco
Muid+MuGirl	mucmb_mugirl_kine_selk001	combined or spectrometer-tagged from Muid

Table 2: Muon selections used in this note. The first column is the name used here, the second is the selection name in the MuonSelectionTools package.

4 Tools for performance evaluation and classification of tracks

Simulation samples were created in the ATLAS framework by running an event generator (PYTHIA [9] or MC@NLO [10, 11]) and using GEANT4 [12] to propagate the final-state particles using ATLAS-specific code to describe the geometry and response of the detector. The data were then reconstructed using the software based on the algorithms described in the previous chapter.

4.1 Truth matching and track classification

Muon reconstruction performance is evaluated for each event by comparing selected reconstructed muons with the true muons, i.e. those in the Monte Carlo truth record. The latter include muons created in the initial event generation as well as secondaries produced during propagation through the tracking volume. Muons produced in the calorimeter or muon spectrometer are not included in the truth record. True muons with transverse momentum below 2 GeV/c are also excluded to avoid spurious matches with candidates we do not expect to be able to reconstruct.

For each event, a one-to-one matching is performed between the selected reconstructed muons and the true muons using the SampleMatch algorithm in the MuonIDTruthMatching package. The matching makes use of two distance metrics: D_{ref} is the *reference* distance measured from true muon to the reconstructed muon:

$$D_{ref} = \sqrt{\left(\frac{\varphi_{reco} - \varphi_{true}}{0.005}\right)^2 + \left(\frac{\eta_{reco} - \eta_{true}}{0.005}\right)^2 + \left(\frac{\Delta p_T / p_T}{0.03}\right)^2} \tag{3}$$

and D_{eva} is the *evaluation* distance measured from the reconstructed muon to the true muon:

$$D_{eva} = \sqrt{(\mathbf{T_{reco}} - \mathbf{T_{true}})\, \mathbf{C_{reco}^{-1}}\, (\mathbf{T_{reco}} - \mathbf{T_{true}})} \tag{4}$$

In the first equation, $\Delta p_T / p_T$ is the fractional momentum resolution:

$$\frac{\Delta p_T}{p_T} = \frac{1/p_{Treco} - 1/p_{Ttrue}}{1/p_{Ttrue}} = \frac{p_{Ttrue} - p_{Treco}}{p_{Treco}} \tag{5}$$

Here p_T is signed (i.e. carries the charge sign), but elsewhere in the text it denotes the magnitude of the transverse momentum. In the second distance equation, $\mathbf{T}$ again denotes the vector of (five) track parameters (expressed at the distance of closest approach to the beam line) and $\mathbf{C}$ the associated covariance matrix. Note that D_{eva}^2 is a chi-square with five degrees of freedom.

There is a maximum allowed value for each of these distances. For D_{eva} the maximum value is 1000, a very loose cut. The limit for D_{ref} is 100 and we see from equation 3 this implies the matched muons must be within a distance of 0.5 in η and φ and have the same charge sign with $p_{Treco} > 0.25\, p_{Ttrue}$ or opposite sign with $p_{Treco} > 0.50\, p_{Ttrue}$.

The matching is carried out by first examining each reconstructed muon and assigning it to the nearest true muon using the evaluation distance. The reconstructed muon is left unmatched if no distance is less than the maximum allowed value. The reference distance is evaluated for each match and the match is discarded if it exceeds the threshold for that quantity. If more than one match remains for any true muon, then only the match with the smallest reference distance is retained.

True muons that are matched are said to be *found* and those left unmatched are *lost*. Found muons are classified as *good* if they have $D_{eva} < 4.5$ corresponding to a chi-square probability above 0.0011.

Reconstructed muons are said to be *real* if they are matched and *fake* if unmatched. Note that these fakes may correspond to true muons produced outside the tracking volume (e.g. in the calorimeter) and hence not included in the truth record.

A similar procedure is used to evaluate performance for dimuons. For each event, a reference sample is obtained by taking all opposite-sign truth muon pairs with mass greater than 2 GeV/c^2. An evaluation collection is created from the reconstructed muons in the same way and then these are matched using the SampleMatch tool with reference and evaluation distances both calculated as follows:

$$D_{dimuon} = \sqrt{\left(\frac{\varphi_{eva} - \varphi_{ref}}{0.10}\right)^2 + \left(\frac{\eta_{eva} - \eta_{ref}}{0.10}\right)^2 + \left(\frac{p_{Teva} - p_{Tref}}{0.10\, p_{Teva}}\right)^2 + \left(\frac{M_{eva} - M_{ref}}{0.10\, M_{ref}}\right)^2} \quad (6)$$

The maximum-allowed value for the reference and evaluation distances is 1000.

4.2 Performance measures

Our performance measures include efficiency, fake rate, resolutions and resolution tails. The efficiency or *finding efficiency* is defined to be the fraction of true muons that are found and is typically evaluated for some kinematic selection (applied after matching). The *good efficiency* is the fraction of true muons that are found and classified as good (as defined in the previous section). The *good fraction* is the fraction of found muons that are classified as good. In the sections that follow, we present the overall efficiency for various physics samples and the efficiency as a function of η for the primary benchmark sample.

The fake rate is defined to be the mean number of fake muons per event and it is presented for a variety of p_T thresholds corresponding to the values that might be chosen for different physics analyses.

Five kinematic variables characterize a track and we choose the set in table 3. These are defined at the point of closest approach to the beam line. They are slightly different than those used in ATLAS tracking but are closer to those used in physics analysis. The precision and accuracy of the direction measurements are typically much better than that required for any physics analysis. The measurement of the initial position of the track (e.g. at the distance of closest approach to the beam line or vertex) is discussed in another note [13]. For the momentum, we use the fractional residual, $\Delta p_T/p_T$, defined in equation 5.

The tails in the residual distributions are often more important than the resolution. To characterize these for r0, z0, phi and eta, we define four thresholds for each variable and evaluate what fraction of reconstructed muons have residual magnitudes in excess of each threshold, e.g. what fraction have $|\Delta\eta| > 0.1$. These are also presented as functions of eta and pT.

For the pT residual, we define five tail categories. The first three are fractional ranges on $|\Delta p_T|/p_T$, the fractions for which this ratio exceed 5%, 10% or 30%. The last category is the fraction for which the charge sign is incorrectly measured. Finally there is an intermediate category in which either the sign is incorrect or the magnitude of the measured momentum is twice or more larger than the true value.

The pull is the ratio of the residual to assigned error and provides a measure of the quality of these error estimates. We also present the width of this distribution and its tails as functions of eta and pT. The latter are the fractions of pulls that are greater than 3, 10, 30 or 100.

Variable	Meaning
r0 (r_0)	signed impact parameter (transverse distance to the beam line)
z0 (z_0)	z-position
phi (φ)	polar direction (angle in the plane normal to the beam line)
eta (η)	pseudorapidity
pT (p_T)	transverse momentum

Table 3: Track kinematic variables used in this note.

Performance analysis was performed using the MuPerf algorithms and macros contained in the ATLAS MuonIDValidation package. A separate job was run for each dataset and muon selection. The output of each job includes a ROOT tree (ntuple) containing the selected matched and unmatched truth and and reconstructed muons. These trees were then used to generate most of the plots shown in this document.

Evaluation of efficiencies, fake rates and tail fractions were straightforward and errors were calculated using binomial statistics. Where present, Monte Carlo weights were properly handled in estimating both values and errors. The widths of the residual and pull distributions were obtained by fitting with a Gaussian and reporting the sigma of that distribution. Although the distributions are often not Gaussian, they are peaked and we did some checks to verify that results do not depend strongly on the choice of the fit ranges as long as that range is many sigma from the peak in both directions. In the resolution and pull plots, we fit over a range symmetric about zero extending to four times the maximum value of the resolution or pull axis.

4.3 Monte Carlo samples

Muon reconstruction is an essential element in the reconstruction of many of the simulation samples ATLAS has produced. These samples cover a wide range of physics processes and, rather than trying to survey all of these, we concentrate on a few representative processes to illustrate the performance of the reconstruction. Unless otherwise indicated, all samples were taken from standard ATLAS production based on software release 12.0.6 or 12.0.7.

Our primary benchmark sample is a collection of $t\bar{t}$ events requiring the presence of at least one lepton (electron, muon or tau). The initial inclusive sample was produced using MC@NLO in conjunction with Herwig [14]. This sample provides a variety of mechanisms for producing muons and we present results for two: *direct* muons which do not have any quarks in their ancestry and *indirect* muons whose ancestry includes a heavy quark (b or c) but not a tau. In this sample, the former are produced directly in the leptonic decay of a W-boson.

Performance metrics are plotted as a function of η for $t\bar{t}$ direct muons. In addition, we tabulate efficiencies and fake rates for these muons, for $t\bar{t}$ indirect muons, and for muons in separate low- and high-p_T samples. The low-p_T sample is taken from direct PYTHIA J/ψ production with the J/ψ forced to decay to two muons and a filter selecting only those events where both muons have $|\eta| < 2.5$ and $p_T > 4$ GeV/c. Muons produced by other processes in these events are suppressed by restricting the analyzed sample to muons that have a c-quark in their ancestry. The high-p_T sample consists of direct muons in PYTHIA production of $Z' \rightarrow \mu\mu$ with a Z' mass of 2 TeV. The generation also includes Z/γ and interference but a dimuon mass cut ($m_{\mu\mu} > 500$ GeV/c) ensures that the average muon p_T is above 500 GeV/c.

At design luminosity, ATLAS will have many interactions in each beam crossing (pileup) and there will be significant background in the muon chambers from low-energy photons and neutrons (cavern background). To get an estimate of the effect this will have on our reconstruction algorithms, we processed a $t\bar{t}$ sample overlaid with the backgrounds expected for a reference luminosity of 10^{33} cm^{-2}s^{-1}. The cavern background was included with a safety factor of 2.0, i.e. at twice the value expected for this luminosity. In the following, this sample is called the high-luminosity $t\bar{t}$ sample. Low luminosity refers to samples without any pileup or cavern background.

There is considerable uncertainty in the estimate of the cavern background and active development is underway to improve reconstruction in this environment, and so the results presented here provide only a rough indication of the performance we expect at high luminosity.

Figure 5 shows the p_T, η and isolation energy distributions for the true muons in the samples studied in this note. The isolation energy was obtained by summing the calorimeter transverse energy in an η-φ

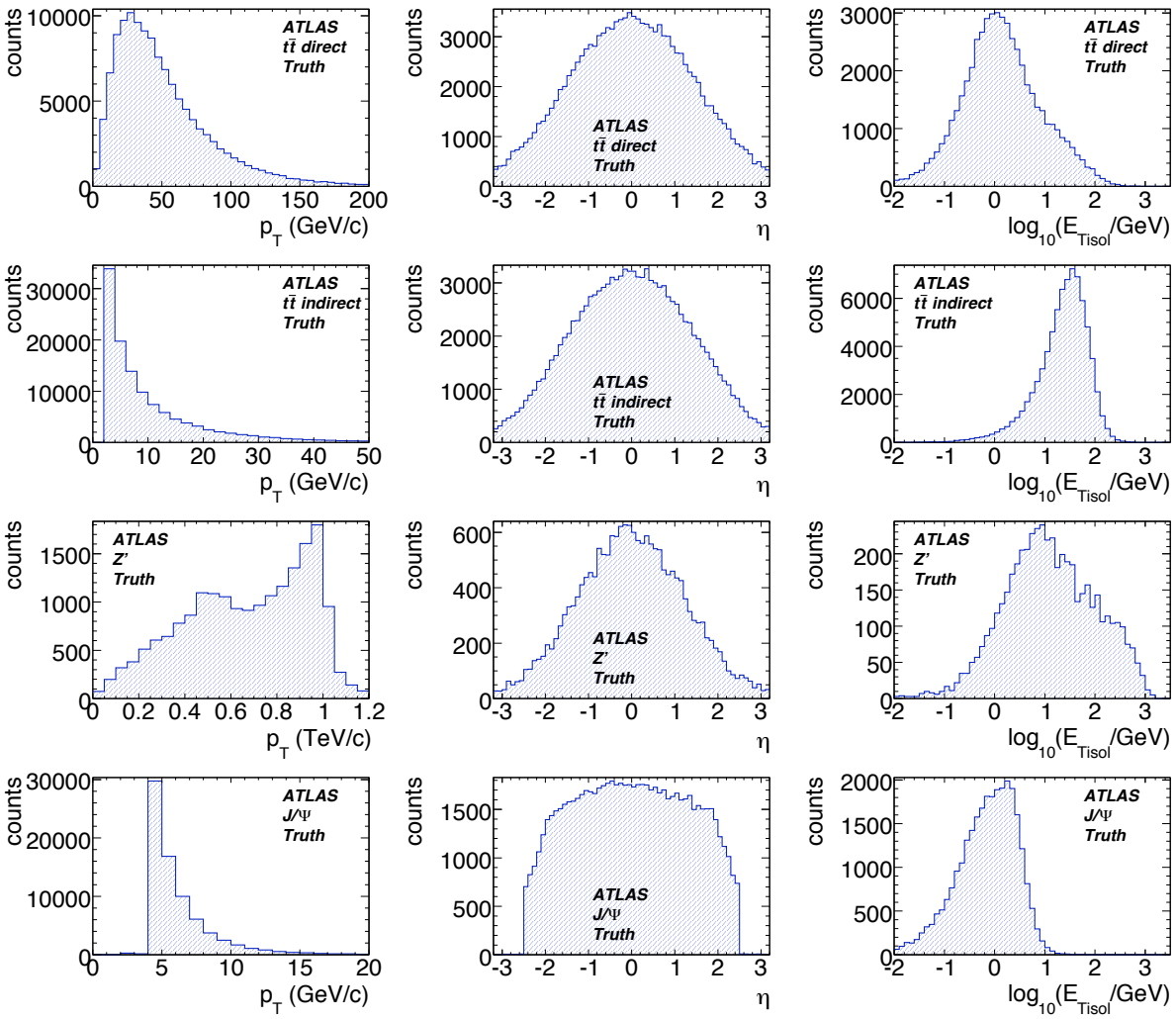

Figure 5: True p_T (left), η (center) and isolation (right) distributions for the $t\bar{t}$ direct muons (top), $t\bar{t}$ indirect muons (second from top), Z' (mass 2 TeV) direct muons (third from top) and J/ψ muons (bottom). Note that the p_T range is different in each of the plots of that variable.

cone of radius 0.2 about the muon. The most probable value for the muon energy loss (as discussed in reference [2]) is subtracted from from these values.

In addition to single-muon performance, we also examine performance for reconstructing dimuon resonances. For these we use a Z sample as well as the J/psi and Zprime samples described above.

Table 4 gives the full names of the datasets studies in this note. We were not able to access all the files associated with each dataset but did process a substantial fraction for each. Table 5 lists the numbers of files and events processed for each dataset. In some cases the number of processed events (i.e. the number used to fill the ntuples) is less than the number read because we skipped events which had the same ID (event number) as any previously-processed event. This was done to avoid duplicate signal events which appear in the pileup samples. Some of the inner detector performance studies were done using a subset of the T1 sample.

The T1 events have Monte Carlo weights set to either 1 or -1 with roughly 15% having the latter value. These weights were used when evaluating the performance leading to the possibility that the efficiency could be less than zero or greater than one in bins with small statistics.

Name	ATLAS dataset name
T1	trig1_misal1_mc12.005200.T1_McAtNlo_Jimmy.recon.AOD.v12000601
T1sf2	trig1_pile1sf02_misal1_mc12.005200.T1_McAtNlo_Jimmy.recon.AOD.v12000605
T1sf5	trig1_pile1sf05_misal1_mc12.005200.T1_McAtNlo_Jimmy.recon.AOD.v12000605
Z	trig1_misal1_csc11.005145.PythiaZmumu.recon.AOD.v12000601
Zprime	trig1_misal1_csc11.005602.Zprime_mumu_pythia_SSM2000.recon.AOD.v12000604
J/psi	trig1_misal1_mc12.017504.Pythia_directJpsimu4mu4.recon.AOD.v12000702

Table 4: Datasets used in this note.

Name		# events	
Name	# files	read	processed
T1	2290	569750	437011
T1sf2	2373	593248	78234
T1sf5	391	97600	75324
Z	784	195030	195030
Zprime	38	9500	9500
J/psi	151	37425	37425

Table 5: Dataset file and event counts.

5 Standalone muon performance

Most of the muons, including those of best quality, are reconstructed by independently finding tracks in the inner detector and muon spectrometer and then combining these tracks. The standalone spectrometer tracks can also be used alone to identify muons in regions beyond the coverage of the inner detector ($2.5 < |\eta| < 2.7$), recover muons for which the combination fails, identify muons produced late in the inner tracker or in the calorimeter, and as a check of inner detector performance.

The standalone reconstruction has two major steps: finding and fitting of tracks in the spectrometer and the extrapolation of those tracks to their closest approach to the beam line. The latter must account for multiple scattering and energy loss including that in the calorimeter. These effects are considered in detail in another note [2]. Here we present results for Muonboy (which does finding, fitting and extrapolation) and the combination Moore/Muid where Muid extrapolates the tracks found by Moore.

5.1 Efficiencies and fake rates

Figure 6 shows the standalone $t\bar{t}$ direct muon efficiencies and fake rates as functions of η at low luminosity (i.e. without any pileup or cavern background) and at our reference luminosity (10^{33} /cm^2/sec with cavern background safety factor 2.0). Table 6 gives the integrated efficiencies and fake rates for these and other samples.

Comparing with Figure 3, we see most of the efficiency loss occurs in regions where the detector coverage is poor, i.e. for $|\eta|$ around 0.0 and 1.2. Otherwise, the $t\bar{t}$ muon efficiency is close to 100% for Muonboy and around 99% for Moore/Muid. The Muid good fraction is significantly higher than for Muonboy, presumably because of better handling of the material in the calorimeter. The algorithms have similar fake rates at low luminosity. At the higher luminosity, the Staco rate increase significantly (by a factor of 2-4) while the Moore/Muid rate increases dramatically (factor of 100). In the high-p_T Z', the efficiency falls by a few percent for both algorithms. For the low-p_T (and non-isolated) J/ψ muons, the Moore/Muid efficiency degrades significantly while Muonboy remains high.

	Efficiency		Fakes/(1000 events) above p_T limit (GeV/c)			
Sample	found	good	3	10	20	50
Muonboy						
$t\bar{t}$ direct	0.951 (1)	0.812 (1)	24.0 (3)	4.4 (1)	1.69 (7)	0.52 (4)
$t\bar{t}$ indirect	0.949 (1)	0.783 (2)				
hi-$\mathscr{L}$ $t\bar{t}$ direct	0.950 (2)	0.809 (3)	53 (1)	8.2 (4)	3.9 (2)	1.9 (2)
Z' direct	0.914 (2)	0.781 (3)	141 (4)	79 (3)	61 (3)	37 (2)
J/ψ	0.959 (3)	0.764 (6)	51 (1)	5.0 (4)	1.6 (2)	0.6 (1)
Moore/Muid						
$t\bar{t}$ direct	0.943 (1)	0.861 (1)	19.8 (3)	3.9 (1)	1.44 (6)	0.47 (4)
$t\bar{t}$ indirect	0.920 (2)	0.838 (2)				
hi-$\mathscr{L}$ $t\bar{t}$ direct	0.932 (2)	0.836 (3)	984 (4)	301 (2)	156 (2)	61 (1)
Z' direct	0.887 (2)	0.769 (3)	168 (4)	102 (3)	75 (3)	43 (2)
J/ψ	0.830 (5)	0.723 (6)	6.7 (4)	1.1 (2)	0.5 (1)	0.13 (6)

Table 6: Muonboy and Moore/Muid efficiencies and fake rates for various samples (section 4.3). Efficiencies are presented both for all found muons and for those with a good truth match ($D_{eva} < 4.5$). Both are calculated for true muons with $|\eta| < 2.5$ and $p_T > 10$ GeV/c. Fake rates are presented for a variety of p_T thresholds.

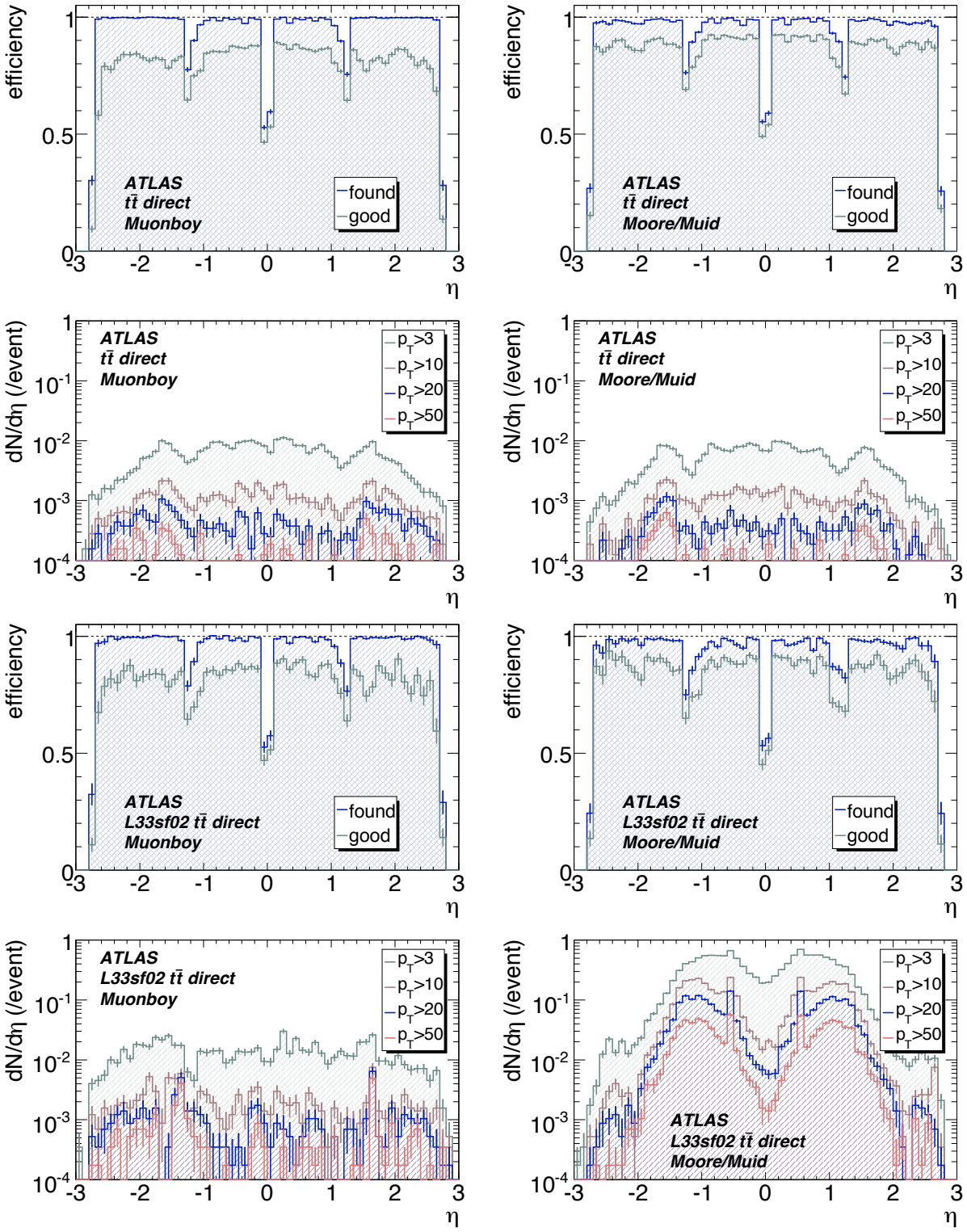

Figure 6: Standalone efficiency and fake rate as functions of true η for Muonboy (left) and Moore/Muid (right) for direct muons in $t\bar{t}$ at low (top) and high (bottom) luminosity. In the efficiency plots, the upper curve (blue) is the efficiency to find the muon while the lower curve (green) additionally requires a good match ($D_{eva} < 4.5$) between reconstructed and true track parameters. Fake rates are shown for a variety of p_T thresholds.

5.2 Resolution

Figure 7 show the p_T resolutions and tails as functions of η and p_T. The resolution is degraded at intermediate pseudorapidity ($1.2 < |\eta| < 1.7$) because of the reduced number of measurements (figure 3), the low field integral in the overlap between barrel and endcap toroids (figure 2), and the material in the endcap toroid (figure 1). The average resolution is very similar for the two algorithms. Despite having a lower good fraction, Muonboy has fewer muons for which the charge sign is incorrectly measured. This suggests that, at least in the tails, Moore/Muid provides a better estimate of the momentum error while Muonboy provides a better estimate of its value. The Moore/Muid tails are likely due to the assignment of incorrect hits to spectrometer tracks.

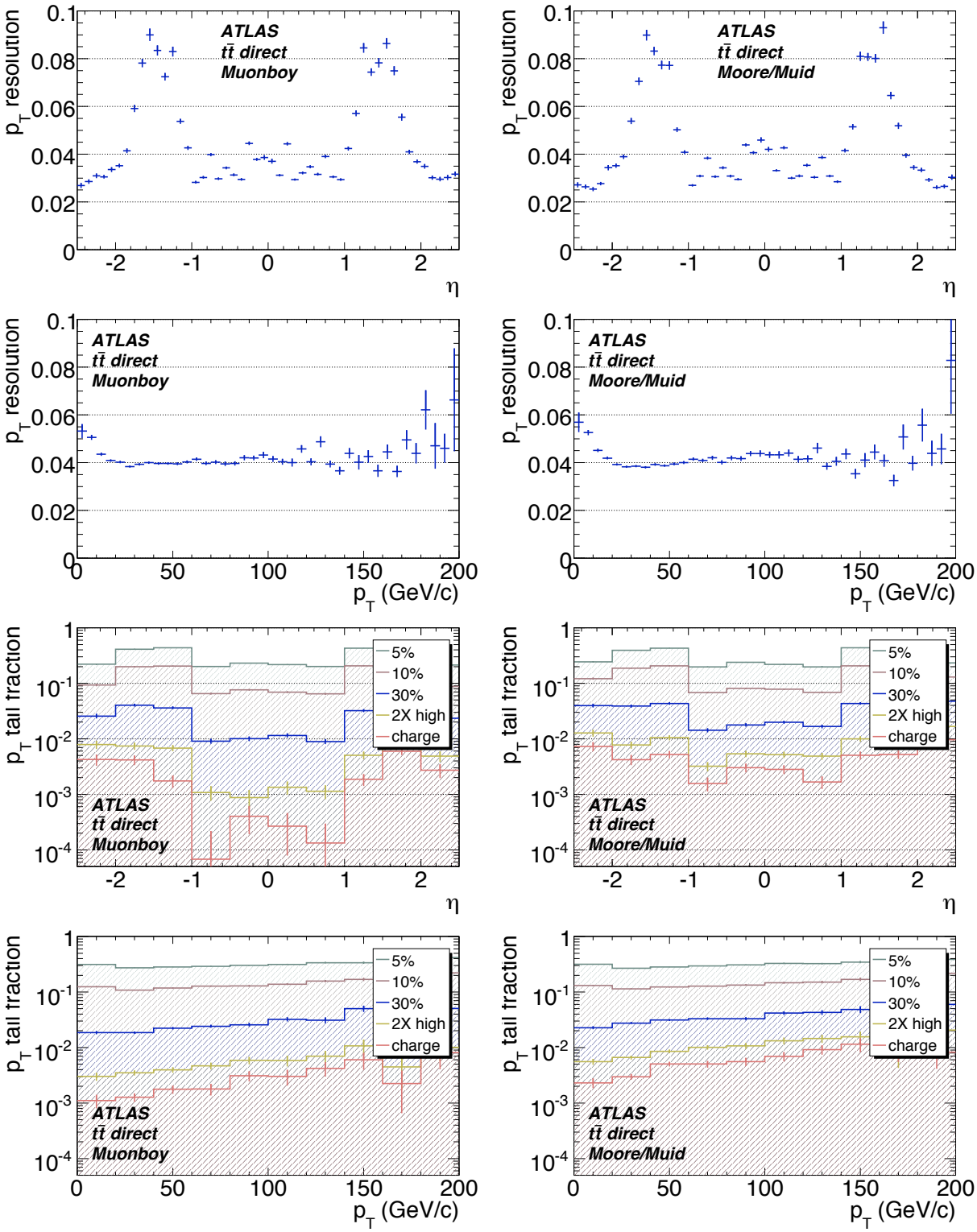

Figure 7: Standalone fractional momentum resolution ($\Delta p_T/p_T$) as function of η (top) and p_T (2nd row) and tails in that parameter also as functions of η (3rd row) and p_T (bottom). All are for both Muonboy (left) and Moore/Muid (right). The tail is the fraction of reconstructed muons with magnitude of $\Delta p_T/p_T$ outside a range and is shown for a wide range of values. The last tail curve (red, "charge") includes only muons reconstructed with the wrong charge sign. The 4th tail curve (yellow, "2X high") includes these and those with momentum magnitude more than two times the true value.

5.3 Resonances

The performance for decays of resonances into dimuon final states has been studied using samples of J/ψ, Z^0 and Z' ($M = 2$ TeV) decays. Dimuons are formed from all pairs of opposite-sign muons passing the selection criteria mentioned above. A single Gaussian is fit to the dimuon mass residual distribution as shown in Fig. 8. As visible in the figure, the residual distributions are not adequately described by a single Gaussian. Deviations from the single Gaussian are most pronounced at high-momentum. The performance extracted from the residual distributions is summarized in Table 7. In particular, the departure from a Gaussian distribution is evident in the large fraction of dimuons beyond 2- and 5-sigmas from the mean.

Table 7: Properties of reconstructed J/ψ, Z^0 and Z' ($M = 2$ TeV) dimuon resonances: Gaussian mean μ and width σ, fraction of dimuons with mass more than 2 and 5 σ away from the mean, and number of dimuons in a fixed-width interval about the mean (corresponding approximately to an interval of $\pm 2\sigma$). The efficiency is computed by dividing this number by the number of true resonances with both true muons in the range $|\eta| < 2.7$.

J/ψ	Muonboy	Moore/Muid
μ (MeV)	54.6 ± 2.9	14.5 ± 2.7
σ (MeV)	444.4 ± 2.6	367.4 ± 2.4
Fraction with $\lvert M-\mu\rvert > 2\sigma$	$(7.62 \pm 0.16)\%$	$(8.33 \pm 0.19)\%$
Fraction with $\lvert M-\mu\rvert > 5\sigma$	$(0.266 \pm 0.031)\%$	$(0.62 \pm 0.05)\%$
# dimuons with $\lvert M-\mu\rvert < 0.8$ GeV	25500	19583
efficiency	$(66.23 \pm 0.24)\%$	$(50.86 \pm 0.25)\%$
Z^0	Muonboy	Moore/Muid
μ (MeV)	67 ± 11	-83 ± 10
σ (MeV)	3273 ± 13	3153 ± 12
Fraction with $\lvert M-\mu\rvert > 2\sigma$	$(15.25 \pm 0.11)\%$	$(16.05 \pm 0.11)\%$
Fraction with $\lvert M-\mu\rvert > 5\sigma$	$(3.52 \pm 0.06)\%$	$(3.98 \pm 0.06)\%$
# dimuons with $\lvert M-\mu\rvert < 6.0$ GeV	91930	90346
efficiency	$(79.02 \pm 0.12)\%$	$(77.66 \pm 0.12)\%$
Z' ($M = 2$ TeV)	Muonboy	Moore/Muid
μ (MeV)	$(-3.7 \pm 2.1) \times 10^3$	$(1.8 \pm 2.1) \times 10^3$
σ (MeV)	$(159.2 \pm 3.2) \times 10^3$	$(155.7 \pm 3.4) \times 10^3$
Fraction with $\lvert M-\mu\rvert > 2\sigma$	$(19.61 \pm 0.45)\%$	$(24.49 \pm 0.50)\%$
Fraction with $\lvert M-\mu\rvert > 5\sigma$	$(6.29 \pm 0.28)\%$	$(9.75 \pm 0.35)\%$
# dimuons with $\lvert M-\mu\rvert < 300$ GeV	6055	5490
efficiency	$(68.06 \pm 0.49)\%$	$(61.71 \pm 0.52)\%$

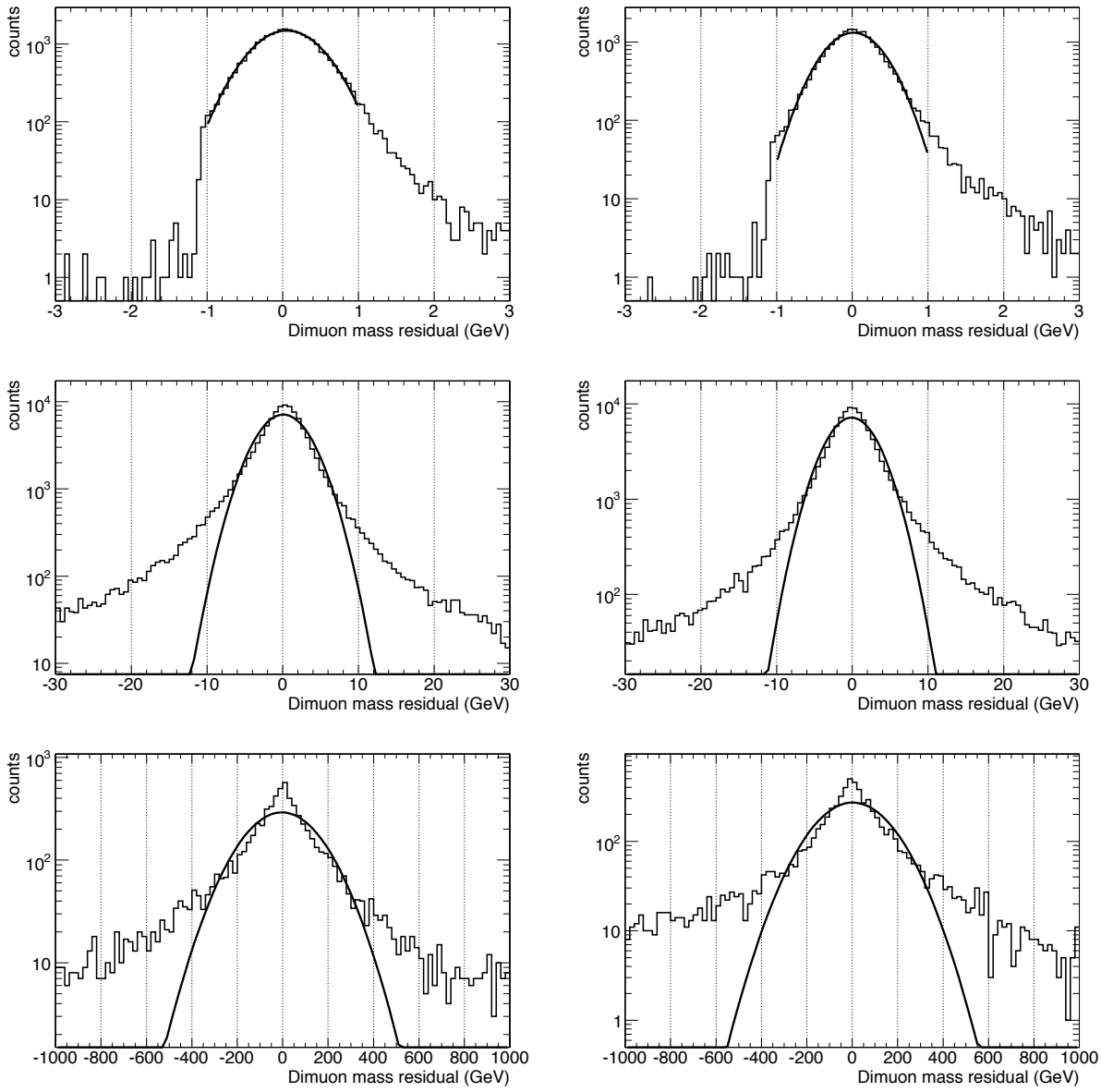

Figure 8: Dimuon mass residual distributions for J/ψ (top row), Z^0 (middle row), and Z' (bottom row). The function corresponds to the result of a fit to a single Gaussian. Results are shown for both Muonboy (left) and Moore/Muid (right).

6 Inner detector performance

Figure 9 shows the efficiency for $t\bar{t}$ direct muons and Table 8 gives the integrated efficiencies for all of the samples. The efficiency is high for all η (within the acceptance) and all samples. There is no evidence of degradation when pileup is added.

The inner detector momentum resolution is the same as that for tagged muons, reported later: see Figure 17 in section 8.

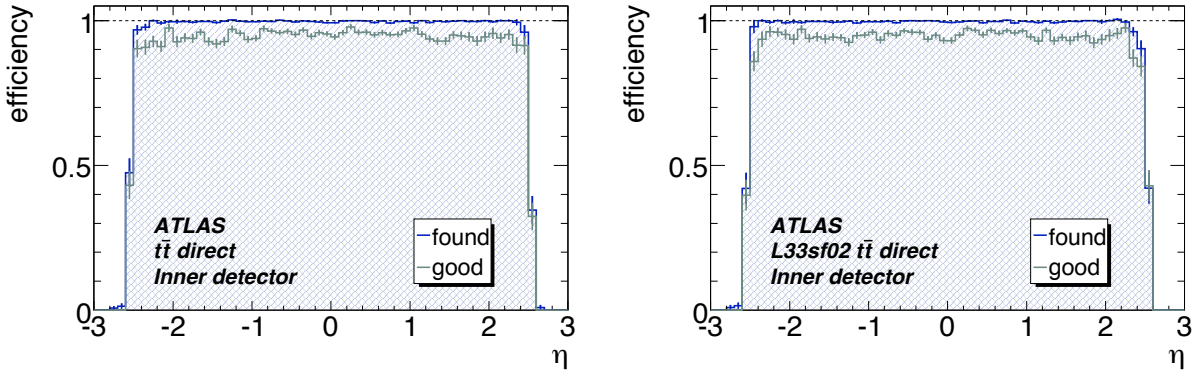

Figure 9: Inner detector $t\bar{t}$ direct muon efficiency as a function of true η at low (left) and high (right) luminosity. In each figure, the upper curve (blue) is the efficiency to find the muon while the lower curve (green) additionally requires a good match ($D_{eva} < 4.5$) between reconstructed and true track parameters. The efficiency is for $p_T > 10$ GeV/c.

	Efficiency	
Sample	found	good
$t\bar{t}$ direct	0.996 (1)	0.950 (2)
$t\bar{t}$ indirect	0.997 (1)	0.833 (5)
hi-$\mathscr{L}$ $t\bar{t}$ direct	0.995 (1)	0.947 (2)
Zprime direct	0.993 (1)	0.966 (1)
J/ψ	0.995 (1)	0.941 (3)

Table 8: Inner detector efficiencies. The samples and algorithms are described in the text. Efficiencies are presented both for all found muons and for those with a good truth match ($D_{eva} < 4.5$). Efficiencies are calculated for true muons with $|\eta| < 2.5$ and $p_T > 10$ GeV/c.

7 Combined muon performance

The combined performance algorithms match muon candidates from standalone reconstruction with tracks found in the inner detector. This combination is expected to have high purity because the calorimeter filters out nearly all of the charged particles that are not muons while the requirement of an inner detector track eliminates most of the muons produced away from the interaction point. It should also eliminate many of the combinatoric fakes that may arise in the muon spectrometer especially where the number of measurements is small. The precision of a combined measurement is superior to either component.

Here we evaluate the performance for two algorithms: Staco which makes use of the standalone spectrometer muon produced by Muonboy and Muid which starts from the standalone muon produced by Moore. Both make use of the inner detector tracks provided by the default inner detector reconstruction algorithm.

7.1 Efficiencies and fake rates

Figure 10 shows the combined $t\bar{t}$ direct muon efficiency and fake rates for each algorithm as a function of η for both low and high luminosity. Compared with the performance for standalone muons (figure 6), Staco shows a small drop in efficiency with little reduction of the fake rate except for the lowest p_T threshold at high luminosity. In fact, the high-p_T fake rates increase at either luminosity because low-p_T standalone muons are matched to high-p_T inner-detector tracks. At low luminosity, Muid $t\bar{t}$ shows a small decrease in both efficiency and fake rate. When background is added, the dramatic increase in fakes for Moore standalone is not observed in Muid combined, i.e. the matching suppresses most of the fakes and the Muid high-p_T fake rates are lower that those of Staco. However, the high-luminosity $t\bar{t}$ Muid efficiency is significantly worse than that of Staco.

When matching inner detector and muon spectrometer tracks, both Staco and Muid calculate χ^2_{match} (section 3.3) which serves as discriminant for separating real and fake muons. The fakes include pion or kaon decays in or near the calorimeter. Figure 11 shows the χ^2_{match} distributions for both direct found muons and fakes. We see that with a cut on this quantity, e.g. $\chi^2_{match} < 100$, many of the Staco high-p_T fakes can be suppressed with only a modest loss in efficiency. The higher Staco fake rates come from looser cuts during reconstruction and, if the χ^2_{match} cuts are adjusted to give the same efficiencies, the Staco fake rate is lower.

Table 9 shows the integrated Staco and Muid muon efficiencies and fake rates for all samples including an entry showing the effect of the above cut on χ^2_{match}.

7.2 Resolution

Figure 12 shows the $t\bar{t}$ direct muon p_T resolutions and tails as functions of η and p_T. Comparing with the same for standalone reconstruction (figure 7), we see, as expected, the combined resolution is significantly better especially in the overlap region ($|\eta|$ around 1.5) and for p_T below 100 GeV/c. There are also significant reductions in the tails of momentum residuals. Misreconstruction and charge misidentification rates are around 0.01% for the combined muons instead of 0.1% for the standalone.

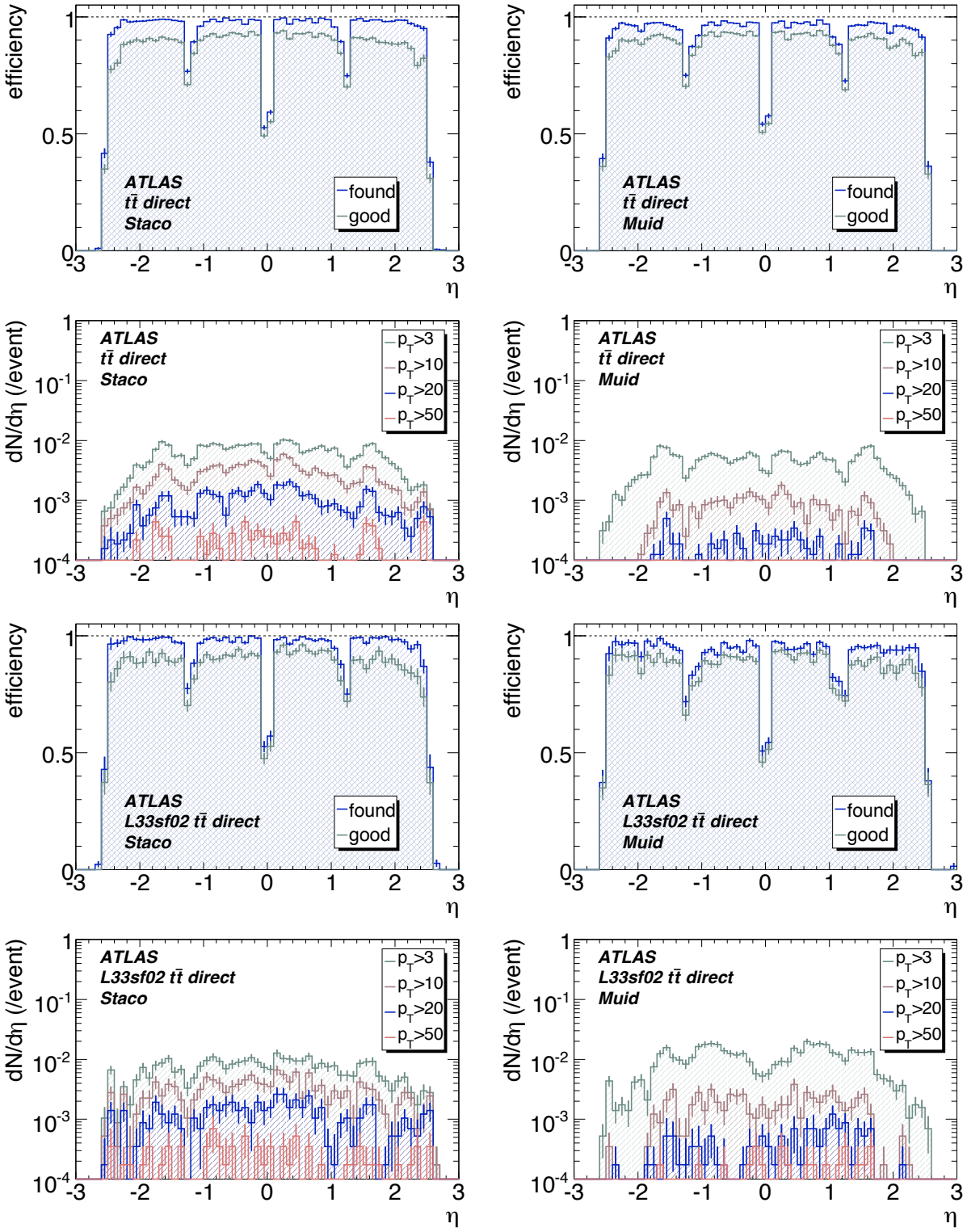

Figure 10: Combined muon efficiency and fake rate for Staco (left) and Muid (right) as functions of true η for direct muons in $t\bar{t}$ at low (top) and high (bottom) luminosity. In each efficiency plot, the upper curve (blue) is the efficiency to find the muon while the lower curve (green) additionally requires a good match ($D_{eva} < 4.5$) between reconstructed and true track parameters. The efficiencies are for $p_T > 10$ GeV/c. Fake rates are shown for a variety of p_T thresholds.

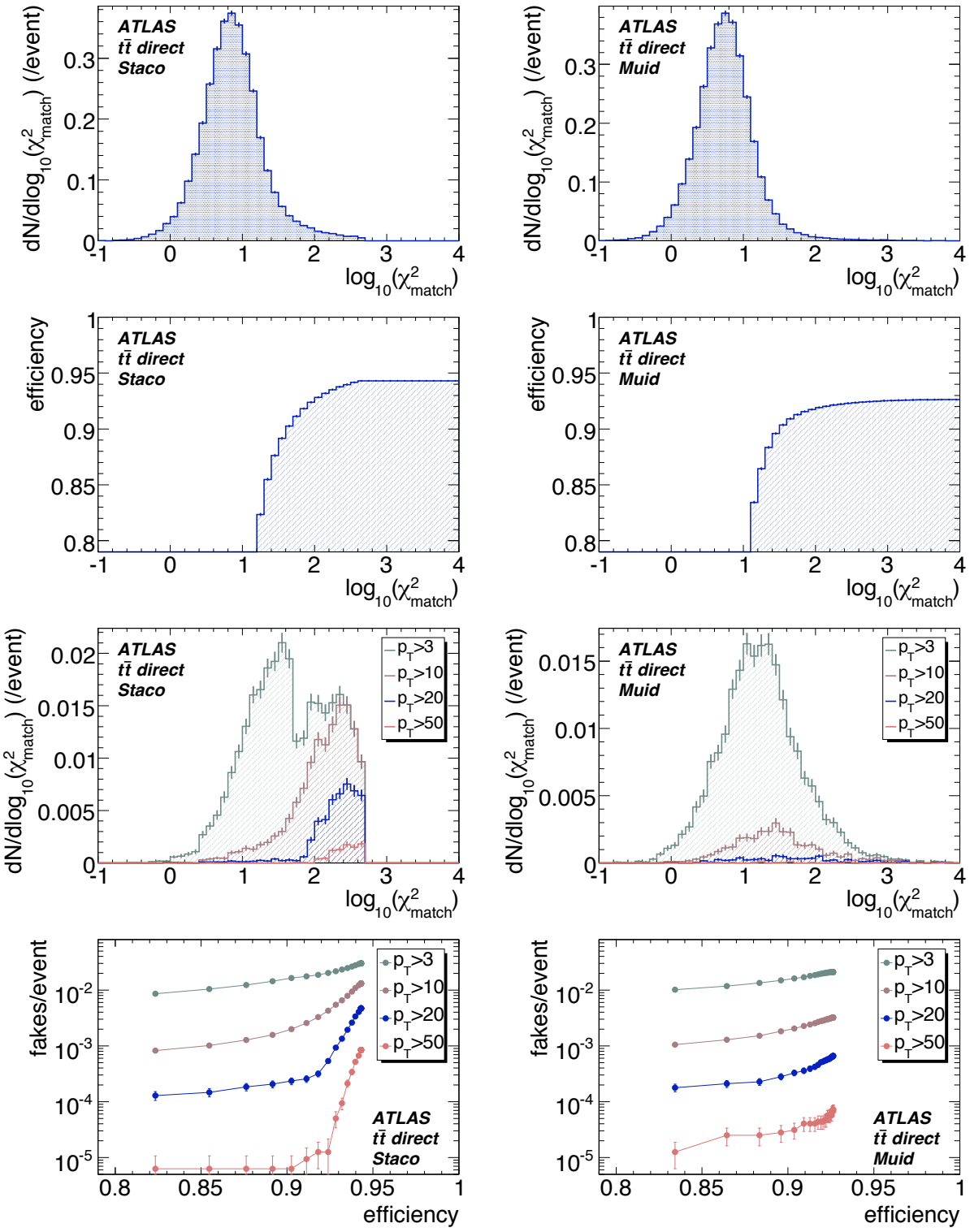

Figure 11: Distributions of χ^2_{match} for direct muons (top) and fakes (third from top). The fakes are shown for a variety of p_T thresholds. The second row shows the efficiency as function of χ^2_{match} when muons above that value are rejected. The bottom row shows the fake rates as a function of efficiency as that threshold is varied. All are shown for both Staco (left) and Muid (right). The sharp drops in the Staco χ^2_{match} distribution come from cuts on that quantity made during reconstruction, i.e. before filling the output muon collection.

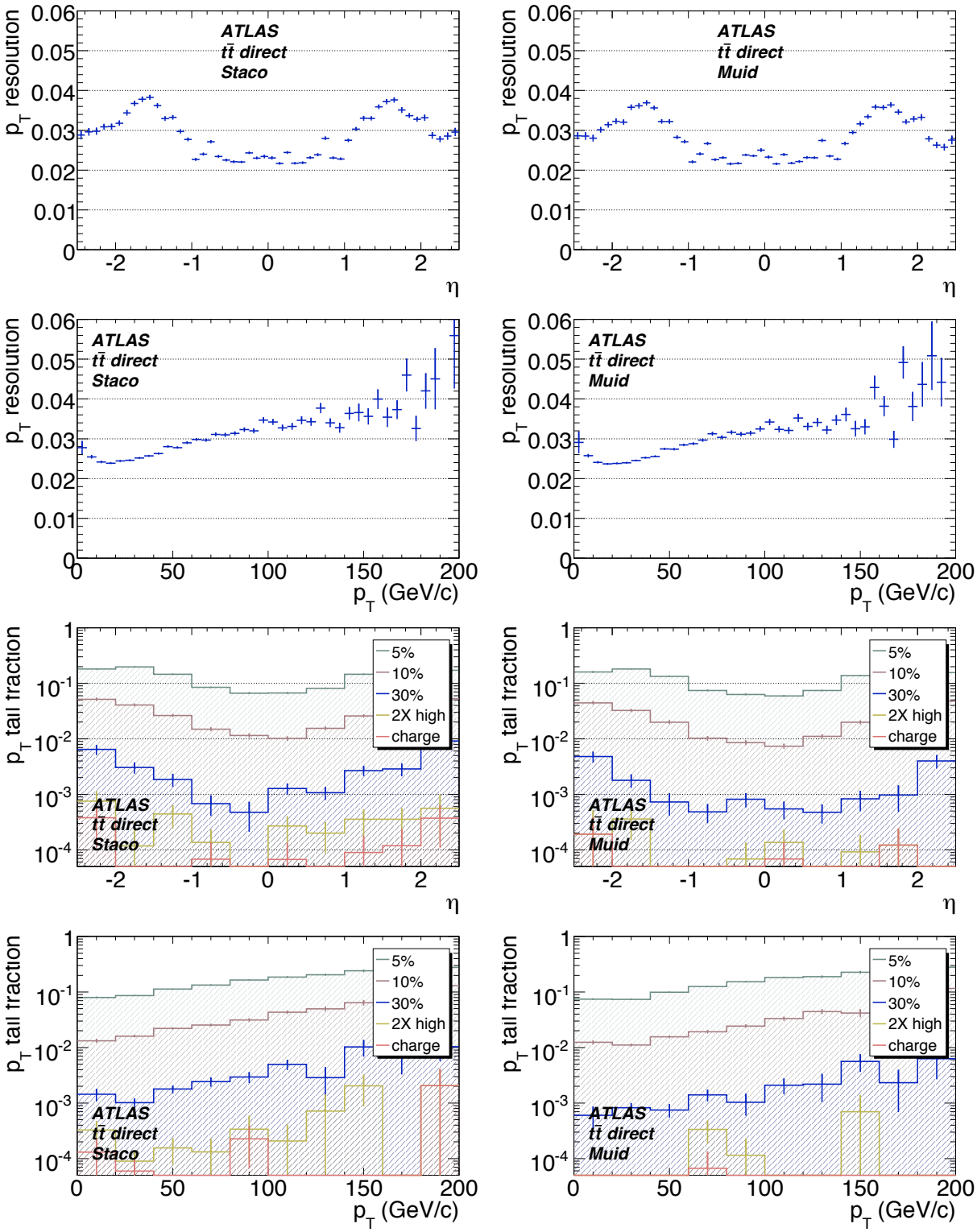

Figure 12: Combined muon fractional momentum resolution ($\Delta p_T/p_T$) as function of η (top) and p_T (2nd row) and tails in that parameter also as functions of η (3rd row) and p_T (bottom). All are for both Staco (left) and Muid (right). The tail is the fraction of reconstructed muons with magnitude of $\Delta p_T/p_T$ outside a range and is shown for a wide range of values. The last tail curve (red, "charge") includes only muons reconstructed with the wrong charge sign. The 4th tail curve (yellow, "2X high") includes these and those with momentum magnitude more than two times the true value.

Sample	Efficiency found	Efficiency good	Fakes/(1000 events) above p_T limit (GeV/c) 3	10	20	50
Staco						
$t\bar{t}$ direct $t\bar{t}$ indirect	0.943 (1) 0.933 (1)	0.875 (1) 0.767 (2)	22.0 (3)	9.6 (2)	3.4 (1)	0.62 (4)
$t\bar{t}$ direct cut	0.924 (1)	0.865 (1)	14.8 (2)	3.1 (1)	0.39 (3)	0.01 (1)
hi-$\mathscr{L}$ $t\bar{t}$ direct	0.941 (2)	0.871 (3)	25.9 (7)	11.2 (4)	4.3 (3)	0.7 (1)
Z'	0.910 (2)	0.824 (3)	14 (1)	8.4 (9)	5.2 (7)	3.4 (6)
J/ψ	0.943 (3)	0.873 (4)	0.9 (2)	0.24 (8)	0.11 (5)	0.0 (0)
Muid						
$t\bar{t}$ direct $t\bar{t}$ indirect	0.926 (1) 0.888 (2)	0.877 (1) 0.748 (3)	15.4 (2)	2.36 (9)	0.48 (4)	0.05 (1)
$t\bar{t}$ direct cut	0.917 (1)	0.871 (1)	14.0 (2)	1.96 (8)	0.33 (3)	0.03 (1)
hi-$\mathscr{L}$ $t\bar{t}$ direct	0.904 (2)	0.854 (3)	35.5 (8)	5.0 (3)	1.1 (1)	0.24 (6)
Z' direct	0.872 (2)	0.811 (3)	11 (1)	4.5 (7)	3.1 (6)	2.7 (5)
J/ψ	0.793 (5)	0.741 (6)	0.8 (1)	0.03 (3)	0.0 (0)	0.0 (0)

Table 9: Staco and Muid efficiencies and fake rates. The samples and algorithms are described in the text. Algorithm names are followed by "cut" to indicate that reconstructed muons are required to have $\chi^2_{match} < 100$ for both efficiency and fake calculations. Efficiencies are presented both for all found muons and for those with a good truth match. Both are calculated for true muons with $|\eta| < 2.5$ and $p_T > 10$ GeV/c. The fake rates are presented for a variety of p_T thresholds.

7.3 Resonances

The performance for decays of resonances into dimuon final states has been studied using samples of J/ψ, Z^0 and Z' ($M = 2$ TeV) decays. Dimuons are formed from all pairs of opposite-sign muons passing the selection criteria mentioned above. A single Gaussian is fit to the dimuon mass residual distribution as shown in Fig. 13. As visible in the figure, the residual distributions are not adequately described by a single Gaussian. Deviations from the single Gaussian are most pronounced at high-momentum. The performance extracted from the residual distributions is summarized in Table 10. In particular, the departure from a Gaussian distribution is evident in the large fraction of dimuons beyond 2- and 5-sigmas from the mean.

Table 10: Properties of reconstructed J/ψ, Z^0 and Z' ($M = 2$ TeV) dimuon resonances: Gaussian mean μ and width σ, fraction of dimuons with mass more than 2 and 5 σ away from the mean, and number of dimuons in a fixed-width interval about the mean (corresponding approximately to an interval of $\pm 2\sigma$). The efficiency is computed by dividing this number by the number of true resonances with both true muons in the range $|\eta| < 2.5$.

J/ψ	Staco	Muid
μ (MeV)	6.66 ± 0.41	-0.97 ± 0.44
σ (MeV)	60.46 ± 0.38	61.12 ± 0.42
Fraction with $\lvert M-\mu\rvert > 2\sigma$	$(10.20 \pm 0.19)\%$	$(10.07 \pm 0.21)\%$
Fraction with $\lvert M-\mu\rvert > 5\sigma$	$(0.93 \pm 0.06)\%$	$(0.89 \pm 0.07)\%$
# dimuons with $\lvert M-\mu\rvert < 0.12$ GeV	21802	18139
efficiency	$(56.72 \pm 0.25)\%$	$(47.19 \pm 0.25)\%$
Z^0	Staco	Muid
μ (MeV)	102 ± 6	-3 ± 6
σ (MeV)	1874 ± 6	1790 ± 6
Fraction with $\lvert M-\mu\rvert > 2\sigma$	$(9.57 \pm 0.09)\%$	$(9.44 \pm 0.09)\%$
Fraction with $\lvert M-\mu\rvert > 5\sigma$	$(0.934 \pm 0.031)\%$	$(0.600 \pm 0.025)\%$
# dimuons with $\lvert M-\mu\rvert < 4.0$ GeV	89599	89395
efficiency	$(85.44 \pm 0.11)\%$	$(85.25 \pm 0.11)\%$
Z' ($M = 2$ TeV)	Staco	Muid
μ (MeV)	$(-3.4 \pm 1.7) \times 10^3$	$(7.3 \pm 1.7) \times 10^3$
σ (MeV)	$(134.8 \pm 2.1) \times 10^3$	$(126.4 \pm 2.0) \times 10^3$
Fraction with $\lvert M-\mu\rvert > 2\sigma$	$(13.46 \pm 0.40)\%$	$(12.38 \pm 0.40)\%$
Fraction with $\lvert M-\mu\rvert > 5\sigma$	$(2.08 \pm 0.17)\%$	$(1.91 \pm 0.17)\%$
# dimuons with $\lvert M-\mu\rvert < 250$ GeV	6156	5745
efficiency	$(71.29 \pm 0.49)\%$	$(66.53 \pm 0.51)\%$

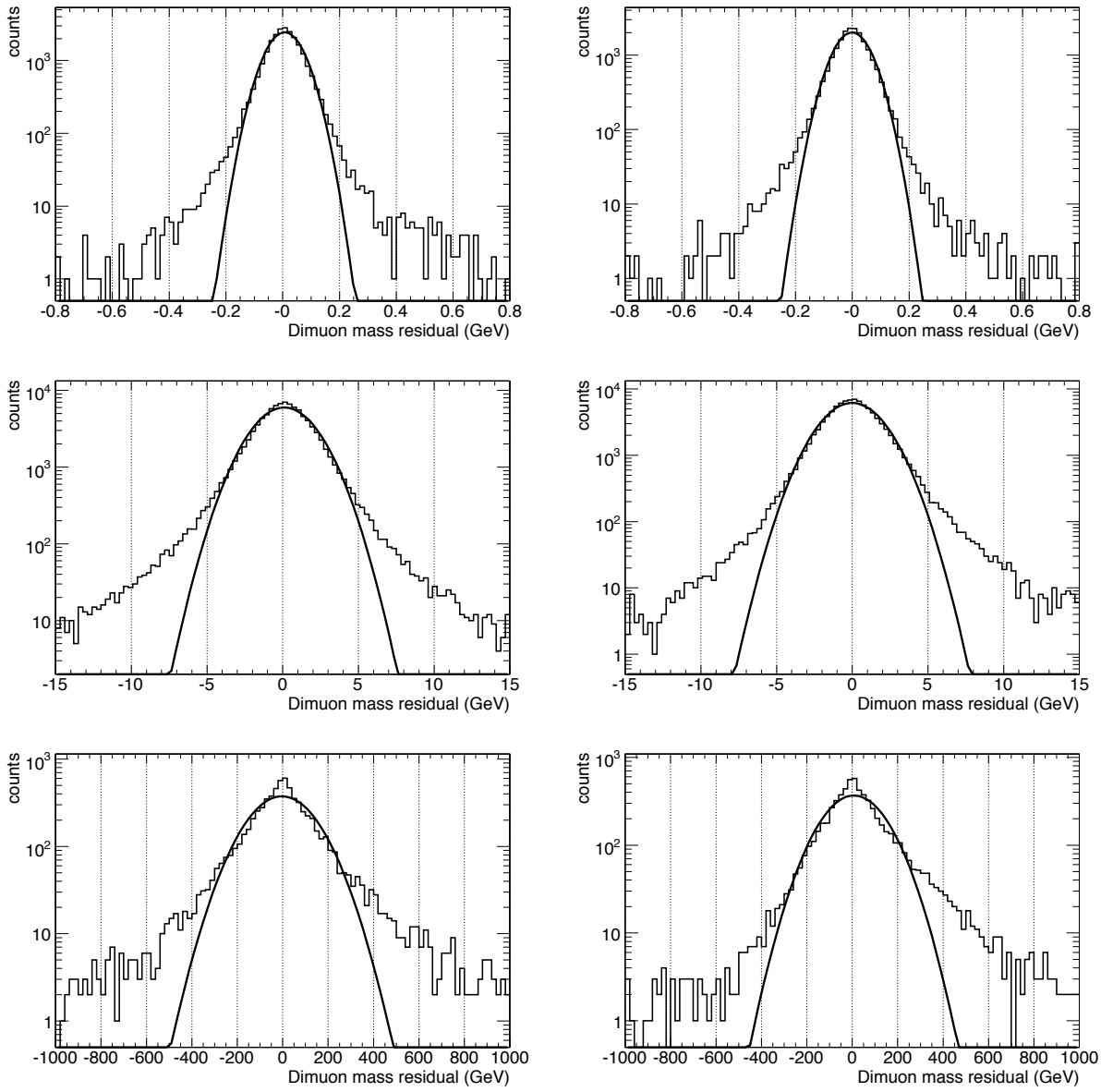

Figure 13: Dimuon mass residual distributions for J/ψ (top row), Z^0 (middle row), and Z' (bottom row). The function corresponds to the result of a fit to a single Gaussian. Results are shown for both Staco (left) and Muid (right).

7.4 Impact of inner detector tracking algorithms on muon performance

There are three algorithms for pattern recognition and track fitting in the ATLAS Inner Detector (ID), namely *iPatRec* [15], *xKalman* [16] and *newTracking* or *NewT* [17]. The first two have been part of the inner detector track reconstruction repository since pre-TDR days. *NewT* has been relatively recently introduced and is the default algorithm used in Athena-based event reconstruction. All three are road-based inside-out algorithms, starting with combinations of space-points in the Pixel and SCT subdetectors, forming track candidates, and extrapolating the candidates into the TRT. But they differ in the fitting procedure used and the rigor of the fit.

Given the differences among the three algorithms, it is possible that they will differ in their performance. The performance of the three algorithms was evaluated with respect to muon tracks. The details of the study can be found in [18].

The objectives of the study were twofold:

- To provide muon-physics performance comparison among the ID algorithms: a track reconstructed in the Muon Spectrometer (MS) is combined with a corresponding track in the ID whenever possible. Therefore, the relative performances of the ID reconstruction algorithms are relevant to muon reconstruction, and a comparison of their performance is warranted.

- To evaluate performance degradation in the presence of cavern background and event pileup: during a physics run, the ATLAS cavern will have a diffuse background of neutral particles. In addition, multiple interactions in a single bunch crossing will lead to event pileup. It is essential to understand how much these factors can affect the performance of the ID reconstruction algorithms.

We used a $t\bar{t} \rightarrow lepton + jets$ sample for our study. The choice of this sample was motivated by three reasons. Firstly, semileptonic $t\bar{t}$ events contain muons with a wide range of transverse momenta: high-P_T isolated muons from W decays as well as low-P_T, non-isolated muons in b-jets. Secondly, these events have a fairly high track density in the inner region, which imposes stringent requirements on ID track reconstruction algorithms. Thirdly the high track density in jets presents a potential source of fake muons, for example, from punch-through pions/kaons.

We used two $t\bar{t}$ samples from the official CSC production dataset '5200'. One of these was a signal-only sample, while the other had cavern background and pileup added to the signal ('*cavbgSF05*' hereafter). Both samples were generated with the Herwig Monte Carlo package using the Jimmy library, and MC@NLO for matrix element calculation. The *signal-only* dataset we used was:

csc11.005200.T1_McAtNlo_Jimmy.digit.v11004205,

simulated and digitized with *Athena* version 11.0.42. The *cavbgSF05* dataset we used was:

pile1sf05_misal1_csc11.005200.T1_McAtNlo_Jimmy.digit.v12000502,

simulated and digitized with *Athena* version 12.0.5.

In order to compare the performance of the three ID tracking algorithms, we adopted the following approach: reconstruct each muon track three times, each time using a different ID algorithm but the same MS algorithm. Since the same MS algorithm is used in all cases, it is reasonable that any difference in performance seen among the three reconstruction paths results from the performance of the ID algorithms only.

For combined track reconstruction, we used the *STACO* package (see Sec. 2.3.2). Using *Athena* version 12.0.52, we reconstructed 24000 events from the *signal-only* sample and 7200 events from the *cavbgSF05* sample. We used the *MuPerf* package (see Sec. 3) to analyze the reconstructed events. For each of the two samples, we studied the reconstruction efficiency, fake rates, and transverse momentum resolution for all *found* muons and for *good* muons, as defined in Sec. 3. The results of our study are summarized in tables 11 and 12. A few sample figures are also shown (figures 14 and 15).

Table 11: Summary of performance of the three reconstruction paths on the *signal-only* sample.

Algorithm	**iPatRec+STACO**	**xKalman+STACO**	**newTracking+STACO**
Overall efficiency	0.888 ± 0.006	0.887 ± 0.006	0.886 ± 0.006
Overall good efficiency	0.806 ± 0.005	0.807 ± 0.005	0.812 ± 0.005
Good fit χ^2/DOF	0.932 ± 0.006	0.934 ± 0.006	0.931 ± 0.006
Fakes/event	0.03 ± 0.01	0.03 ± 0.01	0.03 ± 0.01

Table 12: Summary of performance of the three reconstruction paths on the *cavbgSF05* sample.

Algorithm	**iPatRec+STACO**	**xKalman+STACO**	**newTracking+STACO**
Overall efficiency	0.87 ± 0.01	0.87 ± 0.01	0.87 ± 0.01
Overall good efficiency	0.771 ± 0.009	0.761 ± 0.009	0.773 ± 0.009
Good fit χ^2/DOF	0.87 ± 0.01	0.87 ± 0.01	0.87 ± 0.01
Fakes/event	0.04 ± 0.02	0.04 ± 0.02	0.04 ± 0.02

For the *signal-only* sample, none of the three reconstruction paths is seen to perform better than the others within statistical error. For example, the difference in efficiency between any two of the reconstruction paths is less than 1%, not large enough to favor one path over another. We conclude that, for the *signal-only* sample, the three ID reconstruction algorithms perform at the same level with respect to muon tracks.

The same conclusion can be drawn for all *found* muons in the *cavbgSF05* sample. In the presence of cavern background and pileup, the *NewT + STACO* reconstruction path has lower efficiency, higher fake rates and worse resolution than for the *signal-only* case. The overall decrease in efficiency is found to be $\approx$2%. Fake rates are higher by $\approx$15%, while P_T resolution suffers by $\approx$10%. This performance degradation is also seen for the other two reconstruction paths.

Repeating the study on *good* muons in the *cavbgSF05* sample leads to the same general conclusion, namely that the three ID reconstruction algorithms perform on a par for muon tracks. A comparison of the performances of the *signal-only* sample and the *cavbgSF05* sample shows that the overall decrease in efficiency is $\approx$5% for the latter with respect to the former. Degradation of fake rates and P_T resolution are similar to the case of all *found* muons.

In summary, for both the signal-only sample and the sample with cavern background and pileup added, our conclusion is that the three inner detector algorithms perform similarly within statistical error, and that it is unlikely that, even with higher statistics, we should see any one algorithm performing significantly better than the other two. In the presence of cavern background and pileup, the performance of all three algorithm paths degrades considerably, but we note that the degradation is most likely due to the muon spectrometer track reconstruction (see section 4).

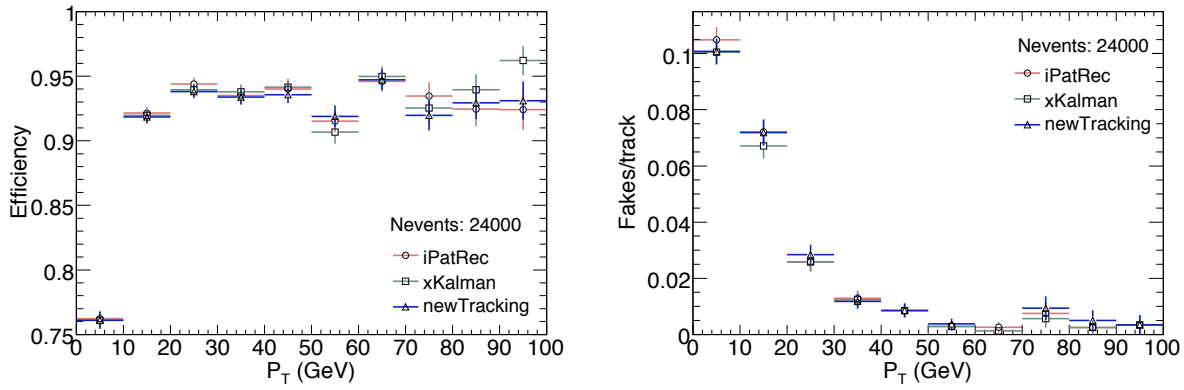

Figure 14: Efficiency and fake rate vs. muon P_T for the three reconstruction paths for the *signal-only* sample.

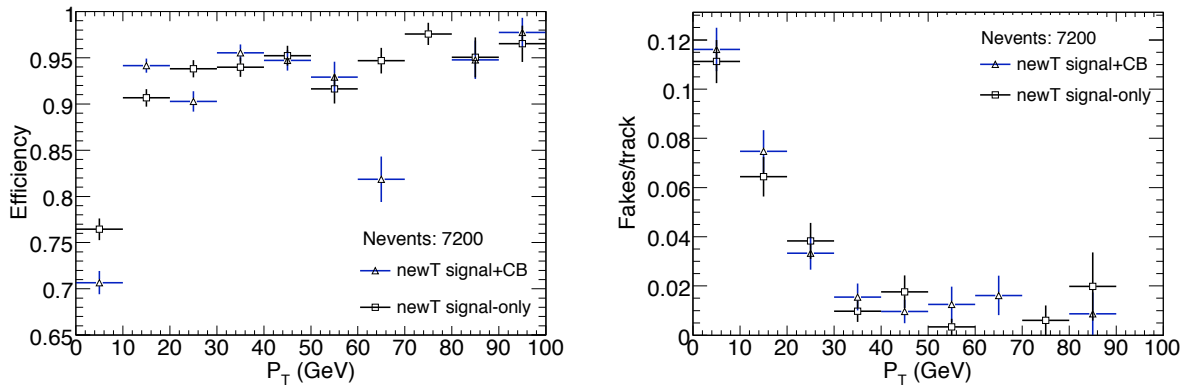

Figure 15: Comparisons of efficiency (left) and fake rate per track (right) vs muon p_T between the *signal-only* and the *cavbgSF05* samples for the *NewT+STACO* reconstruction path.

8 Tagged muon performance

ATLAS currently supports several independent algorithms that tag inner detector tracks using muon spectrometer hits or segments: MuTag, MuTagIMO and MuGirl. However, only MuTag and MuGirl were available in release 12.0.6 studied here. MuTag is intended only to supplement the collection of muon found by Staco and so only makes use of the inner detector tracks and muon spectrometer segments that are not already used in any of the Staco tracks. MuGirl has no such restriction and attempts to find all muons or at least all within the common acceptance of the inner detector and muon spectrometer.

The performance of the combinations Staco+MuTag and Muid+MuGirl will be discussed in a later section. Here we examine the performance of MuGirl by itself.

8.1 Efficiencies and fake rates

Figure 16 shows the MuGirl direct muon efficiency and fake rates as a function of η in $t\bar{t}$ at low and high luminosity. Table 13 gives the MuGirl integrated efficiencies and fake rates for all our samples.

Comparing with the combined muon results (figure 10 and table 9), we see that MuGirl has lower efficiency and a substantially higher fake rate. We also observe that its performance degrades faster when luminosity background is added. MuGirl has higher efficiency than Muid for reconstructing the low-p_T muons in the J/ψ sample.

	Efficiency		Fakes/(1000 events) above p_T limit (GeV/c)			
Sample	found	good	3	10	20	50
$t\bar{t}$ direct	0.911 (1)	0.870 (1)	105.0 (6)	23.7 (3)	7.3 (2)	1.14 (6)
$t\bar{t}$ indirect	0.899 (2)	0.748 (3)				
hi-$\mathscr{L}$ $t\bar{t}$ direct	0.866 (3)	0.825 (3)	154 (2)	26.1 (7)	7.6 (4)	1.2 (1)
Z' direct	0.802 (3)	0.781 (3)	57 (2)	26 (2)	15 (1)	5.9 (8)
J/ψ c-quark	0.888 (4)	0.839 (5)	4.4 (3)	0.11 (5)	0 (0)	0 (0)

Table 13: MuGirl efficiencies and fake rates. The samples and algorithms are described in the text. Efficiencies are presented both for all found muons and for those with a good truth match. Both are calculated for truth muons with $|\eta| < 2.5$ and $p_T > 10$ GeV/c. The fake rates are presented for a variety of p_T thresholds.

8.2 Resolution

Figure 17 shows the MuGirl p_T resolution and tail as functions of η and p_T. MuGirl does not refit the tracks and so this is just the resolution of the inner detector. Comparing with the standalone (figure 7) and combined (figure 12), we see how the standalone and inner measurements complement one another to give high precision over the full η and p_T range of the $t\bar{t}$ sample.

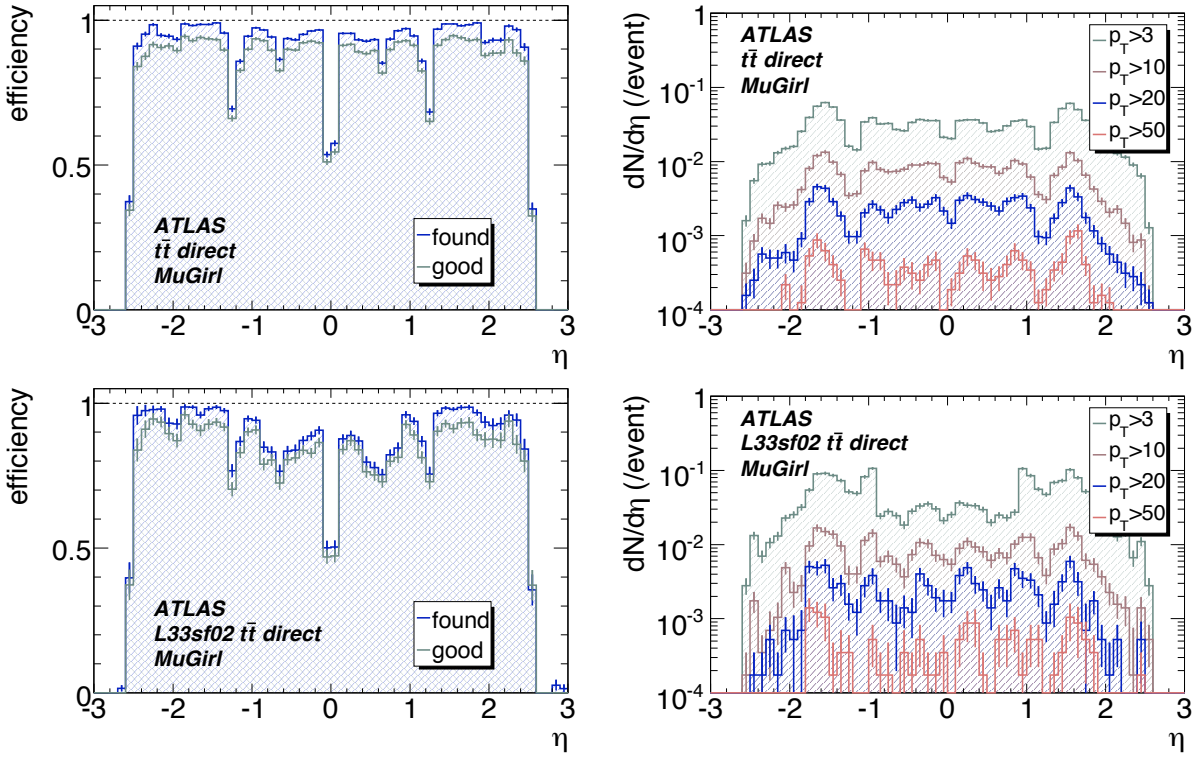

Figure 16: MuGirl efficiency (left) and fake rates (right) as a function of true η in $t\bar{t}$ at low (top) and high (bottom) luminosity. In each efficiency plot, the upper curve (blue) is the efficiency to find the muon while the lower curve (green) additionally requires a good match ($D_{eva} < 4.5$) between reconstructed and true track parameters. The efficiency is for muons with true $p_T > 10$ GeV/c. Fake rates are presented for a variety of p_T thresholds.

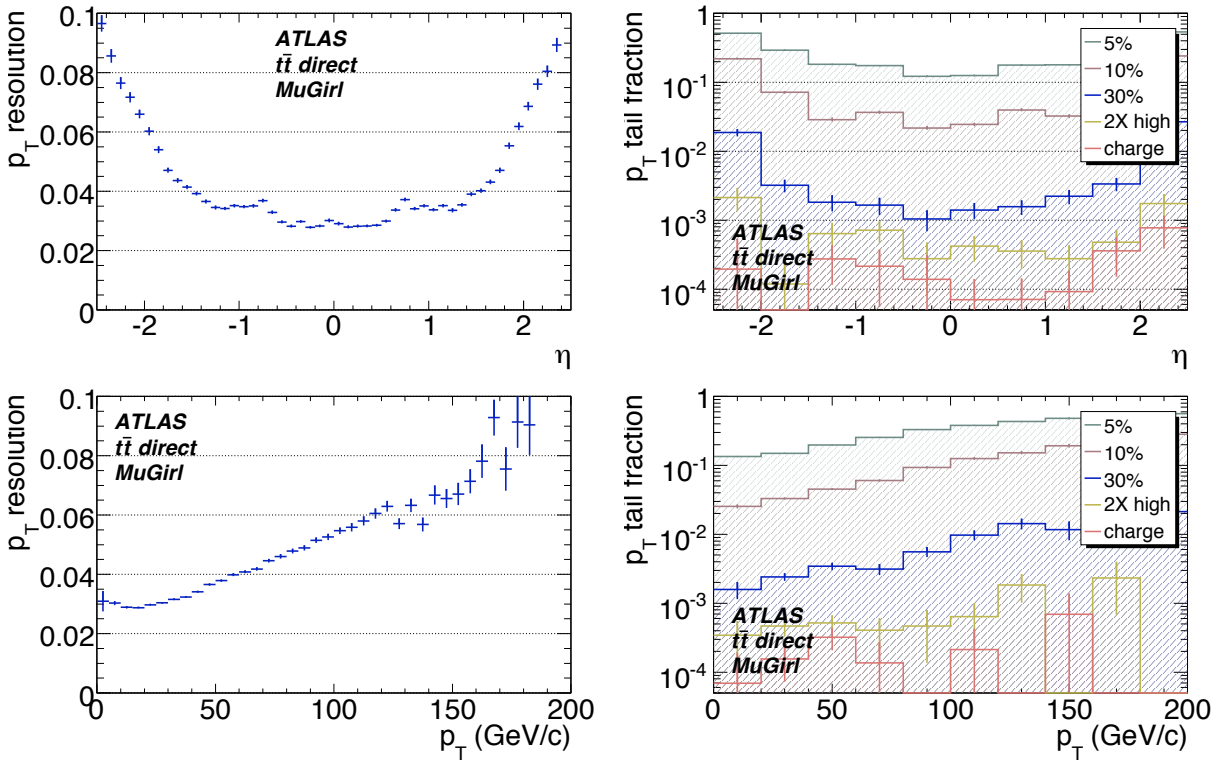

Figure 17: MuGirl fractional momentum resolution ($\Delta p_T / p_T$) as a function of η (top) and p_T (bottom). Both the distribution (left) and tails (right) are shown for each. The tail is the fraction of reconstructed muons with magnitude of residual greater than a threshold and results are shown for a variety of thresholds. The last tail curve (red, "charge") includes only muons reconstructed with the wrong charge sign. The 4th tail curve (yellow, "2X high") includes these and those with momentum magnitude more than two times the true value.

8.3 Resonances

The performance for decays of resonances into dimuon final states has been studied using samples of J/ψ, Z^0 and Z' ($M = 2$ TeV) decays. Dimuons are formed from all pairs of opposite-sign muons passing the selection criteria mentioned above. A single Gaussian is fit to the dimuon mass residual distribution as shown in Fig. 18. As visible in the figure, the residual distributions are not adequately described by a single Gaussian. Deviations from the single Gaussian are most pronounced at high-momentum. The performance extracted from the residual distributions is summarized in Table 14. In particular, the departure from a Gaussian distribution is evident in the large fraction of dimuons beyond 2- and 5-sigmas from the mean.

A significant asymmetry is observed in the residual distribution for the Z' sample. This is likely due to the large uncertainty in the curvature measurement in the inner detector at large momentum. Such large uncertainty results in an asymmetric momentum resolution.

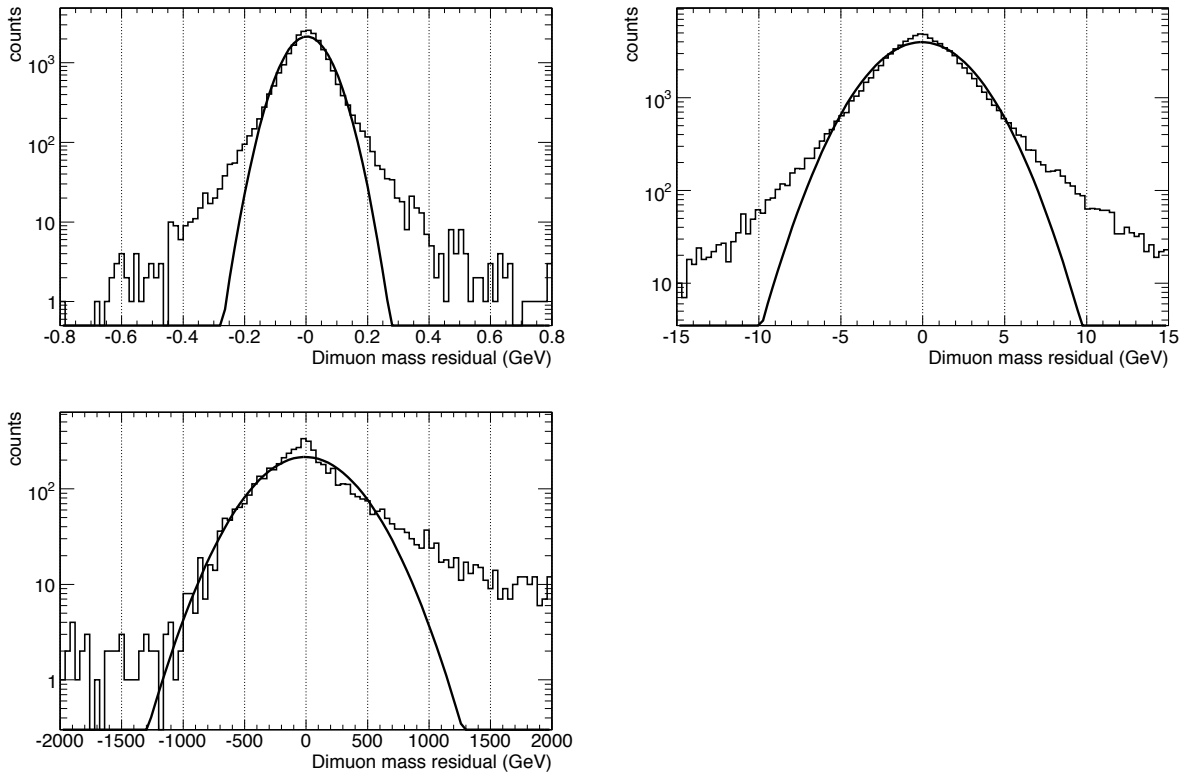

Figure 18: Dimuon mass residual distributions for J/ψ (top left), Z^0 (top right), and Z' (bottom left). The function corresponds to the result of a fit to a single Gaussian.

Table 14: Properties of reconstructed J/ψ, Z^0 and Z' ($M = 2$ TeV) dimuon resonances: Gaussian mean μ and width σ, fraction of dimuons with mass more than 2 and 5 σ away from the mean, and number of dimuons in a fixed-width interval about the mean (corresponding approximately to an interval of $\pm 2\sigma$). The efficiency is computed by dividing this number by the number of true resonances with both true muons in the range $|\eta| < 2.5$.

J/ψ	MuGirl
μ (MeV)	2.30 ± 0.45
σ (MeV)	67.01 ± 0.48
Fraction with $\lvert M-\mu\rvert > 2\sigma$	$(10.93 \pm 0.20)\%$
Fraction with $\lvert M-\mu\rvert > 5\sigma$	$(1.12 \pm 0.07)\%$
# dimuons with $\lvert M-\mu\rvert < 0.12$ GeV	20629
efficiency	$(53.67 \pm 0.25)\%$
Z^0	MuGirl
μ (MeV)	-59 ± 9
σ (MeV)	2606 ± 9
Fraction with $\lvert M-\mu\rvert > 2\sigma$	$(9.64 \pm 0.10)\%$
Fraction with $\lvert M-\mu\rvert > 5\sigma$	$(0.723 \pm 0.028)\%$
# dimuons with $\lvert M-\mu\rvert < 5.0$ GeV	81642
efficiency	$(77.85 \pm 0.13)\%$
Z' ($M = 2$ TeV)	MuGirl
μ (MeV)	$(-8 \pm 6) \times 10^3$
σ (MeV)	$(353 \pm 5) \times 10^3$
Fraction with $\lvert M-\mu\rvert > 2\sigma$	$(13.53 \pm 0.46)\%$
Fraction with $\lvert M-\mu\rvert > 5\sigma$	$(1.50 \pm 0.16)\%$
# dimuons with $\lvert M-\mu\rvert < 600$ GeV	4585
efficiency	$(53.1 \pm 0.5)\%$

9 Merged muon performance

Finally we consider merging the muons produced by different algorithms. There are many possible combinations but we restrict ourselves to two simple but important cases: merging the combined and tagged muons separately within each collection (family), i.e. we examine Staco+MuTag and Muid+MuGirl.

Figure 19 shows the corresponding direct muon efficiencies and fake rates in $t\bar{t}$ at low and high luminosity. The integrated efficiencies and fake rates for all samples are summarized in table 15. One of the primary goals of the tagging algorithms is to reconstruct low-p_T muons which the standalone reconstruction misses because the energy loss in the calorimeter leaves these muons with very little momentum in the muon spectrometer. Figure 20 shows the low-p_T efficiency as function of p_T for combined alone and combined supplemented with tagged for each of the collections.

The merge provides only a small improvement in the Staco efficiencies and a substantial increase in the fake rates (factor of about four). For Muid, the efficiency gains are more substantial: the indirect $t\bar{t}$ efficiency increases by 6% and the J/ψ by 15%. The fake rates are increased by a factor of five, i.e. slightly above the MuGirl rates. Overall, the Muid+MuGirl performance is very similar to that of Staco+MuTag. In both cases, we see the tagging algorithms do provide the significant efficiency improvement for p_T below 10 GeV/c.

Sample	Efficiency		Fakes/(1000 events) above p_T limit (GeV/c)			
	found	good	3	10	20	50
Staco+MuTag						
$t\bar{t}$ direct	0.948 (1)	0.879 (1)	49.0 (4)	14.4 (2)	4.8 (1)	0.86 (5)
$t\bar{t}$ indirect	0.940 (1)	0.772 (2)				
hi-$\mathscr{L}$ $t\bar{t}$ direct	0.946 (2)	0.876 (3)	58 (1)	16.6 (5)	6.1 (3)	1.1 (1)
Z' direct	0.931 (2)	0.844 (3)	32 (2)	14 (1)	7.1 (9)	4.2 (7)
J/ψ	0.954 (3)	0.883 (4)	2.5 (3)	0.3 (1)	0.11 (5)	0 (0)
Muid+MuGirl						
$t\bar{t}$ direct	0.955 (1)	0.903 (1)	113.1 (6)	24.9 (3)	7.6 (2)	1.17 (6)
$t\bar{t}$ indirect	0.946 (1)	0.790 (2)				
hi-$\mathscr{L}$ $t\bar{t}$ direct	0.952 (2)	0.898 (2)	181 (2)	29.8 (7)	8.4 (4)	1.2 (2)
Z' direct	0.929 (2)	0.866 (3)	61 (3)	28 (2)	16 (1)	7.5 (9)
J/ψ	0.946 (3)	0.885 (4)	4.7 (4)	0.11 (5)	0 (0)	0 (0)

Table 15: Staco+MuTag and Muid+MuGirl efficiencies and fake rates. The samples and algorithms are described in the text. Efficiencies are presented both for all found muons and for those with a good truth match. Both are calculated for truth muons with $|\eta| < 2.5$ and $p_T > 10$ GeV/c. The fake rates are presented for a variety of p_T thresholds.

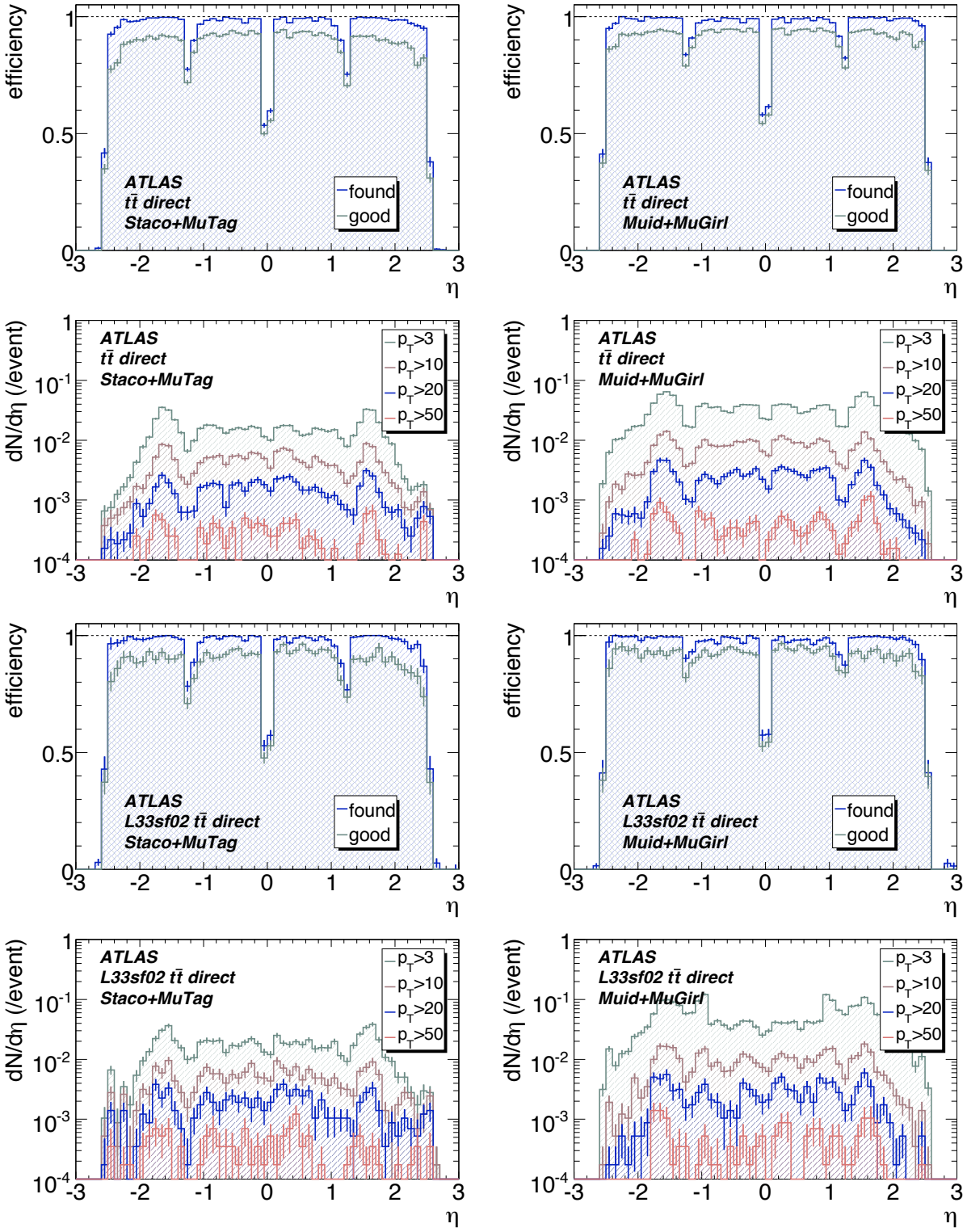

Figure 19: Muon efficiencies and fake rates for Staco+MuTag (left) and Muid+MuGirl (right) as functions of true η in $t\bar{t}$ at low (top) and high (bottom) luminosity. In each efficiency plot, the upper curve (blue) is the efficiency to find the muon while the lower curve (green) additionally requires a good match ($D_{eva} < 4.5$) between reconstructed and true track parameters. The muon selection is described in the text. The efficiency is calculated for true $p_T > 10$ GeV/c. The fake rates are presented for a variety of p_T thresholds.

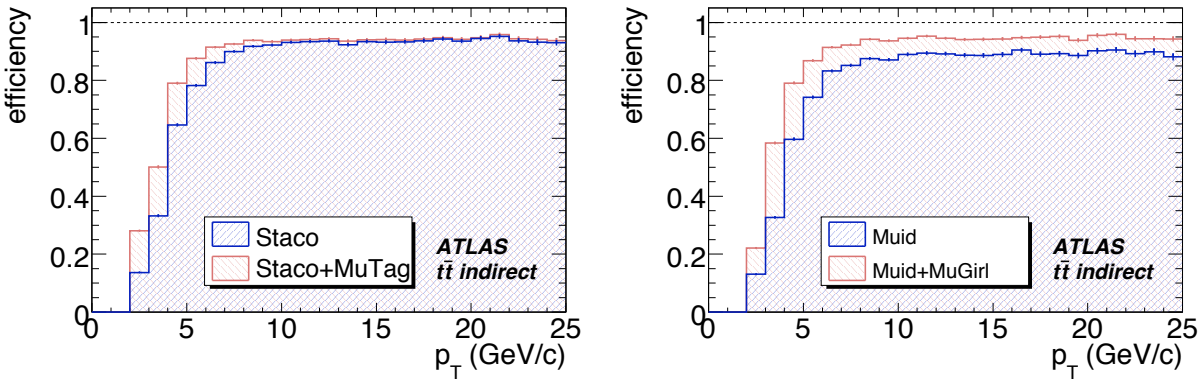

Figure 20: Low-p_T muon finding efficiencies for combined muons alone and combined plus tagged for the Staco (left) and Muid (right) collections. Results are show for the $t\bar{t}$ indirect selection. The other samples show similar behavior but have much poorer statistics at low-p_T. The efficiency is calculated for muons with $|\eta| < 2.5$.

10 Performance in physics analysis

This section is devoted to muon performance studies carried out in the context of a number of physics analyses: Standard Model and SUSY Higgs, inclusive SUSY, heavy gauge bosons and left-right symmetric models. As a result, selection criteria are generally not exactly the same as those used to obtain the results shown in the previous sections.

10.1 $\mathbf{H} \rightarrow \mu^+\mu^-\mu^+\mu^-$

The $H \rightarrow ZZ^* \rightarrow 4\mu$ decay mode is one of the most promising channels for the discovery of the Standard Model Higgs boson at the LHC and, as a result, it has served as a benchmark for the optimization of the ATLAS detector performance. In the following, the performance of the muon reconstruction algorithms in reconstructing this resonance is studied for a set of different Higgs mass scenarios, covering the mass range from 120 to 300 GeV. The analysis is performed using the official AOD samples, see table 16.

Table 16: Standard Model Higgs samples used to evaluate the muon performance.

Dataset name	# events
trig1_misal1_mc12.006300.PythiaH120zz4l.recon.AOD.v12000604	49700
trig1_misal1_mc12.006301.PythiaH150zz4l.recon.AOD.v12000604	39250
trig1_misal1_csc11.005300.PythiaH130zz4l.recon.AOD.v12000601	9750
trig1_misal1_mc12.006302.PythiaH160zz4l.recon.AOD.v12000604	49709
trig1_misal1_mc12.006303.PythiaH165zz4l.recon.AOD.v12000604	49950
trig1_misal1_mc12.006304.PythiaH180zz4l.recon.AOD.v12000604	19750
trig1_misal1_mc12.006305.PythiaH200zz4l.recon.AOD.v12000604	48500
trig1_misal1_mc12.006382.PythiaH300zz4l.recon.AOD.v12000604	9900

The present analysis, usually referred to as the $H \rightarrow 4\mu$ "standard analysis", serves as a baseline for the $H \rightarrow ZZ^* \rightarrow 4\mu$ searches. We require candidate events to contain at least four combined muons, with $|\eta| < 2.5$ and $p_T > 7$ GeV/c. Two of those muons must also have $p_T > 20$ GeV/c. Muons are then paired to form the two Z boson candidates from the Higgs decay. Only events satisfying the dimuon criteria listed in table 17 are retained for further analysis. Finally, the calorimeter and track isolation energies of the muons, in a cone of $\Delta R = 0.2$, are required to be less than 6 and 5 GeV, respectively, and the muon impact parameter significance (r_0/σ_{r_0}) is required to be < 6.

Table 17: Mass window of the leading dimuon pair and the cut on the second dimuon pair, for each Higgs mass scenario.

Higgs Mass (GeV)	Z_1 window	Z_2 cut
120	$m_Z \pm 20$	$> 15GeV$
130	$m_Z \pm 15$	$> 20GeV$
150	$m_Z \pm 15$	$> 30GeV$
160	$m_Z \pm 12$	$> 30GeV$
165	$m_Z \pm 12$	$> 35GeV$
180	$m_Z \pm 12$	$> 40GeV$
200	$m_Z \pm 12$	$> 60GeV$
120	$m_Z \pm 12$	$m_Z \pm 15GeV$

Figure 21 shows the transverse momentum resolution for Staco and Muid combined muons without any cuts, respectively. Figure 22 shows the relative resolution on the Higgs mass for the different mass

scenarios, with and without the application of the Z mass constraint. The latter technique aims to improve the Higgs mass resolution by constraining the mass of the dimuon forming the Z boson, accounting also for the non-negligible natural width of the Z boson. The resolution has been obtained using iterative $\pm 2\sigma$ Gaussian fits. Finally, Fig. 23 shows the reconstructed peak of the Higgs boson.

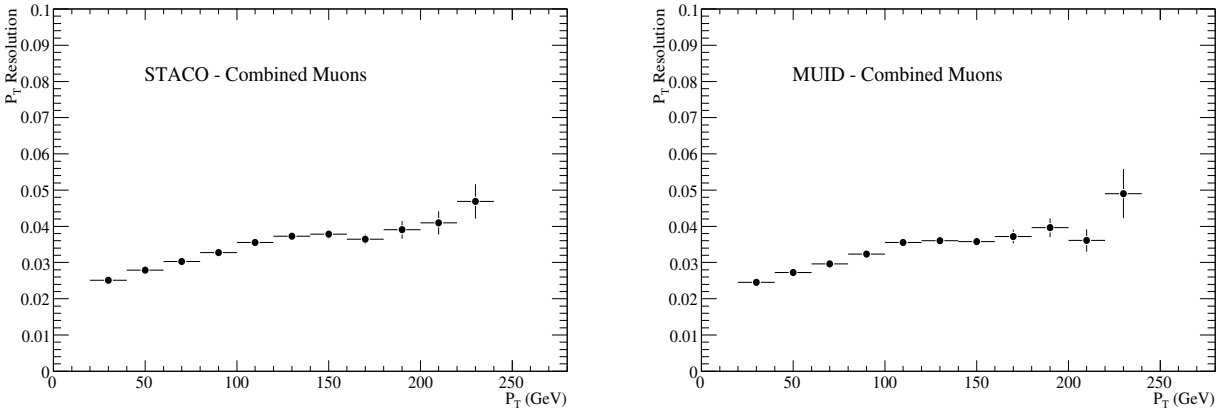

Figure 21: Relative muon p_T resolution as a function of p_T for Staco (left) and Muid (right).

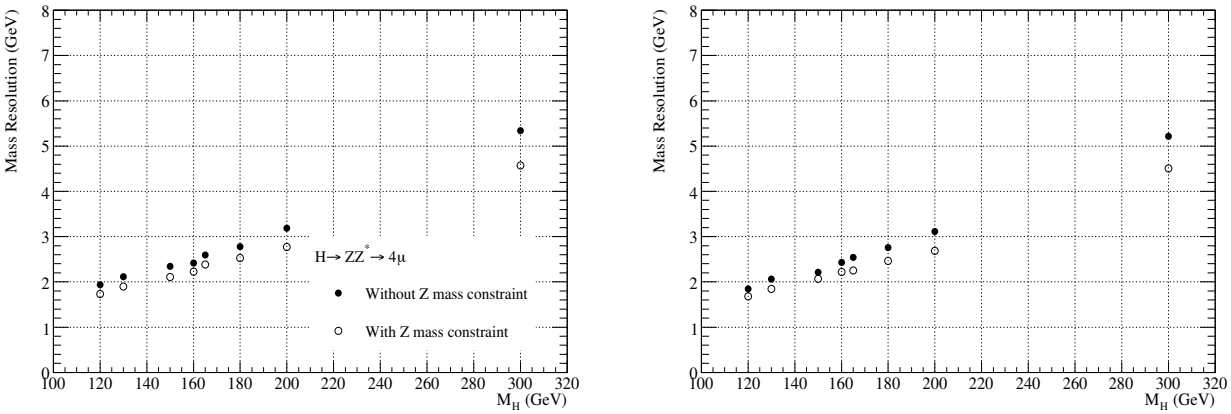

Figure 22: Relative resolution in the Higgs mass reconstruction, after all the analysis cuts, as a function of the Higgs mass with and without the Z mass constraint for Staco (left) and Muid (right).

Tables 18 and 19 summarize the performance of the muon reconstruction algorithms in terms of non-Gaussian tails. The quoted numbers are based on Gaussian fits to the whole distribution of the difference between the true and reconstructed masses. The efficiency of the analysis cuts on the Higgs signal is also presented.

Muon performance was also studied for Higgs decays with a single Higgs mass value of 130 GeV in order to evaluate the impact of cavern background. For this study, the HiggsToFourLeptonsEV package in the EventView analysis framework was used [19,20] and the following merged muon algorithms were considered: Muid+MuGirl and Staco+MuTag. Muons were required to have $|\eta| < 2.5$ and with $p_T > 5$ GeV/c.

In order to reduce $Zb\bar{b}$ and $t\bar{t}$ backgrounds further muon isolation criteria, since muons from Higgs decays are usually isolated and are expected to be associated to the interaction point, IP. Calorimeter

Table 18: Performance of Higgs mass reconstruction for various Higgs masses between 120 and 180 GeV.

	Staco		Muid	
Higgs mass = 120 GeV	w/o Z fit	w/ Z fit	w/o Z fit	w/ Z fit
$\mu(MeV)$	136 ± 18	-15 ± 16	417 ± 19	216 ± 17
$\sigma(GeV)$	2.19 ± 0.02	1.98 ± 0.02	2.09 ± 0.02	1.89 ± 0.02
Efficiency (%)	33.2 ± 0.2		28.6 ± 0.2	
Fraction in 2σ	91.9 ± 0.2	90.0 ± 0.2	91.4 ± 0.2	90.2 ± 0.3
Fraction in 5σ	99.1 ± 0.1	98.6 ± 0.1	98.8 ± 0.1	98.6 ± 0.1
Higgs mass = 130 GeV				
$\mu(MeV)$	185 ± 20	52 ± 18	463 ± 21	285 ± 19
$\sigma(GeV)$	2.29 ± 0.02	2.09 ± 0.02	2.23 ± 0.02	2.01 ± 0.02
Efficiency (%)	37.6 ± 0.2		33.1 ± 0.2	
Fraction in 2σ	90.8 ± 0.2	91.0 ± 0.2	90.9 ± 0.3	91.0 ± 0.3
Fraction in 5σ	99.0 ± 0.1	98.8 ± 0.1	99.1 ± 0.1	98.7 ± 0.1
Higgs mass = 150 GeV				
$\mu(MeV)$	304 ± 41	176 ± 37	603 ± 39	525 ± 36
$\sigma(GeV)$	2.52 ± 0.04	2.31 ± 0.03	2.37 ± 0.04	2.20 ± 0.03
Efficiency (%)	44.5 ± 0.5		40.9 ± 0.5	
Fraction in 2σ	90.8 ± 0.4	90.2 ± 0.5	90.9 ± 0.5	90.4 ± 0.5
Fraction in 5σ	99.1 ± 0.1	98.8 ± 0.2	99.2 ± 0.1	99.2 ± 0.1
Higgs mass = 160 GeV				
$\mu(MeV)$	345 ± 19	263 ± 17	665 ± 19	554 ± 17
$\sigma(GeV)$	2.78 ± 0.02	2.56 ± 0.02	2.67 ± 0.02	2.45 ± 0.02
Efficiency (%)	49.7 ± 0.2		46.0 ± 0.2	
Fraction in 2σ	91.0 ± 0.2	90.2 ± 0.189	91.4 ± 0.2	89.9 ± 0.2
Fraction in 5σ	99.1 ± 0.0588	98.9 ± 0.0649	99 ± 0.1	98.7 ± 0.1
Higgs mass = 165 GeV				
$\mu(MeV)$	409 ± 20	313 ± 18	765 ± 20	617 ± 19
$\sigma(GeV)$	2.89 ± 0.02	2.70 ± 0.02	2.79 ± 0.02	2.59 ± 0.02
Efficiency (%)	48.3 ± 0.2		44.3 ± 0.2	
Fraction in 2σ	91.2 ± 0.2	90.9 ± 0.2	90.2 ± 0.2	90.2 ± 0.2
Fraction in 5σ	98.9 ± 0.1	98.7 ± 0.1	98.9 ± 0.1	98.6 ± 0.1
Higgs mass = 180 GeV				
$\mu(GeV)$	492 ± 31	390 ± 30	925 ± 33	794 ± 31
$\sigma(GeV)$	3.08 ± 0.03	2.90 ± 0.03	2.99 ± 0.03	2.82 ± 0.03
Efficiency (%)	55.3 ± 0.4		50.2 ± 0.4	
Fraction in 2σ	89.9 ± 0.3	89.6 ± 0.3	89 ± 0.3	88.3 ± 0.3
Fraction in 5σ	98.0 ± 0.1	97.9 ± 0.1	98 ± 0.1	97.7 ± 0.2

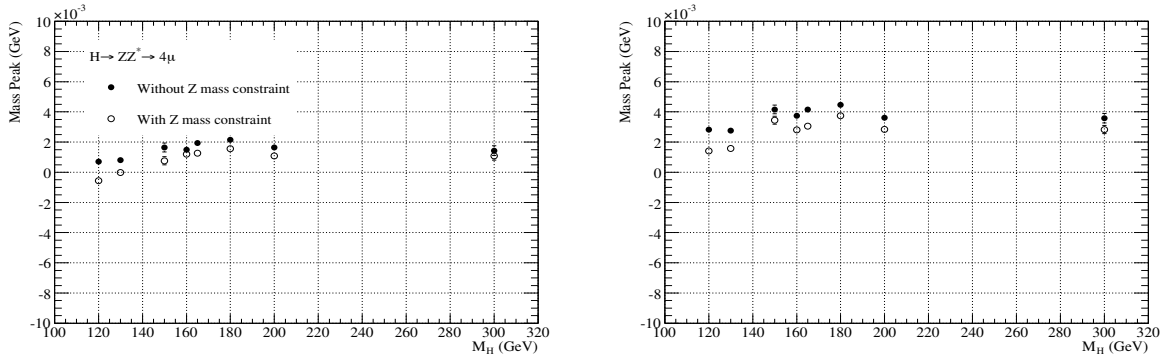

Figure 23: Generated minus reconstructed mass of the Higgs boson, after all the analysis cuts, as a function of the Higgs mass with and without the Z mass constraint for Staco (left) and Muid (right).

Table 19: Performance of Higgs mass reconstruction for Higgs masses of 200 and 300 GeV.

	Staco		Muid	
Higgs mass = 200 GeV	w/o Z fit	w/ Z fit	w/o Z fit	w/ Z fit
$\mu(MeV)$	459 ± 23	349 ± 21	895 ± 23	710 ± 21
$\sigma(GeV)$	3.53 ± 0.02	3.14 ± 0.02	3.37 ± 0.02	2.95 ± 0.02
Efficiency (%)	54.3 ± 0.2		50.6 ± 0.2	
Fraction in 2σ	90.9 ± 0.2	89.8 ± 0.2	90.3 ± 0.2	89.7 ± 0.2
Fraction in 5σ	98.3 ± 0.1	97.9 ± 0.1	98.1 ± 0.1	97.6 ± 0.1
Higgs mass = 300 GeV				
$\mu(GeV)$	536 ± 89	399 ± 79	1176 ± 85	918 ± 73
$\sigma(GeV)$	5.78 ± 0.08	5.14 ± 0.08	5.70 ± 0.07	4.85 ± 0.07
Efficiency (%)	46.1 ± 0.5		47.9 ± 0.5	
Fraction in 2σ	93.7 ± 0.4	92.1 ± 0.4	93.6 ± 0.4	91.5 ± 0.4
Fraction in 5σ	99.7 ± 0.1	99.6 ± 0.1	99.7 ± 0.1	99.7 ± 0.1

isolation cuts were used as well as track isolation and impact parameter cuts. For the calorimeter isolation the sum of the transverse energy in the calorimeter in a cone of $\Delta R < 0.2$ is calculated and the muon is rejected if this sum is over 5 GeV. For track isolation the sum of the transverse momentum of all the inner detector tracks within a cone of $\Delta R < 0.2$ around the muon is obtained and the muon is used only if the sum is below 5 GeV. Also a muon impact parameter significance cut of less than 5 is used to isolate the muons.

Figure 24 shows the reconstructed Higgs mass distribution for Muid, Staco, Muid+MuGirl, and Staco+MuTag without isolation and impact parameter requirements. Staco and Staco+MuTag have higher efficiencies than Muid or Muid+MuGirl but worse resolutions. Muid+MuGirl has worse resolution than Muid and Staco+MuTag same resolution with Staco.

Figure 25 shows the sane distribution but with the inclusion of isolation and impact parameter cuts. This time the Muid+MuGirl and Staco+MuTag show same resolutions with Muid and Staco, respectively.

The effect of the pileup on the muon fakes and muon reconstruction efficiencies was evaluated with the SF05 H(130) sample, were minimum bias events and cavern background events of safety factor 5 were added. The muon efficiency is defined as the number of reconstructed muons which match a true muon in $\Delta R < 0.02$ cone, divided by the number of true muons. The muon fake rate is defined as the number of reconstructed muons which did not match a true muon in a cone of $\Delta R < 0.02$ divided by the number of true muons.

The muon fake rate as a function of p_T and η without applying any additional kinematic or isolation cuts is shown in Figs. 26 and 27 for the four different combined muon reconstruction algorithms. A higher fake rate is observed in the case of Muid and Muid+MuGirl than Staco and Staco+MuTag, respectively. Furthermore, Muid and Muid+MuGirl have lower efficiencies as a function of p_T and η than Staco and Staco+MuTag, see Figs. 28 and 29. However, after applying isolation cuts in a $\Delta R < 0.45$ cone, calorimeter isolation energy and track isolation energy both less than 5 GeV and impact parameter significance cut less than 5, the muon fake rate is dramatically reduced for all combined reconstruction algorithms as shown in Figs. 30 and 31.

Table 20: Datasets used in this analysis.

Name	Dataset name	# events
H(130)	trig1_misal1_csc11.005300.PythiaH130zz4l.v12000601	∼40K
SF05 H(130)	trig1_pile1sf05_misal1_csc11.005300.PythiaH130zz4l.recon.v12000605	∼40K

10.2 SUSY $H/A \rightarrow \mu^+\mu^-$

The $H/A \rightarrow \mu^+\mu^-$ decay channel can provide a uniquely clean experimental signature for the discovery of one of the MSSM Higgs bosons. The H/A gets fully reconstructed as a dimuon resonance peaking at the relevant mass. In order to study the muon performance for this physics channel, five different masses of H/A have been used (see table 21) spanning the region from 110 GeV to 400 GeV. The p_T of the decay muons varies from a few GeV to several hundred GeV. Figure 32 shows the reconstruction efficiency (top) as a function of p_T for Staco+MuTag (left) and Muid+MuGirl (right). The p_T resolution of a function of p_T is shown on the bottom row of the same figure. The corresponding plots for the sample of m_A=200 GeV with pile-up and cavern background with safety factor 5 are superimposed. It is obvious from the plots that the combined muon efficiency of Muid+MuGirl is heavily deteriorated for this sample, while the combined muon efficiency of Staco+MuTag and the momentum resolution of both algorithms are marginally affected.

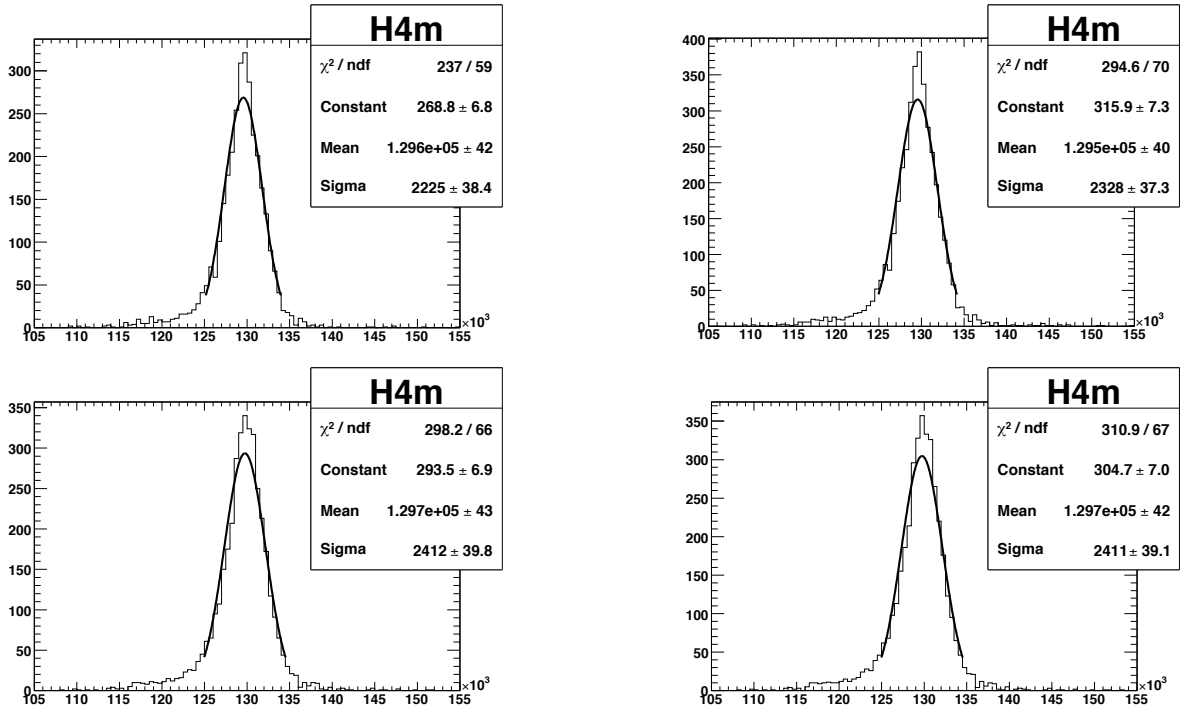

Figure 24: Higgs 4 muon mass distribution for Muid (left, top) and Muid+MuGirl (right, top), Staco (left, bottom) and Staco+MuTag (right, bottom) without cuts, in the H(130) sample.

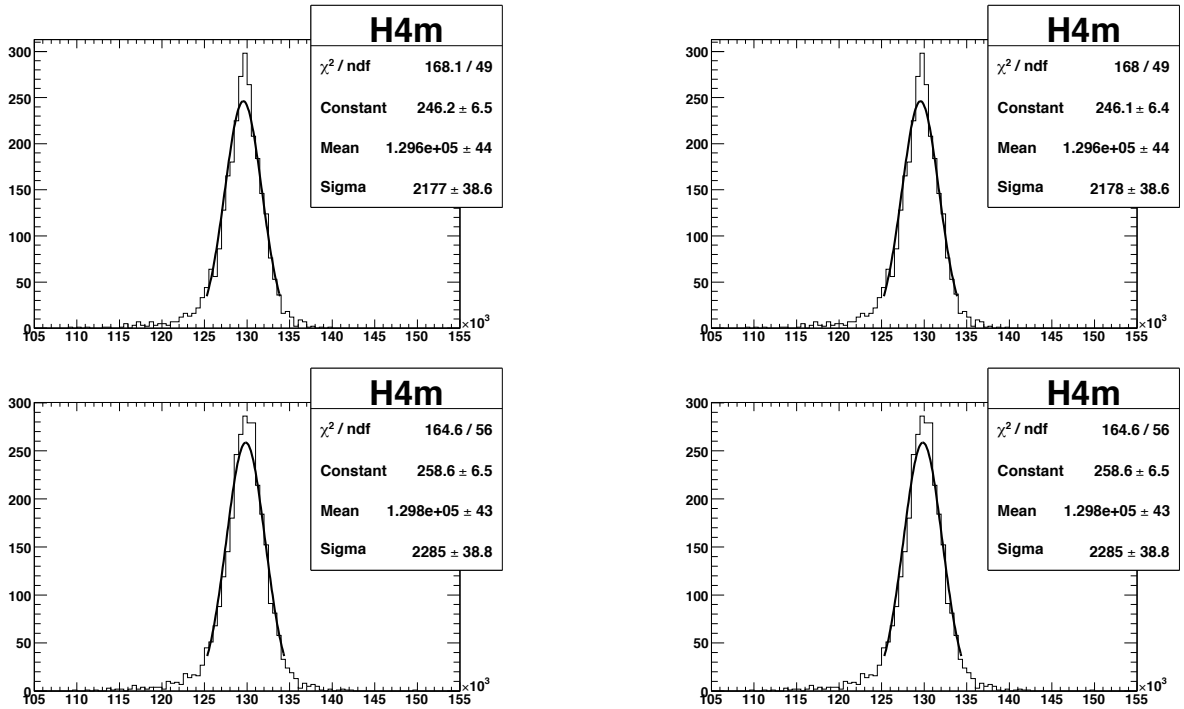

Figure 25: Higgs 4 muon mass distribution for Muid (left, top) and Muid+MuGirl (right, top), Staco (left, bottom) and Staco+MuTag (right, bottom) with isolation and impact parameter cuts, in the H(130) sample.

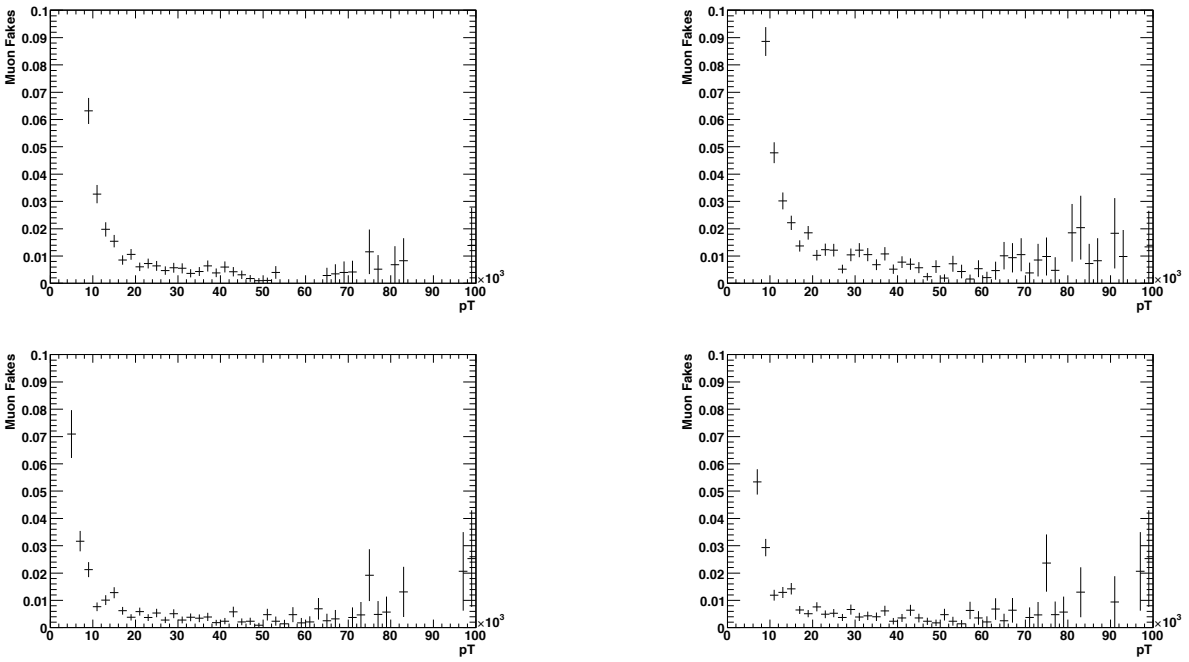

Figure 26: Muon fakes as a function of p_T for Muid (left, top) and Muid+MuGirl (right, top), Staco (left, bottom) and Staco+MuTag (right, bottom) without cuts in the SF05 H(130) sample.

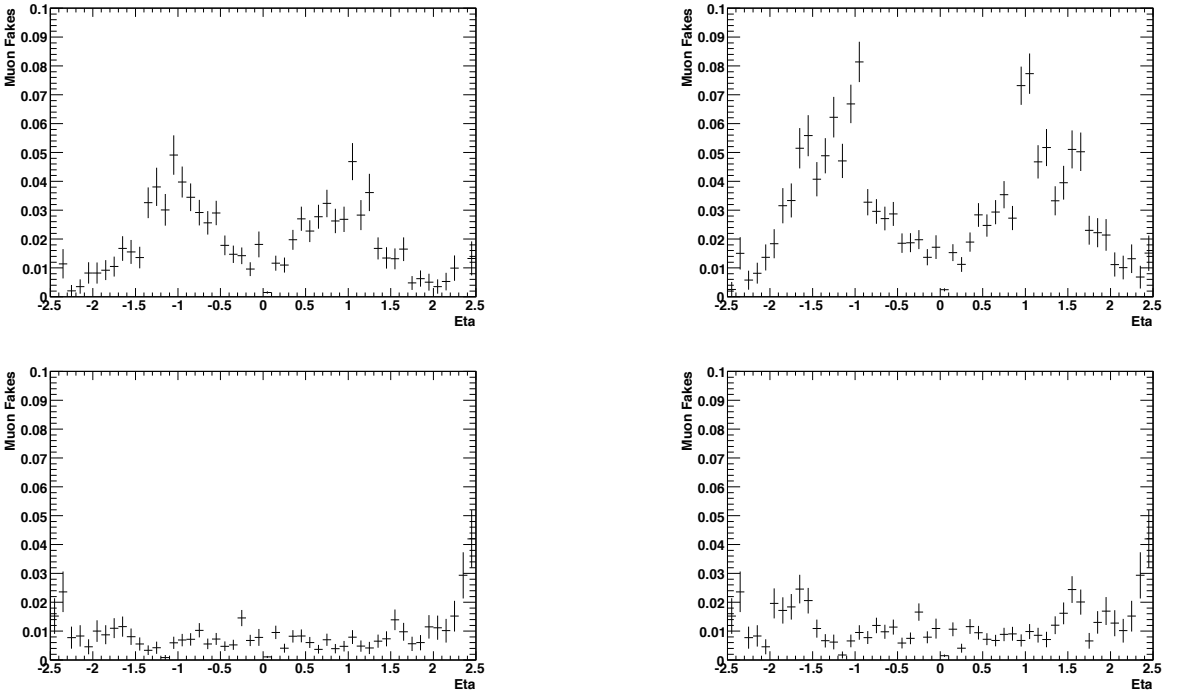

Figure 27: Muon fakes as a function of η for Muid (left, top) and Muid+MuGirl (right, top), Staco (left, bottom) and Staco+MuTag (right, bottom) without cuts in the SF05 H(130) sample.

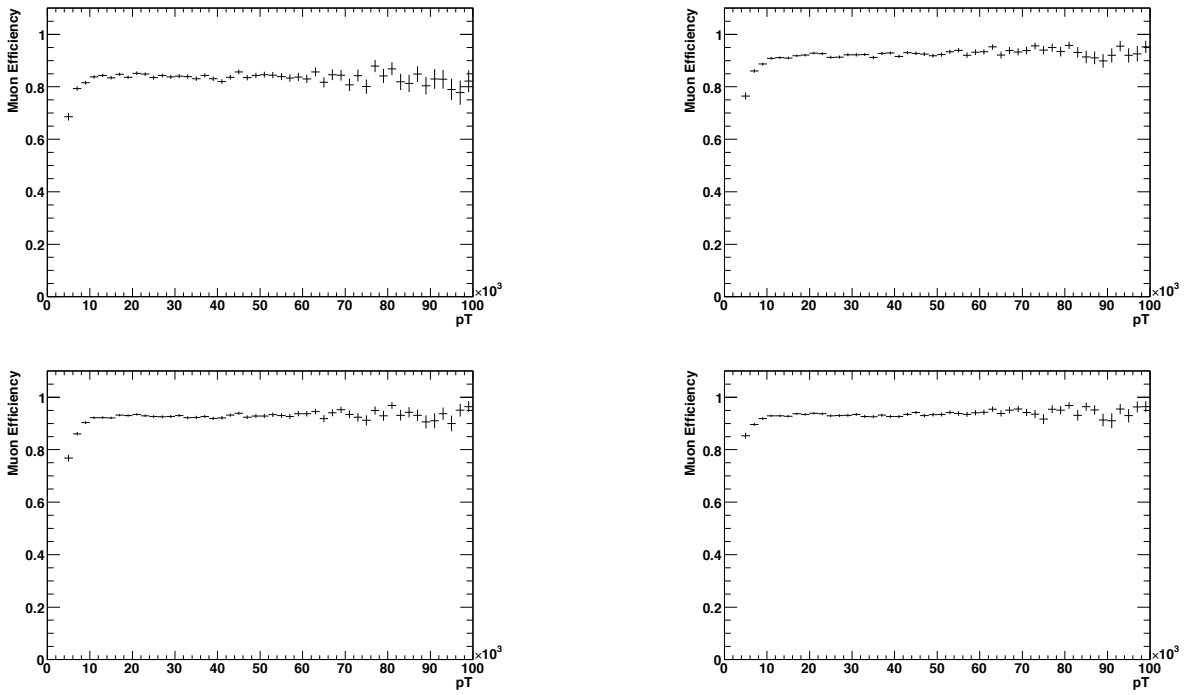

Figure 28: Muon efficiency as a function of p_T for Muid (left, top) and Muid+MuGirl (right, top), Staco (left, bottom) and Staco+MuTag (right, bottom) without cuts in the SF05 H(130) sample.

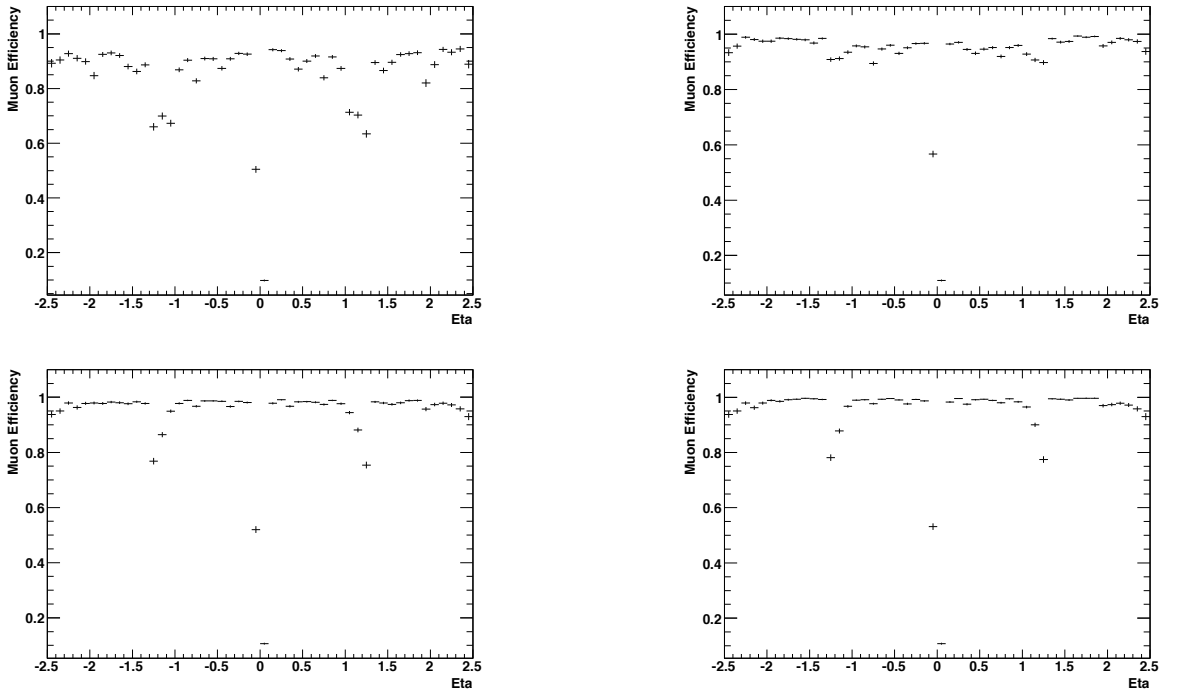

Figure 29: Muon efficiency as a function of η for Muid (left, top) and Muid+MuGirl (right, top), Staco (left, bottom) and Staco+MuTag (right, bottom) without cuts in the SF05 H(130) sample.

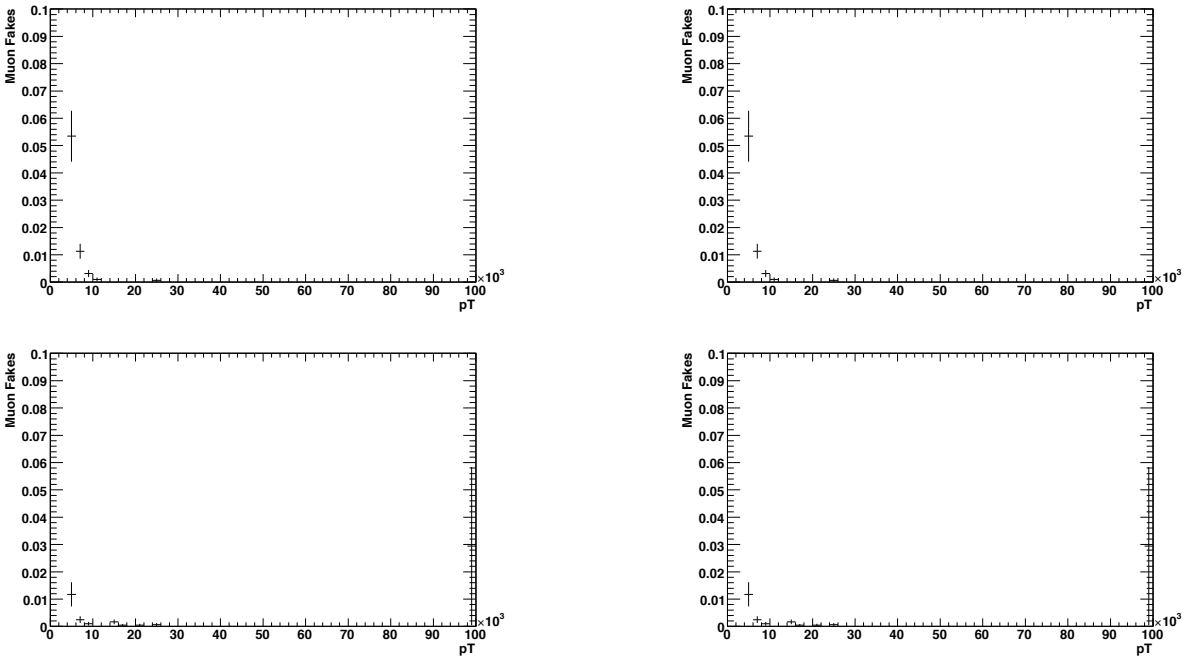

Figure 30: Muon fakes as a function of p_T for Muid (left, top) and Muid+MuGirl (right, top), Staco (left, bottom) and Staco+MuTag (right, bottom) after isolation and impact parameter cuts in the SF05 H(130) sample.

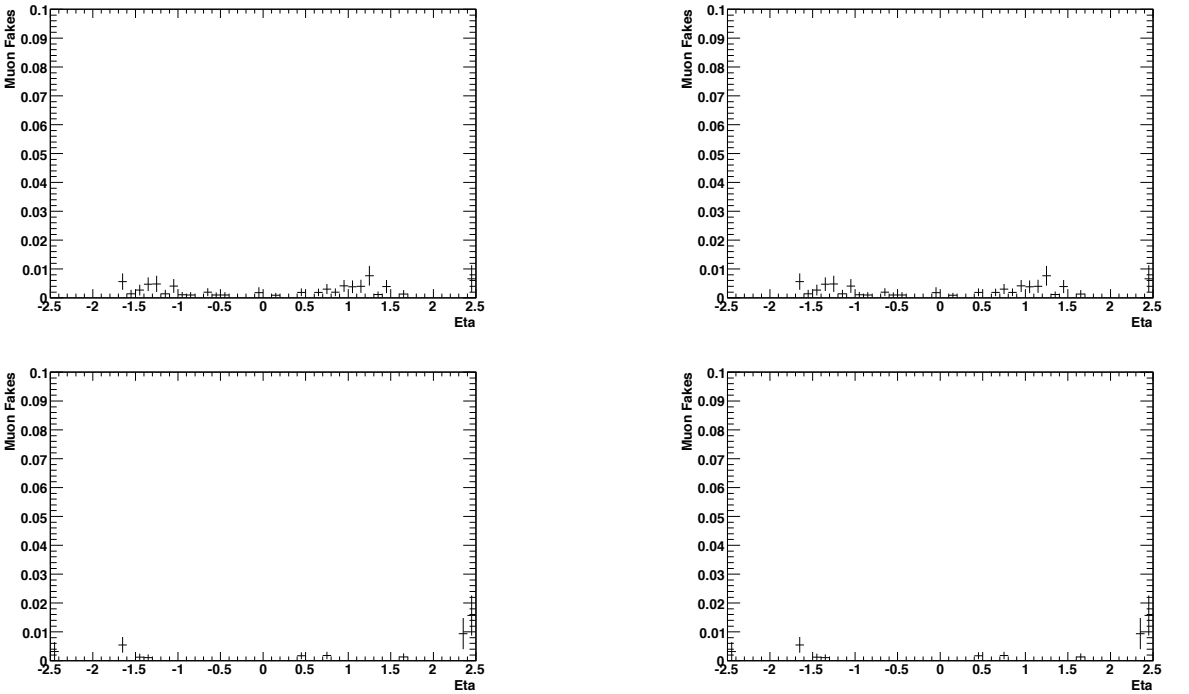

Figure 31: Muon fakes as a function of η for Muid (left, top) and Muid+MuGirl (right, top), Staco (left, bottom) and Staco+MuTag (right, bottom) after isolation and impact parameter cuts in the SF05 H(130) sample.

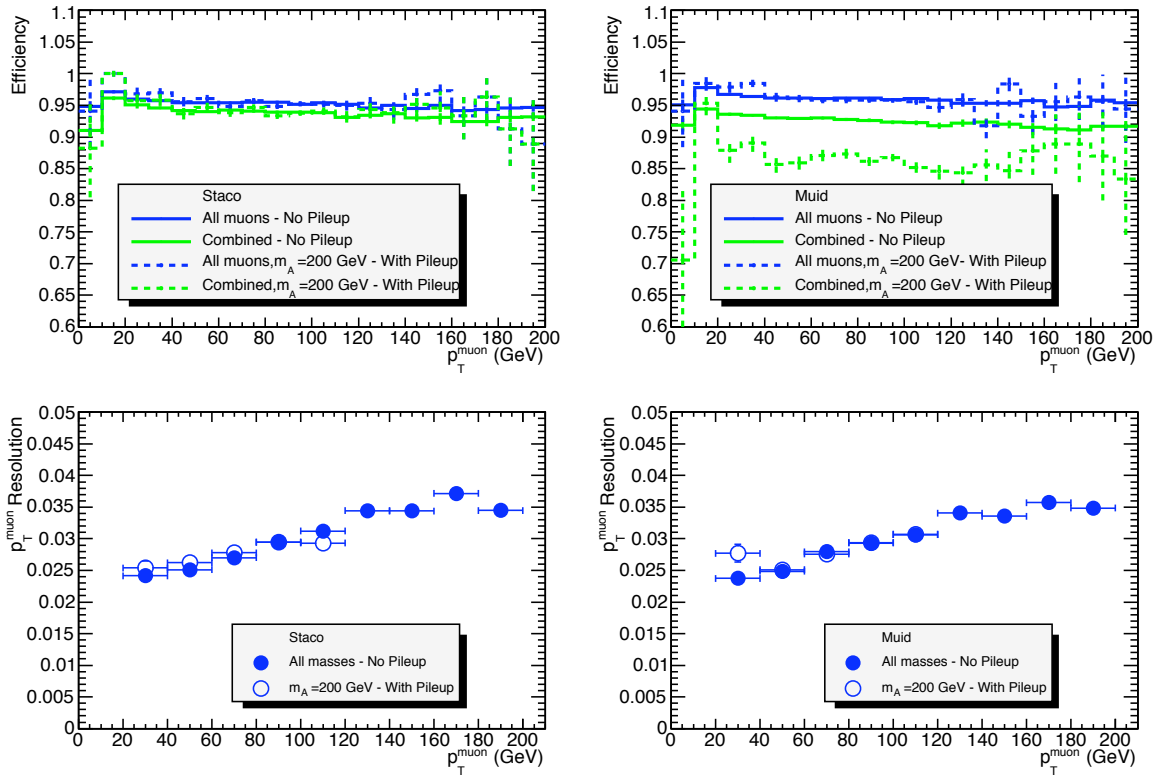

Figure 32: Muon reconstruction efficiency (top) in H/A decays for all and combined muons and Muon p_T resolution (bottom) as a function of p_T. Events with pile-up and cavern background for m_A=200 GeV are superimposed.

Table 21: Data samples used in this section.

File type	Sample ID	No of events
bbA, m_A=110 GeV, $\tan\beta = 45$	trig1_misal1_mc12005350	5000
bbA, m_A=110 GeV, $\tan\beta = 30$	trig1_misal1_mc12006337	3200
bbA, m_A=110 GeV, $\tan\beta = 15$	trig1_misal1_mc12006338	46400
bbA, m_A=150 GeV, $\tan\beta = 30$	trig1_misal1_mc12006341	5000
bbA, m_A=200 GeV, $\tan\beta = 30$	trig1_misal1_mc12005351	8850
with pileup and cavern blg	trig1_pile1sf05misal1_mc12005351	7750
A, m_A=200 GeV, $\tan\beta = 30$	trig1_misal1_mc12006335	4250
bbA, m_A=200 GeV, $\tan\beta = 45$	trig1_misal1_mc12006339	3250
bbA, m_A=300 GeV, $\tan\beta = 30$	trig1_misal1_mc12006342	3250
bbA, m_A=400 GeV, $\tan\beta = 30$	trig1_misal1_mc12006343	5000

In order to evaluate the performance of the two algorithms on the mass reconstruction, the standard preselection of the analysis is used (further cuts irrelevant to muon reconstruction are applied in the actual H/A analysis). A lower cut of 20 GeV has been imposed to the p_T of each muon. Only opposite sign dimuon pairs are further selected. In addition, there is a cut on the isolation of each muon in order to reject the main source of background which in the associated production case, TbH/A, is the $t\bar{t}$ one. The isolation cut imposed on each muon is to have the transverse energy deposited in the calorimeters in a cone of radius $\Delta R < 0.4$ divided by the p_T of the corresponding muon less than 0.2. If there are more than two muons passing the above criteria, the invariant mass is formed by the two most energetic ones. The mass residuals $m_{true} - m_{reconstructed}$ for the 5 different generated masses are shown in figure 33. In these plots a Gaussian fit in a region of $\pm 2\sigma$ around the peak has been performed. The results of the fits are shown on the plots. In addition, a more detailed study of the two algorithms behavior is summarized in table 22. In this case the Gaussian fits were performed in all the region [-100, +100] GeV. The corresponding mean values and standard deviations, the efficiency of obtaining a candidate with the above mentioned criteria and the fraction of the selected events in 2 σ and 5 σ windows are shown. It can be seen that using all muons in each collection, Muid+MuGirl has a higher initial efficiency, which is partially compensated by the higher Staco+MuTag fraction of events in a realistic mass window.

10.3 Inclusive SUSY

Since many of the SUSY analyses focus on events with one or more high-energy leptons [21], the knowledge of the performance on these leptons, i.e. efficiencies and fake rates, is a crucial point. Few points from different regions of mSUGRA parameter space were selected for full simulation studies. SU3 point which is covering the bulk region of mSUGRA parameter space has been chosen as benchmark point for SUSY full simulation studies. Also SU1 point in the stau-coannihilation region and SU4 point in the low-mass region were analyzed. SUSY signal was generated with Herwig-Jimmy [14, 22–25], while mSUGRA input files were generated with isasugra [26]. Leptonic top quark decays constitute a major background for analyses with leptons in the final state. We use the T1 sample, which contains at least one top quark decaying leptonically, generated with the MC@NLO generator [10, 11]. Dataset names and corresponding cross sections are specified in table 23. Pile-up and cavern background simulation were not included in the signal and background samples.

Muon identification criteria were chosen in such a way as to get the best possible efficiency and minimal probability of misidentification in a given SUSY environment. Staco muons were required to

Table 22: Properties of reconstructed dimuon masses from H/A decays. Gaussian mean μ and width σ, efficiency with preselection cuts (as described in the text) and fraction of events in a window of approximately 2 and 5 σ from the peak.

H/A mass = 110 GeV	Staco+MuTag	Muid+MuGirl
μ (MeV)	-135 $\pm$ 12	127 $\pm$ 11
σ (GeV)	2.35 $\pm$ 0.1	2.28 $\pm$ 0.1
Efficiency %	76.0 $\pm$ 0.2	78.2 $\pm$ 0.2
Fraction with $\lvert M-\mu\rvert < 12.5$ GeV (%)	98.6 $\pm$ 0.1	97.8 $\pm$ 0.1
Fraction with $\lvert M-\mu\rvert < 5$ GeV (%)	92.7 $\pm$ 0.1	92.6 $\pm$ 0.1
H/A mass = 150 GeV	Staco+MuTag	Muid+MuGirl
μ (MeV)	-210 $\pm$ 60	+103 $\pm$ 50
σ (GeV)	3.40 $\pm$ 0.05	3.25 $\pm$ 0.04
Efficiency %	79.7 $\pm$ 0.5	83.1 $\pm$ 0.5
Fraction with $\lvert M-\mu\rvert < 17.5$ GeV (%)	98.1 $\pm$ 0.2	97.1 $\pm$ 0.2
Fraction with $\lvert M-\mu\rvert < 7$ GeV (%)	91.1 $\pm$ 0.4	91.1 $\pm$ 0.4
H/A mass = 200 GeV	Staco+MuTag	Muid+MuGirl
μ (MeV)	-477 $\pm$ 44	+279 $\pm$ 43
σ (GeV)	4.91 $\pm$ 0.04	4.81 $\pm$ 0.04
Efficiency %	80.3 $\pm$ 0.3	83.5 $\pm$ 0.3
Fraction with $\lvert M-\mu\rvert < 25$ GeV (%)	97.8 $\pm$ 0.2	96.9 $\pm$ 0.2
Fraction with $\lvert M-\mu\rvert < 10$ GeV (%)	90.7 $\pm$ 0.3	90.0 $\pm$ 0.3
H/A mass = 300 GeV	Staco+MuTag	Muid+MuGirl
μ (MeV)	-400 $\pm$ 170	-80 $\pm$ 170
σ (GeV)	8.10 $\pm$ 0.16	8.10 $\pm$ 0.16
Efficiency %	79.5 $\pm$ 0.8	83.2 $\pm$ 0.8
Fraction with $\lvert M-\mu\rvert < 40$ GeV (%)	97.7 $\pm$ 0.4	95.7 $\pm$ 0.4
Fraction with $\lvert M-\mu\rvert < 16$ GeV (%)	88.9 $\pm$ 0.6	86.8 $\pm$ 0.6
H/A mass = 400 GeV	Staco+MuTag	Muid+MuGirl
μ (MeV)	-1310 $\pm$ 200	-620 $\pm$ 200
σ (GeV)	11.7 $\pm$ 0.2	11.6 $\pm$ 0.2
Efficiency %	79.7 $\pm$ 0.5	83.3 $\pm$ 0.5
Fraction with $\lvert M-\mu\rvert < 55$ GeV (%)	96.9 $\pm$ 0.3	95.1 $\pm$ 0.3
Fraction with $\lvert M-\mu\rvert < 22$ GeV (%)	86.6 $\pm$ 0.5	84.6 $\pm$ 0.5

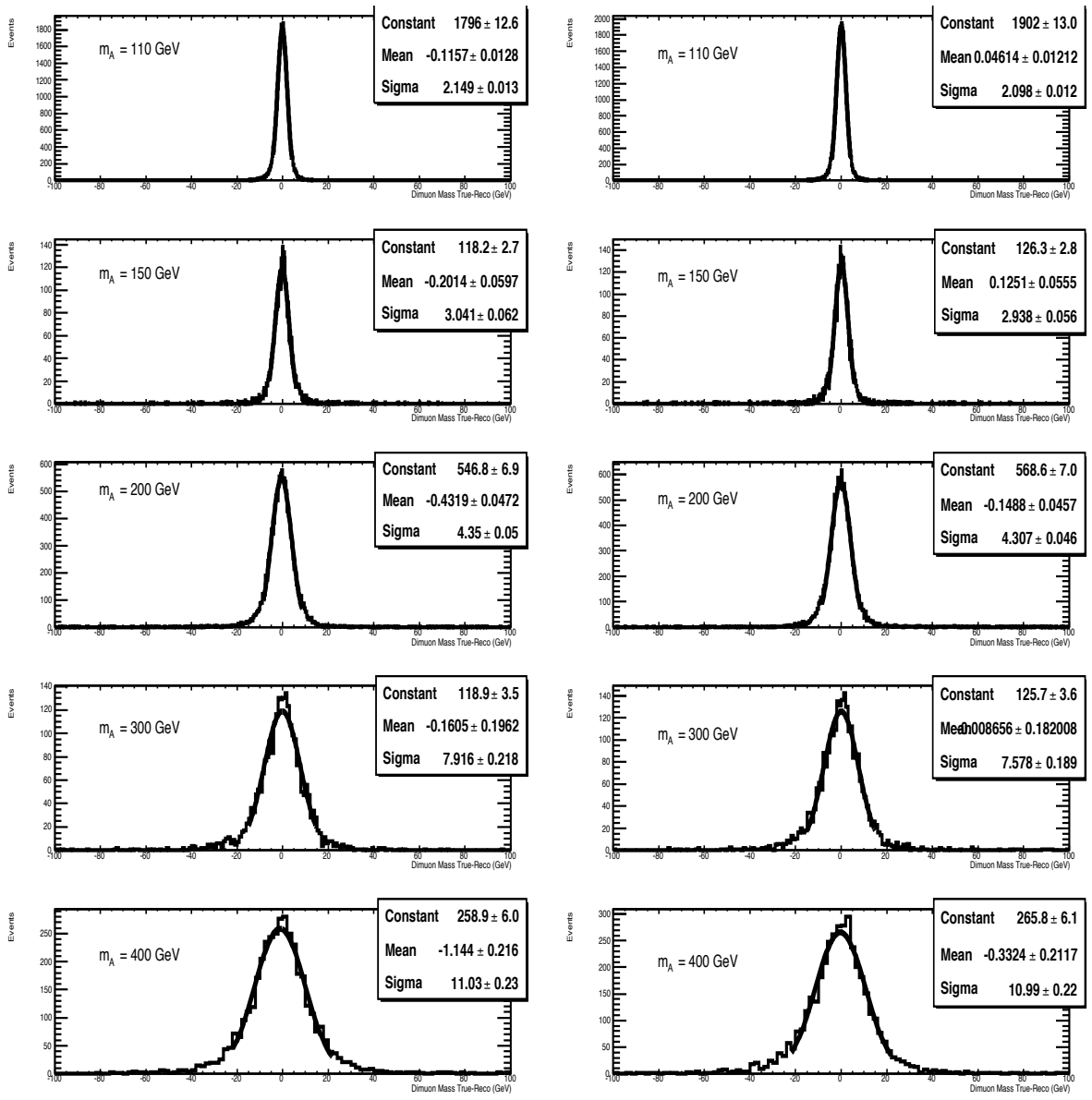

Figure 33: Dimuon mass resolution in H/A decays for muons passing the preselection defined in the text. The left (right) column corresponds to Staco+MuTag (Muid+MuGirl). From top to bottom m_A = 110, 150, 200, 300 and 400 GeV, respectively.

Table 23: Datasets used for SUSY signal and background processes.

Sample	Data Set	σ (pb)
SU1	trig1_misal1_csc11.005401.SU1_jimmy_susy.recon.AOD.v12000601	7.43
SU3	trig1_misal1_csc11.005403.SU3_jimmy_susy.recon.AOD.v12000601	18.59
SU4	trig1_misal1_mc12.006400.SU4_jimmy_susy.recon.AOD.v12000601	262
T1	trig1_misal1_mc12.005200.T1_McAtNlo_Jimmy.recon.AOD.v12000604	461

be reconstructed with Muonboy, while those reconstructed with MuTag were discarded. Muid muons produced with Moore/Muid were used and muons from MuGirl were neglected. Both Staco and Muid muons were forced to be combined muons and if more than one Inner Detector track matched one track from the Muon Spectrometer, only the one with the best match was kept. Muon identification cuts: p_T, η, calorimeter isolation in a $\Delta R < 0.2$ cone E_T^{isol}, match and fit χ^2/ndf, applied to truth and reconstructed muons are listed in table 24 together with p_T and η cuts applied on truth jets.

Table 24: Identification cuts applied on truth and reconstructed muons and truth jets.

	Truth μ ε	Reco. μ Staco ε	Reco. μ Muid ε	Truth μ Fake rates	Reco. μ Staco Fake rates	Reco. μ Muid Fake rates	Truth jet
$p_T(GeV)$ min	20	15	15	15	20	20	20
$\|\eta\|$ max	2.5	2.5	2.5	2.5	2.5	2.5	2.5
$E_T^{isol}(GeV)$ max	10	10	10		10	10	
match χ^2/ndf max		20	4		20	4	
fit χ^2/ndf max			5			5	

If truth electrons with $p_T > 20$ GeV, $|\eta| < 2.5$ and calorimeter isolation in a $\Delta R < 0.2$ less than 10 GeV, were found to be at a distance $\Delta R < 0.2$ from a truth jet with $p_T > 20$ GeV, $|\eta| < 2.5$, then this truth jet was excluded from studies. Truth and reconstructed muons and truth jets passing the mentioned selection criteria were used for computation of efficiencies and fake rates.

Muons in the event can originate from several sources. They are produced in the decays of "heavy" particles, like SUSY particles, W and Z bosons, τ leptons, or they can come from light and heavy flavor decays. There is the possibility that muons are radiated by other muons in the Bremsstrahlung process (so called "G4 muons"). According to the origin of the muon, the following selections of truth muons were considered for efficiencies and fake rate analysis:

- Muons from decays of "heavy" particles: SUSY, W, Z and τ (Def1);
- Muons from decays of all particles (SUSY, W, Z, τ, light and heavy flavors), apart from G4 muons (Def2);
- Muons from decays of all particles including G4 muons (Def3).

One needs to know how many of the generated muons are identified in the detector. The efficiency was defined as the ratio between the number of truth muons matched with a reconstructed muon within a distance $\Delta R < 0.02$ and by the number of truth muons. Truth muons described by the first two definitions (Def1 and Def2) were used. Efficiencies are reported in table 25. The efficiencies as a function of η and

of p_T for Staco muons and Muid muons from SU3 and T1 samples, where truth muons are selected according to the Def2 selection, are shown in Fig. 34. Table 25 summarizes the efficiencies and indicates similar performance for the different SUSY samples.

Table 25: Staco and Muid efficiencies for SU1, SU3, SU4 and T1 samples.

	STACO	MUID
SU1, Def1 of truth μ	90.4(2)%	85.5(2)
SU1, Def2 of truth μ	90.4(2)%	85.5(2)
SU3, Def1 of truth μ	90.3(2)%	85.3(2)%
SU3, Def2 of truth μ	90.3(2)%	85.3(2)%
SU4, Def1 of truth μ	90.7(2)%	85.7(2)%
SU4, Def2 of truth μ	90.7(2)%	85.6(2)%
T1, Def1 of truth μ	91.46(7)%	86.5(1)%
T1, Def2 of truth μ	91.45(7)%	86.5(1)%

The muon fake rate was defined as the number of reconstructed muons without matching truth muon with $\Delta R < 0.02$ divided by the number of truth jets. Truth muons from all three definitions (Def1, Def2, Def3) were analyzed. Fake rates are reported in table 26. For definitions Def2 and Def3, the fake rates are statistically compatible in different SUSY and T1 samples and are very low, of order 10^{-5}. With respect to muons described by Def1, fake rates are one or two orders of magnitude larger because these fake rates include contributions from reconstructed muons inside jets. T1 and SU4 samples have larger fake rates than SU1 and SU3 samples, because of the larger number of b-jets in SU4 and T1 samples.

Table 26: Staco and Muid fake rates for SU1, SU3, SU4 and T1 samples.

	STACO	MUID
SU1, Def1 of truth μ	$4.5(2) \times 10^{-4}$	$4.2(2) \times 10^{-4}$
SU1, Def2 of truth μ	$1.4(4) \times 10^{-5}$	$0.9(3) \times 10^{-5}$
SU1, Def3 of truth μ	$1.4(4) \times 10^{-5}$	$0.9(3) \times 10^{-5}$
SU3, Def1 of truth μ	$4.1(3) \times 10^{-4}$	$3.6(2) \times 10^{-4}$
SU3, Def2 of truth μ	$1.4(5) \times 10^{-5}$	$1.0(3) \times 10^{-5}$
SU3, Def3 of truth μ	$1.3(5) \times 10^{-5}$	$1.0(3) \times 10^{-5}$
SU4, Def1 of truth μ	$12.4(4) \times 10^{-4}$	$11.1(3) \times 10^{-4}$
SU4, Def2 of truth μ	$1.5(4) \times 10^{-5}$	$0.6(2) \times 10^{-5}$
SU4, Def3 of truth μ	$1.5(4) \times 10^{-5}$	$0.6(2) \times 10^{-5}$
T1, Def1 of truth μ	$17.2(3) \times 10^{-4}$	$15.8(3) \times 10^{-4}$
T1, Def2 of truth μ	$1.9(3) \times 10^{-5}$	$1.4(3) \times 10^{-5}$
T1, Def3 of truth μ	$1.5(3) \times 10^{-5}$	$0.9(2) \times 10^{-5}$

10.4 $Z' \to \mu^+\mu^-$ and $W' \to \mu\nu$

Many extensions of the Standard Model predict the existence of heavy, neutral or charged, vector bosons generally called Z' and W'. Their leptonic decays to muons, ($Z' \to \mu^+\mu^-$ and $W' \to \mu\nu$), are very promising discovery channels, since their hadronic decays would be difficult to trigger and detect, given

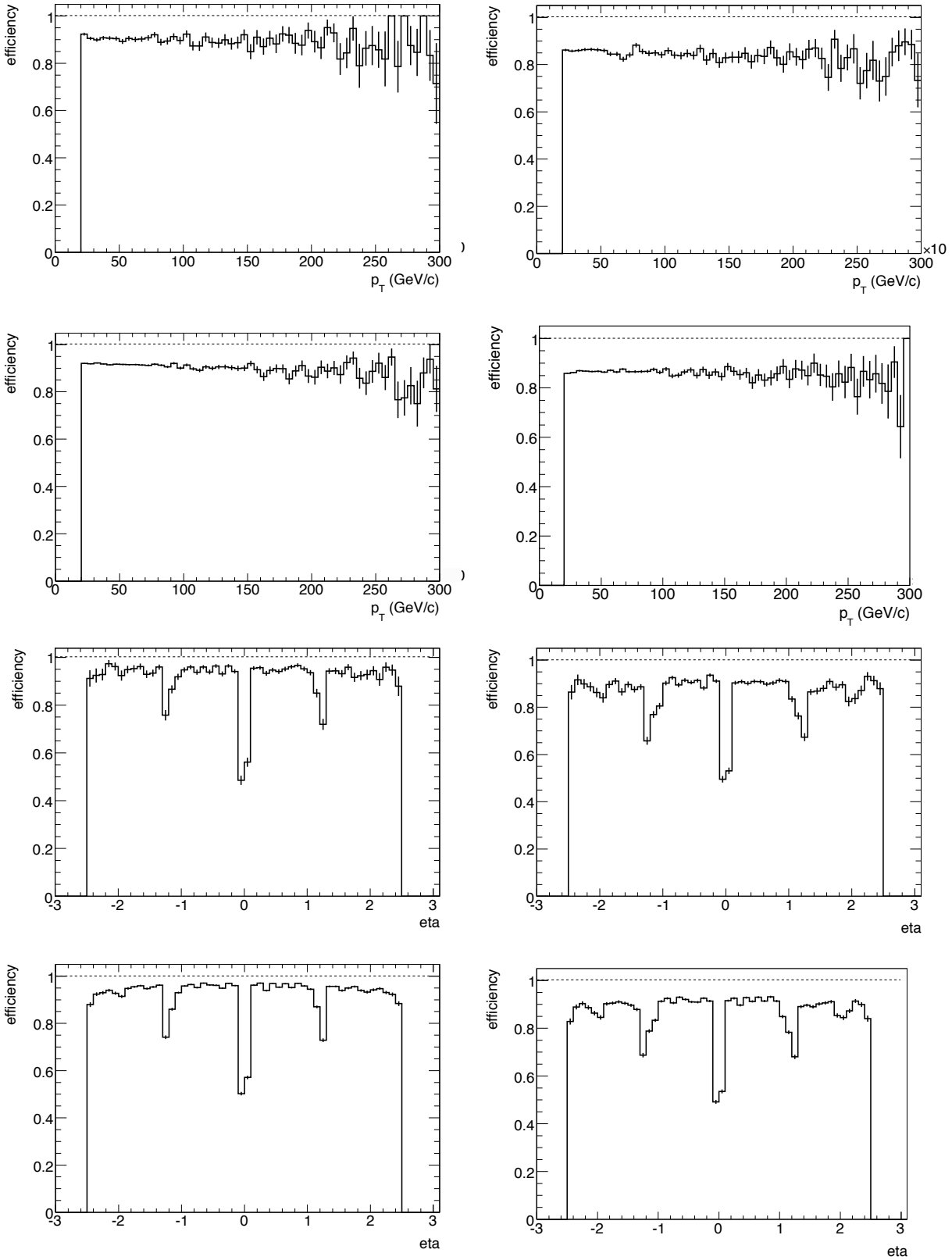

Figure 34: Muon efficiencies for Staco (left) and Muid (right) as a function of pT (top and first from the top) and eta (second from bottom, bottom) for the SU3 sample (top, second from bottom) and T1 sample (second from top, bottom).

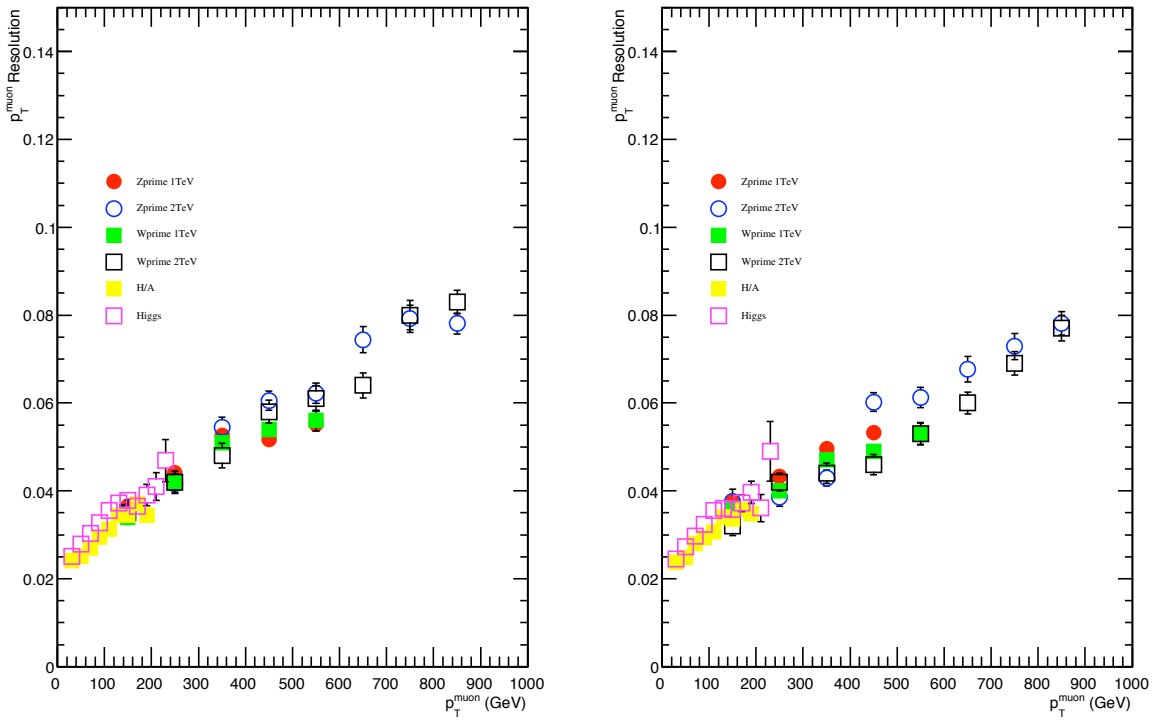

Figure 35: Muon p_T resolution for various samples: Zprime 1 TeV, Zprime 2 TeV, Wprime 1 TeV and Wprime 2 TeV, as well as for H/A and Higgs decays. Left for Staco+MuTag, right for Muid+MuGirl.

the enormous QCD background. In the following, the performance of the muon reconstruction algorithms is studied, for two gauge boson masses, 1 and 2 TeV. The datasets used are shown in table 27.

Table 27: Data samples used for Z' and W' study.

Sample	No. events
trig1_misal1_csc11.005601.Zprime_mumu_pythia_SSM1000.recon.AOD.v12000604	42750
trig1_misal1_csc11.005602.Zprime_mumu_pythia_SSM2000.merge.AOD.v12000604	10000
trig1_misal1_csc11.005610.Wprime1000emutau.merge.AOD.v12000604	28500
trig1_misal1_csc11.005611.Wprime2000emutau.merge.AOD.v12000604	28500

The muon p_T values vary from a few GeV up to almost 1 TeV (for a 2 TeV mass Z' or W'). The p_T resolution can be seen in figure 35. In this case, a 2 σ fit has been performed for each p_T residual distribution.

The mass residuals $m_{true} - m_{reconstructed}$ for the two different generated masses of Z' are shown in figure 36. The analysis is presented at preselection level, where at least two opposite charged muons with $p_T > 50$ GeV are required. In addition, the transverse energy deposited in the calorimeter within a cone, $\Delta R = 0.4$, around the muon, normalized to the muon p_T, is requested to be less than 0.2. If more than two muons fulfill the above criteria, the Z' candidate is formed by combining the two most energetic

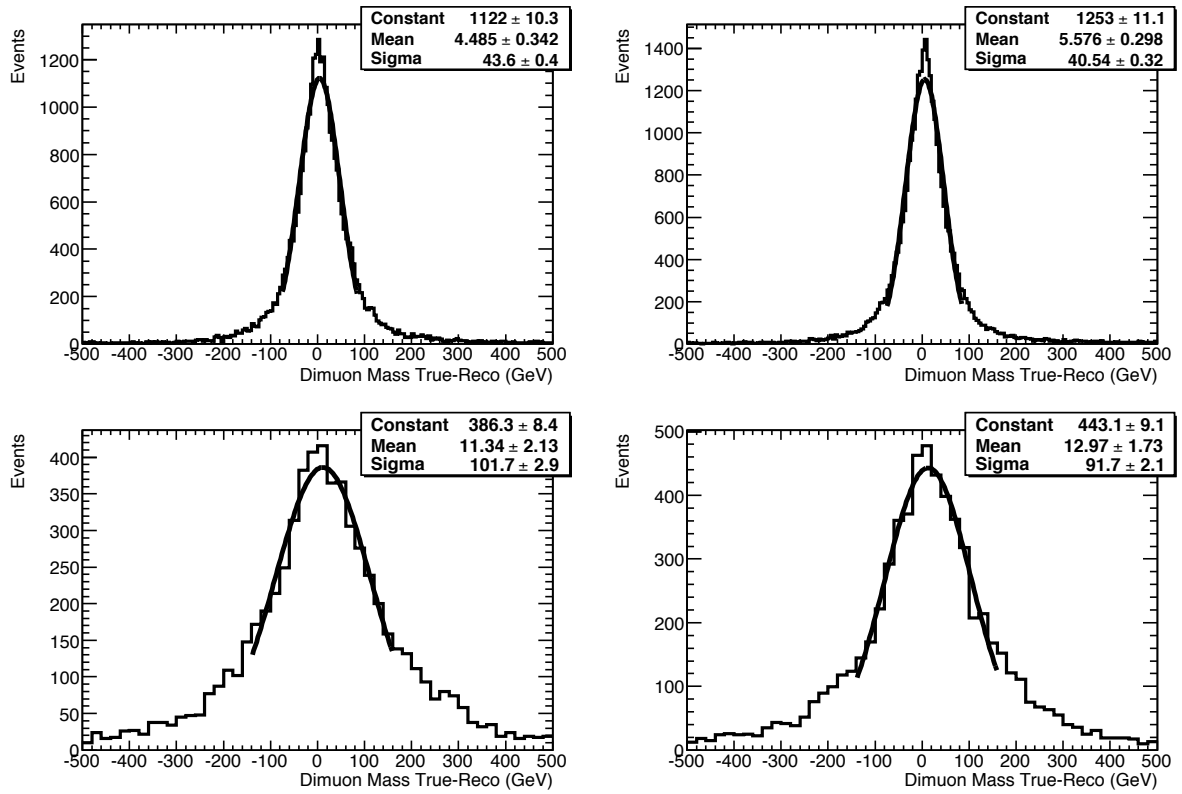

Figure 36: Mass residual distributions for 1 TeV Z' Staco+MuTag (upper left) and Muid+MuGirl (upper right) and 2 TeV Z' Staco+MuTag (bottom left) and Muid+MuGirl (bottom right).

muons.

A more detailed study of the behavior of the two algorithms is summarized in table 28. The corresponding mean values and standard deviations, the efficiency of obtaining a candidate with the above mentioned criteria and the fraction of the selected events in 2 σ and 5 σ windows are shown.

A test of the mass resolution linearity is obtained by studying the resolution for a variety of resonances from J/ψ to Z' decays. Fig. 37 shows that both algorithm chains have mass resolution growing linearly with mass in the range of resonance masses between 3 GeV and 2 TeV.

10.5 Left-Right Symmetric Model

The W_R decays into a lepton and a heavy neutrino, which in turn decays into another lepton and two partons. Hence the signature for this process is two high p_T leptons and two high p_T jets. We study the muon channel of this decay by requiring some selection criteria for both muons and jets. In the following study, we compare Staco and Muid muons by looking at the fake rate, efficiency and resolution. Each muon candidate has several variables which can be used to reduce the fake rate. These variables are the fit χ^2, match χ^2 and the relative isolation energy EtIsolation defined as (caloEnergy(0.2) − EnergyLoss) divided by E_t where caloEnergy(0.2) is the energy from calorimeter cells within a cone size of 0.2 centered around the muon track. EnergyLoss is the muon energy loss in the calorimeter (due to ionization, bremsstrahlung, δ-rays, pair production, etc.).

To study the effect of these different quantities we use samples of Z($\mu\mu$) and Z($\mu\mu$)+jets events, which are the datasets run numbers 5151 and 5186, respectively. The Z+jets sample is used to span

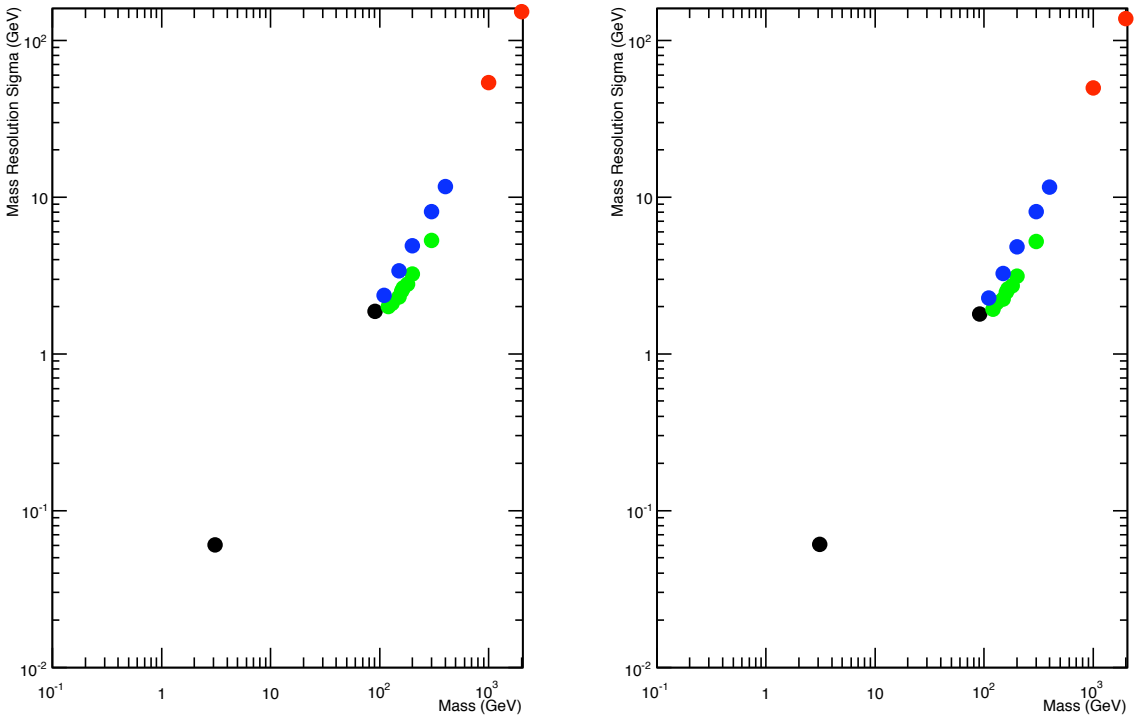

Figure 37: Mass resolution as a function of resonance mass for J/ψ and Z decays (black), Higgs decays to leptons (green), H/A decays (blue) and Z' decays (red). Results are shown for Staco+MuTag (left) and Muid+MuGirl (right).

Table 28: Properties of reconstructed dimuon masses from Z' decays. Gaussian mean μ and width σ, efficiency with preselection cuts (as described in the text) and fraction of events in a window of approximately 2 and 5 σ from the peak.

Zprime mass = 1TeV	Staco+MuTag	Muid+MuGirl
μ (MeV)	4380 ± 330	5420 ± 290
σ (GeV)	46.3 ± 0.3	43.6 ± 3.04
Efficiency %	71.2 ± 0.002	74.0 ± 0.002
Fraction in 5 σ (%)	91.9 ± 0.001	91.5 ± 0.001
Fraction in 2 σ (%)	79.9 ± 0.002	80.0 ± 0.002
Zprime mass = 2TeV	Staco+MuTag	Muid+MuGirl
μ (MeV)	1160 ± 190	1340 ± 170
σ (GeV)	122 ± 2.1	114 ± 1.9
Efficiency %	68.9 ± 0.005	71.8 ± 0.004
Fraction in 5 σ (%)	89.2 ± 0.003	88.5 ± 0.003
Fraction in 2 σ (%)	76.7 ± 0.003	76.4 ± 0.004

a high-p_T region up to 200 GeV/c. The analysis procedure consists of defining the muon fake to be a reconstructed muon which does not match any μ-truth within a cone of 0.1 making use of Monte Carlo generator information. Since reconstructed muons fall into three categories: combined, low-p_T or standalone muons, we choose to study two cases, the case where the muon track is a combined muon and the case where it is either combined, lowPt or standalone muon. In each case, we study the efficiency and fake rate varying the isolation cut "EtIsolation" following the prescription $\mid$ EtIsolation $\mid \leq (0.3 - j * 0.025)$, where j=[0,9] and the first point corresponds to $\mid$ EtIsolation $\mid \leq 1$, see Fig. 38 for the case of combined muons and Fig. 39 for the case of combined, lowPt or standalone muons.

We conclude from this study that combined muons provide already a lower fake rate with respect to the use of combined, lowPt or standalone muons. And for combined muons the fake rate goes down substantially after requiring the isolation cut of 0.3 while the efficiency drops by a couple of a percent. Also the fake rate for Staco muons is a bit higher than the fake rate for Muid muons.

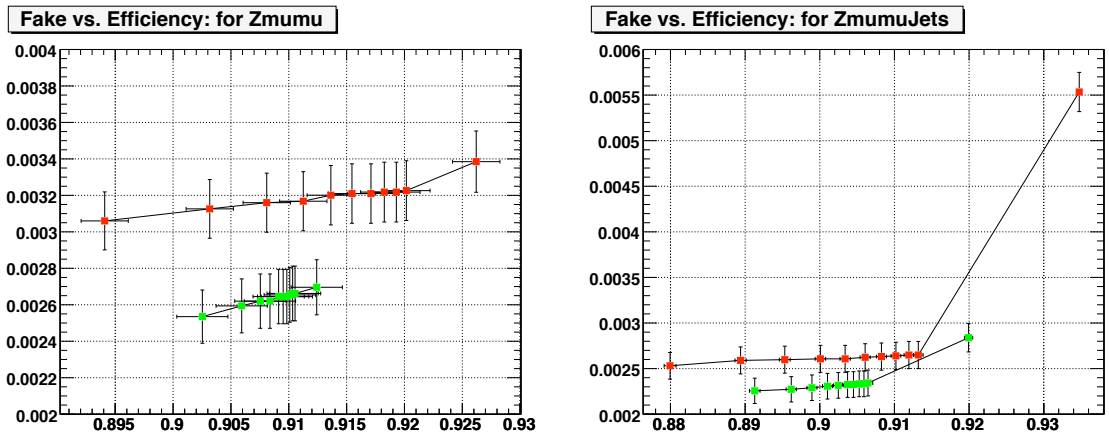

Figure 38: Fake rate vs. efficiency for combined muons using the Z($\mu\mu$) (left) and Z($\mu\mu$)+jets datasets (right): Staco (red) and Muid (green).

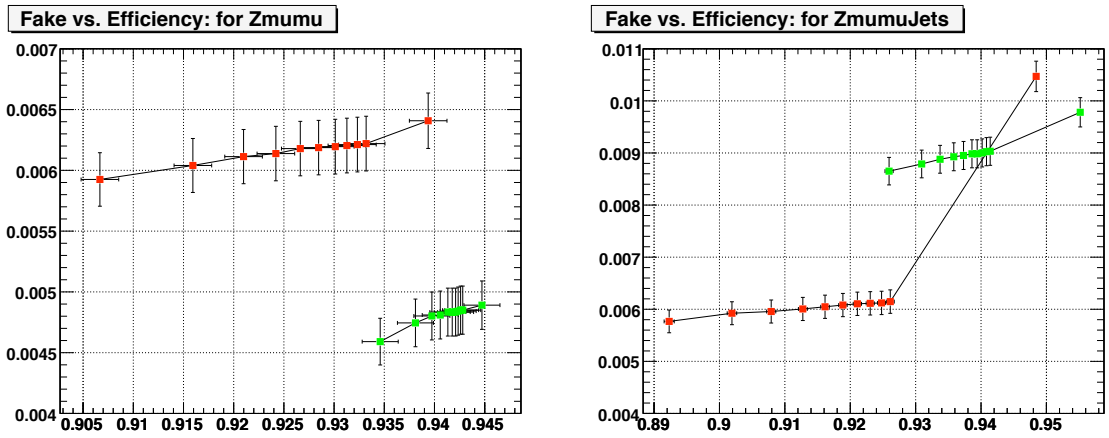

Figure 39: Fake rate vs. efficiency for combined, lowPt and standalone muons using the Z($\mu\mu$) (left) and Z($\mu\mu$)+jets datasets (right): Staco+MuTag (red) and Muid+MuGirl (green).

The transverse momentum, η and ϕ resolutions shown in Fig. 40 are obtained using the LRSM dataset 5650, where the leading high-p_T muon is matched to the leading high-p_T truth muon originating from the W_R decay. Table 29 summarizes the results of a Gaussian fit to the central part of the residual distributions. The Staco and Muid resolutions are the same within uncertainties.

Table 29: Mean and width values for p_T, η and ϕ residual distributions for the different muon algorithms.

	P_t resolution ($\times 10^{-3}$)		η resolution ($\times 10^{-5}$)		ϕ resolution ($\times 10^{-5}$)	
	Mean	σ	Mean	σ	Mean	σ
Staco	0.52 ± 0.17	6.90 ± 0.17	0.2 ± 0.4	17.5 ± 0.4	0.1 ± 0.1	2.6 ± 0.1
MuTag	3.10 ± 7.13	10.51 ± 8.31	-4.5 ± 6.2	24.4 ± 8.9	-0.4 ± 3.9	11.2 ± 5.7
Staco standalone	1.42 ± 1.52	9.09 ± 1.76	2.8 ± 2.1	17.3 ± 2.2	0.2 ± 0.4	2.8 ± 0.5
Muid	0.54 ± 0.16	6.61 ± 0.17	-0.4 ± 0.4	17.1 ± 0.4	0.1 ± 0.1	2.6 ± 0.1
MuGirl	0.72 ± 1.27	6.11 ± 1.04	N/A	N/A	N/A	N/A
Muid standalone	-2.08 ± 3.86	12.58 ± 5.39	5.1 ± 7.2	33.9 ± 10.5	-1.1 ± 0.5	4.2 ± 0.5

It is also worth to look at the dependence of the p_T resolution versus p_T, isolation variable, match χ^2/ndf and fit χ^2/ndf (fit-χ^2 from the muon spectrometer) for both Staco and Muid muons as shown in Fig. 41. Figure 40 compares the mass resolution of the W_R and the heavy neutrino N_μ for both Staco and Muid, where the selection criteria used for muons and jets are:

- Use either Staco or Muid.
- Select combined muons only.
- $P_t \geq 20$ GeV/c and $|\eta| \leq 2.5$.
- Loose cut on the relative isolation energy (EtIsolation ≤ 0.3).

While, the selection criteria for jets are:

- Use Cone4 jets.

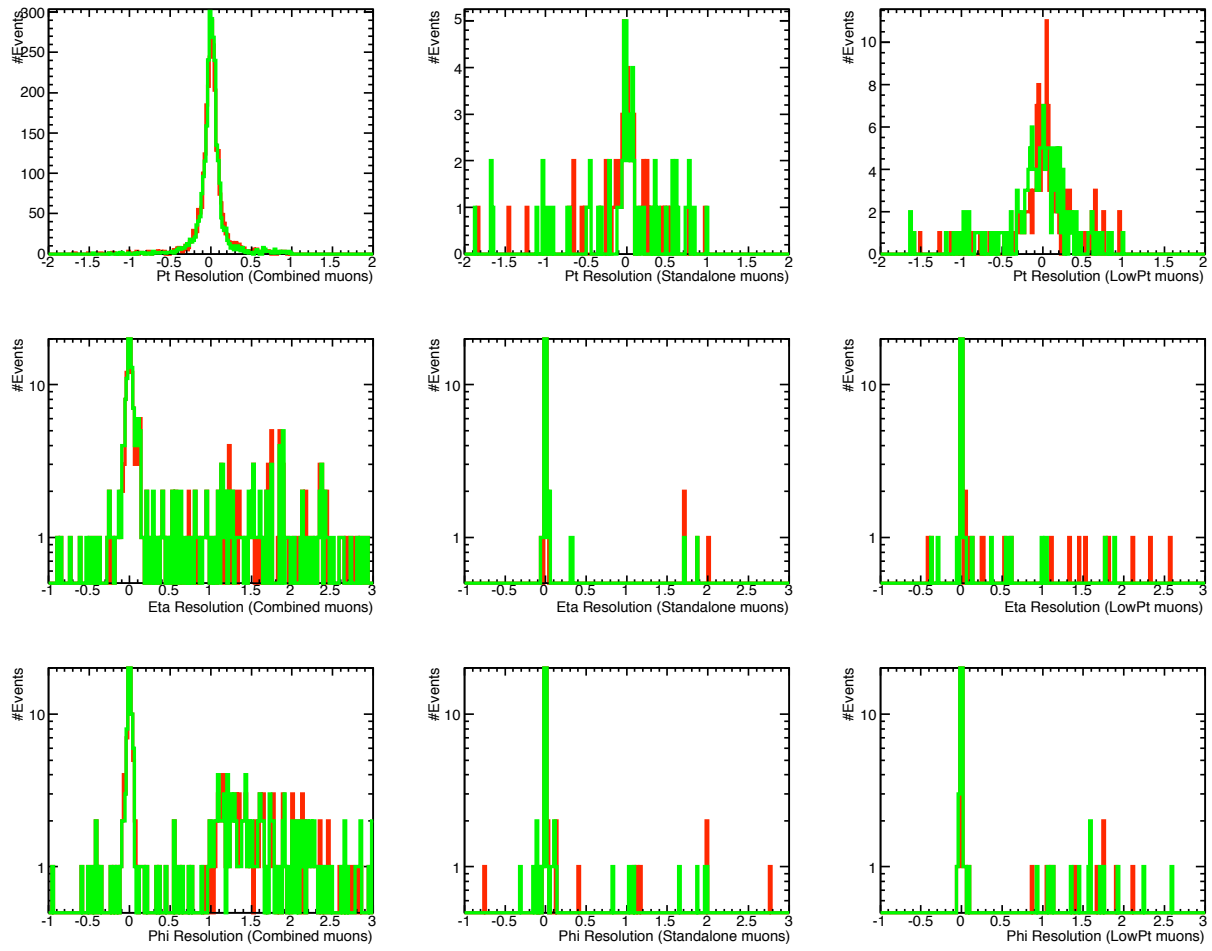

Figure 40: p_T resolution vs. p_T, η resolution vs. η and ϕ resolution vs. ϕ for combined (left), LowPt (middle) and standalone muons (right).

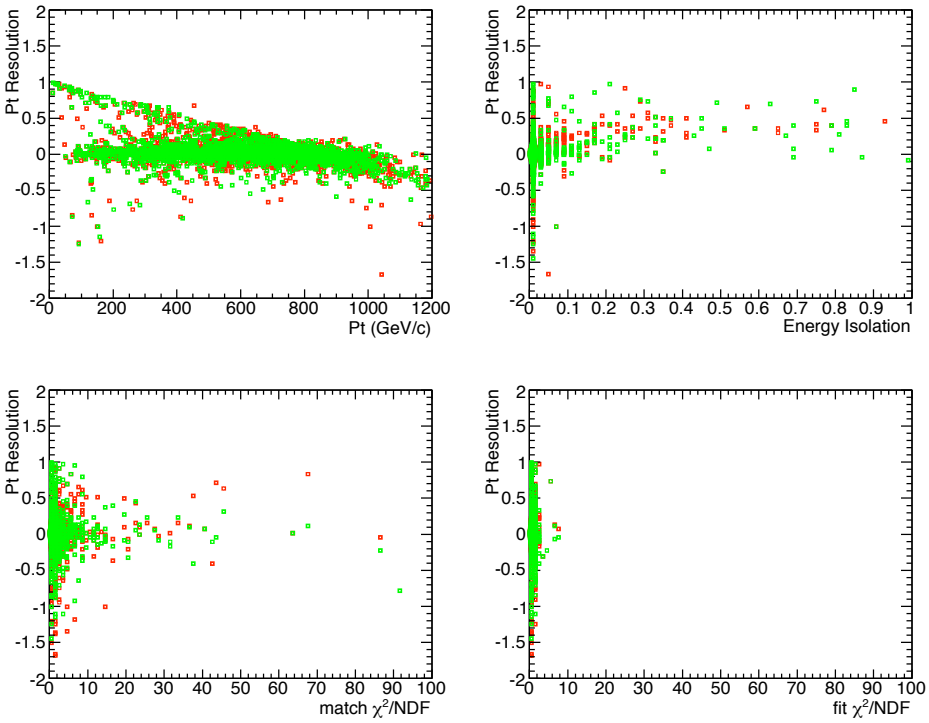

Figure 41: p_T resolution vs. p_T, Isolation variable, match χ^2/ndf and fit χ^2/ndf for Staco (red) and Muid (green).

- $P_t \geq 20$ GeV/c and $|\eta| \leq 2.5$.

We reconstruct the W_R invariant mass by combining the two highest-p_T muons and the two highest-p_T jets. For the heavy neutrino N_R invariant mass, we combine the two highest-p_T jets with the second highest p_T muon. The two highest p_T jets are combined with the second highest P_t jet to form the heavy neutrino.

Table 30: Mean and sigma values of the single Gaussian fit for resolution variables.

	Staco ($\times 10^{-2}$)		Muid ($\times 10^{-2}$)	
	Mean	σ	Mean	σ
W_R	0.77 ± 0.21	7.06 ± 0.21	1.03 ± 0.21	7.09 ± 0.20
N_μ	-1.78 ± 0.25	6.45 ± 0.24	-1.70 ± 0.27	6.68 ± 0.26

The efficiency to find a combination of two high-p_T muon tracks and two high p_T jets ($\mu\mu$jj), so that the invariant mass resolution function is within a fixed resolution window of ± 0.2, is $49.0 \pm 1.5\%$ for Staco muons and $48.1 \pm 1.5\%$ for Muid muons. In conclusion, Staco and Muid algorithms have similar performance within the quoted uncertainties.

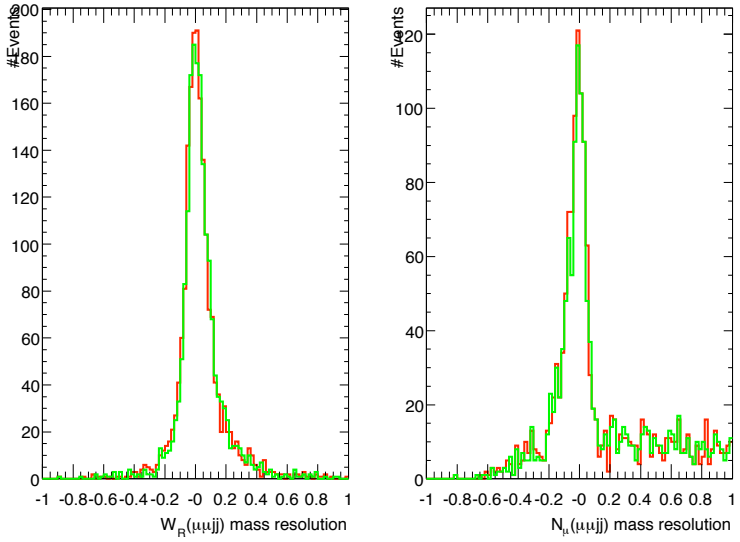

Figure 42: Mass resolution functions for the W_R (right) and N_μ (left) for Staco (red) and Muid (green).

11 Summary

11.1 Present status

The starting point for most ATLAS analyses are the combined muons, i.e. those muons constructed by combining tracks found independently in the inner detector and muon spectrometer. Their momentum resolution and fake rate (with appropriate quality cuts) are both significantly better than muons reconstructed from either the spectrometer alone or muons identified by tagging inner detector tracks. In $t\bar{t}$ events, for muons from $W \to \mu\nu$ with $|\eta| < 2.5$, the Staco combined muon efficiency is 94% with most of the loss coming from regions of the spectrometer where the detector coverage is thin. The efficiency falls by a few percent when the muon transverse momentum reaches the TeV scale where it is much more likely that a muon will radiate a substantial fraction of its energy. The $t\bar{t}$ rate for fakes is a few per thousand events for $p_T > 20$ GeV/c and this can be reduced by an order a of magnitude (with a 2% loss in efficiency) by cutting on the muon quality (χ^2_{match}). The performance of the Muid algorithm is only slightly worse for $t\bar{t}$ but it is significantly less robust, losing additional efficiency at low-p_T and high-p_T and when luminosity background is added.

The combined muons can be supplemented with the standalone muons to extend the η coverage to 2.7 and to recover the percent or so efficiency loss in combination. We do not report on this merge but it is clear from the standalone results that the fake rates will increase significantly especially when luminosity background is present. In the case of Moore, the fake rate is likely intolerable.

We find that merging with MuTag provides only slight improvement to the Staco efficiency with a significant increase in fakes. This may reflect the success of Staco more than deficiencies in MuTag. MuGirl is able to improve the Muid efficiency, so that the merge Muid+MuGirl has performance similar to Staco or Staco+MuTag. By itself, the MuGirl efficiency is somewhat less than that of Staco especially for high-p_T muons, and the fake rates are substantially higher.

11.2 Future

The results presented here reflect the status of the ATLAS software used to reconstruct (Monte Carlo) production data in 2007. Work continues both to improve the algorithms described here and to add new ones. The high-luminosity fake rate for Moore is being addressed by introducing timing cuts and investigating alternative approaches to the pattern recognition. The latter also has the goal of reducing the number of false hit assignments. Combined muons with large χ^2_{match} are being studied to see if a second stage of pattern recognition can reduce the efficiency loss or resolution tails. Efforts are underway to improve or replace the existing spectrometer-tagging algorithms; in particular, code is already in place to extrapolate to additional stations enabling recovery of much of the standalone/combined efficiency loss near $|\eta| = 1.2$. Two calorimeter-tagging algorithms have been developed and offer the possibility of recovering much of the efficiency loss near $\eta = 0$. Improvements in modularity will make it possible to mix components from the different algorithms, (e.g. to use Muid to combine Muonboy muons) and enable algorithms to share common tools such as those being developed to calculate energy loss, refit muon tracks, and repair muons with poor fit quality.

Appendices

A Known issues with simulation and reconstruction in release 12.0.6

A series of problems affect the performance extracted from the MC samples in release 12.0.6. All are fixed in release 14.

A.1 Simulation

- Magnetic field propagation: the parameters used for the tracking of particles through the magnetic field of the spectrometer inside Geant 4 was too big in regions where the field varies rapidly. When comparing the trajectory of muons with $p_T = 100$ GeV/c computed by Geant 4 to the one for precise propagators starting from the same point at the entrance of the spectrometer, differences of up to 400 μm are seen at the level of the outer stations in some specific η regions.
- Resolution in CSC: the gain of the cathode strip chambers was too big (by a factor 2) in simulations before release 13. This resulted in a mean cluster resolution of about 40 μm instead of the expected 60 μm.
- Cavern background suffered from a series of problems, see next Appendix.

A.2 Reconstruction

- Handling of out-of-time hits inside Moore: particle crossing a tube before the trigger time, inside a window corresponding to the full drift time of the tube (about 700 ns) can mask a genuine muon hit. In the simulations with pileup and cavern background, these hits were present but were not properly taken into account inside Moore.

B Pileup and cavern background

The pile-up is simulated as a number of minimum bias collisions properly distributed in time and overlayed onto the physics collision. Every collision is normally simulated only for a few 100 ns of the propagation time. But there is one component missing in this approach: neutrons may fly in the ATLAS cavern for a few seconds until they are thermalised, thus producing some kind of permanent neutron-photon gas which creates a constant rate of Compton electrons and spallation protons. This component, i.e. additional hits created by long-lived particles, is referred to as *cavern background*.

The cavern background consists mainly of thermalised slow neutrons, long-lived neutral kaons and low-energy photons escaping the calorimeter and the forward beam and shielding elements. High cavern-background rates would degrade the performance of the muon spectrometer. The radiation levels to be expected in the ATLAS cavern have been simulated as a function of R and Z [27] for the design luminosity of $10^{34}\,cm^{-2}s^{-1}$. Depending on the type of radiation effect and exact composition of the equipment, these values have to be multiplied by safety factors (SF) for specific purposes. The cavern background is simulated as a separate component (that is added on top of every single minimum bias event) as follows:

- A standalone dedicated Geant3/GCALOR based detector simulation program with improved neutron propagation and a simplified ATLAS geometry is run on pp collisions. The output of this program provides particle fluxes in the envelopes (scoring volumes) surrounding muon spectrometer chambers. The fluxes are provided as a list of particles with all related parameters per pp interaction at the entrance of each chamber envelope.

- The kinematic truth information of the list of particles generated by Geant3/GCALOR are converted to HepMC/POOL format, and the spectrum is modified to be uniform in the time interval of $[0,25]$ ns.

- The cavern events are mixed, at different safety factor varying between 1 and 10, at the generator level with the minimum bias and signal events.

- The simulation of the detector response is then carried out in Geant4.

There are however a number of issues with the simulation of the cavern bacground:

1. The statistics in the available cavern events is limited: 40K events for a safety factor of 1; 10K events for safety factor of 2 and 5; and 5K events for safety factor of 10. Because of the limited statistics, a number of MDT tubes fire more often than expected (resulting in spikes in the hit response of the spectrometer).

2. The absence of scoring volumes in the version of Geant4 used for the simulation leads to the tracking of the neutrals through the entire detector, thus producting additional interactions that should have been terminated at the scoring volume boundaries (resulting in multiple counting).

3. The original primary cavern events were generated in an older version of Pythia where the generated particle density is reported to be a factor of 2 lower than in the newer versions of Phythia.

The scoring volumes are being implemented in the current ATLAS detector simulation, with the longer term objective to regenerate in the primary cavern background events in the new versions of Pythia and the simulation done in Geant4. In the short term, the limited statistics of the cavern events can be fixed by taking advantage of the phi-symmetry of the muon spectrometer - rotating the cavern event kinematics eight times. Further improvement in the available cavern statistics can be achieved by throwing the

neutrals many times since the probability of neutral interaction is very low, of the order 1%: these efforts have taken place since release 12. A way of removing the duplicates (absence of scoring volumes) from the available cavern files is also being considered as a part of the short term plan.

References

[1] G. Aad, et al., JINST **3** (2008) S08003.

[2] ATLAS collaboration, "Muons in the ATLAS Calorimeters: Energy Loss Corrections and Muon Tagging", ATL-COM-PHYS-2009-153, 2009.

[3] S. Hassani, et al., NIM **A572** (2007) 77–79.

[4] Th. Lagouri, et al., IEEE Trans. Nucl. Sci. **51** (2004) 3030–3033.

[5] D. Adams, et al., ATL-SOFT-2003-007 (2003).

[6] K. Nikolopoulos, D. Fassouliotis, C. Kourkoumelis, and A. Poppleton, IEEE Trans. Nucl. Sci. **54** (2007) 1792–1796.

[7] T. Cornelissen, et al., ATL-SOFT-PUB-2007-007 (2007).

[8] S. Tarem, Z. Tarem, N. Panikashvili, O. Belkind, Nuclear Science Symposium Conference Record, 2007 IEEE **1** (2007) 617–621.

[9] T. Sjostrand, S. Mrenna, and P. Skands, JHEP **05** (2006) 26.

[10] S. Frixione and B.R. Webber, JHEP **0206** (2002) 029.

[11] S. Frixione, P. Nason and B.R. Webber, JHEP **0308** (2003) 007.

[12] J. Allison et al., IEEE Transactions on Nuclear Science **53** (2006) 270–278.

[13] ATLAS collaboration, "Beauty Production Cross Section Measurements at LHC: B-physics Reference channel $B^+ \to J/\psi K^+$ and Inclusive Methods", this volume.

[14] G. Corcella et al., hep-ph/0210213.

[15] R. Clifft, A. Poppleton, "IPATREC: inner detector pattern-recognition and track-fitting", ATL-SOFT-94-009, 1994; https://twiki.cern.ch/twiki/bin/view/Atlas/IPatRec.

[16] I. Gavrilenko, "Description of Global Pattern Recognition Program: XKalman", ATLAS note, ATL-INDET-97-165, 1997; https://twiki.cern.ch/twiki/bin/view/Atlas/InDetXKalman.

[17] T. Cornelissen, et al., "Design and Implementation of the ATLAS New Tracking", ATL-COM-SOFT-2007-002, 2007.

[18] L. Kashif, D. Levin, "Muon track reconstruction performance of ATLAS inner detector tracking algorithms", ATL-COM-MUON-2007-010, 2007.

[19] T. Lagouri, J. del Peso, "EventView Analysis Package Hto4lEV for Higgs to Four Leptons Searches", ATL-PHYS-INT-2008-028, 2008.

[20] T. Lagouri, J. DelPeso, "Hto4lEV EventView Analysis for Higgs to Four Leptons Searches", ATL-COM-PHYS-2008-031, 2008.

[21] G. Aad, et al., CERN-OPEN-2008-020 (2008).

[22] G. Corcella et al., JHEP **0101** (2001) 010.

[23] S. Moretti et al., JHEP **0204** (2002) 028.

[24] J.M. Butterworth and J.R. Forshaw, J. Phys. G **19** (1993) 1657.

[25] J.M. Butterworth, J.R. Forshaw and M.H. Seymour, Z. Phys. C **72** (1996) 637.

[26] H. Baer et al., hep-ph/0001086.

[27] M. Shupe, et al., "Radiation Task Force", ATL-GEN-2005-001, 2005.